



**POLITECNICO
DI TORINO**

Corso di Laurea Magistrale in Ingegneria Aerospaziale

Tesi di Laurea

**Modelling, Performance Assessment and Aerodynamic
Optimisation of a Supersonic Through-Flow Rotor**

Relatore:

Prof. Dario Giuseppe PASTRONE

Candidato:

Jordy GRASSO

Ottobre 2018

Abstract

Civil supersonic transport represents the new aviation frontier. Noise regulations constitute the main obstacle to the born of such transport system. Many new engine concepts capable of overcoming such a constrain have been studied. Some preliminary studies suggested that an engine equipped with a fan capable of accepting supersonic inflow could be a suitable and competitive configuration for this market. A supersonic through-flow rotor has been tested by NASA in order to understand the main characteristics and limits of this peculiar concept. Aim of the thesis is to model and optimise the supersonic through-flow rotor focussing on the effects of geometry variations on performance.

By using the experimental data released by NASA, a model of such rotor has been designed. The blade is modelled by setting both the blade angle and thickness distributions at three layers: 0%, 50% and 100% of the blade span. The full model is obtained by the interpolation of such distributions on the whole blade span. The model is validated by comparing computational fluid dynamics results with experimental data. Both the design and off-design flow characteristics are appropriately replicated, justifying when possible the rotor performance. At design point conditions, the rotor shows a total pressure ratio of 2.48 and an isentropic efficiency of 77.3%.

Once validated, the rotor total pressure ratio and isentropic efficiency are enhanced by modifying both the original blade angle and thickness distributions. The optimisation method is carried out at design point conditions and uses a combination of response surface evaluations and genetic algorithms. The optimised blade shows a broader blade passage, a higher blade loading and a lower blade solidity. As a consequence, the work done on the flow is higher and the skin friction losses are lower. The optimised blade shows a total pressure ratio of 3.03 and an isentropic efficiency of 78.8% at design point conditions.

Keywords: Computational Fluid Dynamics, Genetic Algorithm, Response Surface, Supersonic Civil Transport, Supersonic Compressor, Supersonic Fan, Transonic Compressor.

Acknowledgements

To begin with, I want to thank my parents, Giacomo and Marie, without whom I would never have reached such level in my studies. Thanks go to the people who made the writing of this thesis possible, such as Prof Vassilios Pachidis, Mr Salvatore Ippedico and all the UTC staff. Then, I want to thank my colleague Bhargav, who introduced me to the world of CFD for the first time. A thank you goes also to the central perk people, Florian, Davide, Francisco and Pierre, who have supported me morally during this year. Last but not least, I thank the Spaniards group who made this year less difficult to live. I will never forget the failed BBQs and all the travels made together.

Contents

Acknowledgements	v
Contents	vi
List of Figures	viii
List of Tables	xi
Nomenclature	xiii
1 Introduction	1
1.1 Background	1
1.2 Thesis Aim and Objectives	3
1.3 Document Structure	4
2 Literature Review	5
2.1 SSTF Engine Performance Comparisons	6
2.1.1 SSTF Engine - TBE	6
2.1.2 SSTF Engine - VSCE	9
2.1.3 SSTF Engine - MFTF Engine	9
2.1.4 SSTF Engine Overall Advantages	10
2.2 Historical SSTF Development	11
2.3 Test Facility	13
2.3.1 Facility Scheme and Instrumentation Location	14
2.3.2 Supersonic Starting Process	17
2.4 Rotor Operating Modes	23
2.4.1 Subsonic Through-Flow Mode	23
2.4.2 Impulse-Type Mode	28
2.4.3 Supersonic Inflow Starting	31
2.4.4 Supersonic Through-Flow Mode	33
3 Methodology	35
3.1 Methodology Scheme	35
3.2 Domain Definition	36
3.3 Original Blade Modelling	37
3.4 Mesh Design	41
3.4.1 Mesh Dependency Study	43

3.4.2	Grid Quality Assessment	44
3.5	Computational Fluid Dynamics	46
3.5.1	Boundary Conditions	48
3.5.2	Solver Settings	49
3.6	Optimisation Process	51
3.6.1	Response Surface Methodology	53
3.6.2	Design of Experiments	54
3.6.3	Response Surface Quality Assessment	56
3.6.4	Genetic Algorithms	58
3.7	Summary	61
4	Results and Discussions	62
4.1	Validation Process	62
4.1.1	Subsonic Through-Flow Operating Mode	63
4.1.2	Impulse-Type and Supersonic Through-Flow Operating Modes	70
4.2	Optimisation Process	79
4.2.1	Response Surface Generation	79
4.2.2	Pareto Front Generation	84
4.3	Optimised Blade Model	85
4.3.1	Subsonic Through-Flow Operating Mode	88
4.3.2	Impulse-Type and Supersonic Through-Flow Operating Modes	90
4.4	Summary	96
5	Conclusions	99
5.1	Future Work	101
	References	103
A	Gas Turbine Performance Aspects	108
A.1	Specific Thrust Considerations for Supersonic Flight	108
A.2	Spillage Drag for External-Compression Supersonic Intakes	110
B	Settings Tables and Charts	113
B.1	Domain Definition	113
B.2	Original Blade Model	114
B.3	Mesh Settings	121
B.4	Boundary Conditions and Solver Settings	121
B.5	Optimised Blade Model	123

List of Figures

2.1	Supersonic Through-Flow Fan Engine [4, pp.2]	7
2.2	Turbine Bypass Engine [5, pp.5]	7
2.3	Variable Stream Control Engine [6, pp.350]	7
2.4	Conventional Mixed-Flow Turbofan Engine [4, pp.2]	7
2.5	Flight mission benefit of the SSTF engine over the TBE [7, pp.4]	8
2.6	Test Facility Scheme [7, pp.25]	15
2.7	Test Package Scheme [18, pp.12]	15
2.8	Pressure Rake Element Location [7, pp.28]	15
2.9	Stations Location	16
2.10	Rotor Zero-Reference Location [7, pp.27]	17
2.11	Test Package with Possible Area Reduction Sections [7, pp.59]	18
2.12	Stable Condition in a Duct with Two Choked Throats [7, pp.64]	19
2.13	New Stable Shock Condition [7, pp.66]	20
2.14	Rotor and Diffuser Choked Condition [7, pp.61]	22
2.15	Unique-Incidence Condition for a Flat Plate Cascade [20, pp.103]	24
2.16	Flow Field Model for Unique-Incidence Condition [7, pp.276]	25
2.17	Influence of Suction Surface Angle on Inlet Mass Flow [7, pp.282]	26
2.18	Subsonic Rotor Performance Map [7, pp.81]	28
2.19	Rotor Outflow Velocity Triangle [7, pp.152]	29
2.20	Conditions Necessary for Impulse-Type Operating Mode [7, pp.153]	30
2.21	Rotor Total Temperature Ratio During Impulse-Type Mode as a Function of Axial Outflow Mach Number and Relative Outflow Angle [7, pp.155]	30
2.22	Supersonic Inflow Starting Condition [20, pp.104]	32
2.23	Supersonic Rotor Performance Map [7, pp.180]	34
3.1	Methodology Scheme	36
3.2	BladeGen Working Scheme [25, pp.64]	38
3.3	Meridional Profile	38
3.4	Original Blade Model and Domain Representation	39
3.5	Original Blade Hub Section	40
3.6	Original Blade Mid Section	40
3.7	Original Blade Tip Section	40
3.8	Structured and Unstructured Mesh [24, pp.26]	41
3.9	Mid-Span Y^+ at Design Point Conditions	42
3.10	Isentropic Efficiency Grid Dependency	43
3.11	Final Mesh - Lateral View	46
3.12	Domain Suddivision	49

3.13 Residuals for choking conditions at 50% rotational speed	50
3.14 Efficiency Stability for choking conditions at 50% rotational speed	50
3.15 Full Factorial Design for Three Design Variables on Three Levels [35, pp.21]	54
3.16 Central Composite Design (CCD) for Three Design Variables [35, pp.23]	55
3.17 Comparison between LHS and CCD for Two Design Variables [35, pp.27]	56
3.18 Genetic Algorithm Process [37, pp.110]	59
4.1 Subsonic Performance Map	64
4.2 Subsonic Isentropic Efficiency Map	64
4.3 Mid-Span Absolute Mach Number Contours at Choking Conditions and 50% of Rotational Speed	66
4.4 Mid-Span Relative Mach Number Contours at Choking Conditions and 50% of Rotational Speed	66
4.5 Mid-span Relative Mach Number Contours at Choking Conditions and 60% of Rotational Speed	68
4.6 Meridional Absolute Mach Number Contours at Choking Conditions and 65% of Rotational Speed	68
4.7 Mid-span Absolute Mach Number Contours at Choking Conditions and 75% of Rotational Speed	69
4.8 Mid-span Relative Velocity Vectors at Choking Conditions and 75% of Rotational Speed	69
4.9 Mid-Span Absolute Mach Number Contours at Choking Conditions and 100% of Rotational Speed	71
4.10 Mid-Span Relative Mach Number Contours at Choking Conditions and 100% of Rotational Speed	71
4.11 Supersonic Total Pressure Map	72
4.12 Supersonic Efficiency Map	72
4.13 Mid-Span Absolute Mach Number Contours at Unstarted conditions and 60% of Rotational Speed	74
4.14 Mid-Span Absolute Mach Number Contours at Started conditions and 60% of Rotational Speed	74
4.15 Mid-Span Relative Mach Number Contours at Unstarted conditions and 75% of Rotational Speed	76
4.16 Mid-Span Absolute Mach Number Contours at Unstarted conditions and 75% of Rotational Speed	76
4.17 Mid-Span Absolute Mach Number Contours at Design Point	77
4.18 Mid-Span Relative Mach Number Contours at Design Point	77
4.19 Hub Blade Loading at Design Point	78
4.20 Tip Blade Loading at Design Point	78
4.21 Predicted and Observed Outputs	80
4.22 Total Pressure Ratio Local Sensitivity	82
4.23 Isentropic Efficiency Local Sensitivity	82
4.24 Total Pressure Ratio Response Surface	83
4.25 Isentropic Efficiency Response Surface	83
4.26 First Pareto Front	85

4.27 Optimised (Red) and Original (Black) Blade Hub Sections	86
4.28 Optimised (Red) and Original (Black) Blade Mid Sections	86
4.29 Optimised (Red) and Original (Black) Blade Tip Sections	86
4.30 Blade Passage Area Distributions for the Original and Optimised Blades	87
4.31 Subsonic Total Pressure Map	89
4.32 Subsonic Efficiency Map	89
4.33 Optimised Blade Mid-Span Absolute Mach Number Contours at Choking Conditions and 50% of Rotational Speed	91
4.34 Optimised Blade Mid-Span Relative Mach Number Contours at Choking Conditions and 50% of Rotational Speed	91
4.35 Supersonic Total Pressure Map	92
4.36 Supersonic Efficiency Map	92
4.37 Optimised Blade Mid-Span Absolute Mach Number Contours at Design Point	94
4.38 Optimised Blade Mid-Span Relative Mach Number Contours at Design Point	94
4.39 Original Blade Trailing Edge Streamlines	95
4.40 Optimised Blade Trailing Edge Streamlines	95
4.41 Optimised Blade Loading at Design Point (Hub)	97
4.42 Optimised Blade Loading at Design Point (Mid)	97
4.43 Optimised Blade Loading at Design Point (Tip)	97
A.1 Free stream, inlet and exhaust engine section locations [39, pp.26].	109
A.2 Pressure distribution around an air intake edge [39, pp.3].	111
A.3 Subcritical, critical and supercritical conditions [40, pp.15].	111
B.1 Original Blade Angle Distribution (Hub)	115
B.2 Original Blade Angle Distribution (Mean)	116
B.3 Original Blade Angle Distribution (Tip)	117
B.4 Original Thickness Distribution (Hub)	118
B.5 Original Thickness Distribution (Mean)	119
B.6 Original Thickness Distribution (Tip)	120
B.7 Optimised Blade Angle Distribution (Hub)	124
B.8 Optimised Blade Angle Distribution (Mean)	125
B.9 Optimised Blade Angle Distribution (Tip)	126
B.10 Optimised Blade Thickness Distribution (Hub)	127
B.11 Optimised Blade Thickness Distribution (Mean)	128
B.12 Optimised Blade Thickness Distribution (Tip)	129

List of Tables

2.1	Final SSTF stage characteristics [7, pp.17]	13
2.2	Test Package Geometry and Measurement Locations	17
2.3	Rotor Operating Modes [7, pp.56]	23
3.1	Isentropic Efficiency Grid Dependency	44
3.2	Mesh Quality Parameters	45
3.3	Adapted Blade Model Discretisation Points Location	52
4.1	Goodness of Fit Criteria	80
4.2	Blade Solidities	85
4.3	Response Surface Prediction and CFD Results Comparison at Design Point	87
B.1	Domain Points Locations	113
B.2	General Blade Model Settings	114
B.3	Angle Distribution Discretisation Points Locations (Hub)	115
B.4	Angle Distribution Properties (Hub)	115
B.5	Original Angle Distribution Discretisation Points Locations (Mean)	116
B.6	Original Angle Distribution Properties (Mean)	116
B.7	Original Angle Distribution Discretisation Points Locations (Tip)	116
B.8	Original Angle Distribution Properties (Tip)	117
B.9	Original Thickness Distribution Discretisation Points Locations (Hub)	118
B.10	Original Thickness Distribution Properties (Hub)	118
B.11	Original Thickness Distribution Discretisation Points Locations (Mean)	119
B.12	Original Thickness Distribution Properties (Mean)	119
B.13	Original Thickness Distribution Discretisation Points Locations (Tip)	120
B.14	Original Thickness Distribution Properties (Tip)	120
B.15	Turbogrid Settings	121
B.16	Domain Parts Boundary Settings	122
B.17	General Domain Settings	122
B.18	Subsonic Outlet Boundary Settings	123
B.19	Solver Settings	123
B.20	Optimised Angle Distribution Discretisation Points Locations (Hub)	124
B.21	Optimised Angle Distribution Properties (Hub)	124
B.22	Optimised Angle Distribution Discretisation Points Locations (Mean)	125
B.23	Optimised Angle Distribution Properties (Mean)	125
B.24	Optimised Angle Distribution Discretisation Points Locations (Tip)	126
B.25	Optimised Angle Distribution Properties (Tip)	126

B.26 Optimised Thickness Distribution Discretisation Points Locations (Hub)	. 126
B.27 Optimised Angle Distribution Properties (Hub) 127
B.28 Optimised Thickness Distribution Discretisation Points Locations (Mean)	128
B.29 Optimised Angle Distribution Properties (Mean) 128
B.30 Optimised Thickness Distribution Discretisation Points Locations (Tip)	. 129
B.31 Optimised Angle Distribution Properties (Tip) 129

Nomenclature

List of	Abbreviations
ASME	American Society of Mechanical Engineers
BSL	Baseline
CFD	Computational Fluid Dynamics
DoE	Design of Experiments
EA	Evolutionary Algorithm
EARSM	Explicit Algebraic Reynolds Stress Model
FAR	Federal Aviation Regulation / Fuel to Air Ratio
FCE	Fixed Cycle Engine
FLADE	Fan on Blade
GA	Genetic Algorithm
IFV	Inlet Flow Valve
LE	Leading Edge
MFTF	Mixed-Flow Turbofan
MOGA	Multi-Objective Genetic Algorithm
PR	Total Pressure Ratio
RAAE	Relative Average Absolute Error
RANS	Reynolds Averaged Navier-Stokes
RSM	Response Surface Methodology / Reynolds Stress Model
RSME	Root Mean Square Error
SF	Stream Force

SFC	Specific Fuel Consumption
SSCRD	Supersonic Counter-Rotating Diffuser
SST	Supersonic Transport / Shear-Stress-Transport
SSTF	Supersonic Through-Flow Fan
SSTR	Supersonic Through-Flow Rotor
TBE	Turbine Bypass Engine
TE	Trailing Edge
VCE	Variable Cycle Engine
VSCE	Variable Stream Control Engine

Roman Symbols

A	Cross Sectional Area
a	Speed of Sound
D	Spillage Drag
F	Thrust
L	Length
M	Mach Number
N	Rotational Speed / Number of Sampling Points
P	Pressure
R	Universal Gas Constant / Coefficient of Determination
Re	Reynolds Number
s	Blade Spacing
T	Temperature
u	Horizontal Velocity Component
V	Velocity
W	Mass Flow
y	Normal Wall Distance
y^+	Adimensional Wall Distance

y_i	Output Parameter Value at the i -th Sampling Point
y^*	Regression Model Value at the i -th Sampling Point
y'	Arithmetic Mean of the Values y_i

Greek Symbols

α	Absolute Flow Angle
β	Relative Flow Angle
γ	Ratio of Specific Heats
ε	Noise Error
η_R	Rotor Isentropic Efficiency
μ	Mach Angle/ Dynamic Viscosity
ν	Cinematic Viscosity
ρ	Density
σ_y	Standard Deviation of the Values y_i
τ_w	Shear Force at Wall

Subscripts

∞	Undisturbed Upstream Condition
0	Plenum Station / Engine Upstream Station
1	Generic Upstream Station / End of Intake Station
2	Experimental Rake Station / Generic Downstream Station
θ	Circumferential Quantity
Ax	Axial
d	Design Condition Quantity
E	First Captured Mach Wave Quantity
i	Engine Inlet Station
j	Engine Exhaust Station
Max	Maximum

P	Plenum Station
ss	Suction Surface Quantity
t	Total Quantity
u	Tangential Quantity
x	Local Station

Superscripts

o	Total Quantity
*	Sonic Conditions
'	Relative Velocity Component

Chapter 1

Introduction

1.1 Background

Starting in the past few decades, a revived interest in the supersonic transport (SST) for civil applications is catching on. The main problems associated with this market have always been represented by emissions and noise regulations, rather than the feasibility of SST itself, already used in military applications. For instance, the well known Concorde project underwent some restrictions which caused the takeoff and landing ban from some airports, causing an immense loss concerning revenues. Future emissions regulations, mostly related to the production of oxides of Nitrogen at high altitudes, are believed to be solved by acting directly on the combustor design or by using alternative fuels. Hence, takeoff and landing noise restrictions, which are becoming progressively more stringent, represent the real challenge for this sector. During such flight phases, the primary source of noise is represented by the engine jet noise, which is proportional to the engine jet velocity.

During supersonic flight, a high specific thrust is desirable since it corresponds to a smaller engine cross-sectional area, and so to a lower aircraft drag. For a fixed cycle engine (FCE), defined as an engine able to operate efficiently only under one specific flight condition, a particular specific thrust requirement for the cruise phase corresponds to a

higher takeoff one, due to the thrust reduction caused mainly by the decrease of the air pressure during the climb. Based on thrust definition, for a fixed inlet mass flow, a higher specific thrust corresponds to a higher jet velocity and therefore to a higher jet noise¹. For such engines, heavy noise suppressors are required in order to meet the noise restrictions, corresponding consequently to poor performances. Based on such considerations, many new propulsion system concepts for SST use have been investigated starting in the 1970s, all developed in order to overcome the noise limit problem while maintaining good performances. Both conventional and variable cycle engine concepts were analysed. A variable cycle engine is defined as an engine able to operate efficiently under multiple flight conditions. The idea behind a variable cycle engine is to improve both performance and noise reduction by using unorthodox systems such as variable geometry components and extra bypass ducts. However, such a design leads to a considerable increase in weight and complexity when compared with an FCE.

Towards the end of the decade, an alternative concept arose: the supersonic through-flow fan (SSTF) engine. This particular engine can operate with axial supersonic inlet flow resulting, theoretically, in a lighter and simpler solution². Moreover, during supersonic inlet conditions, it has the peculiar characteristic of causing a reduction in mass flow while increasing the rotational speed, which is the opposite behaviour of a subsonic compressor. This feature is the one which permits to operate with a high amount of mass flow and low jet velocity during takeoff (low noise) while using a low amount of mass flow and a high jet velocity during the supersonic cruise (high specific thrust). Due to the competitive results demonstrated by the SSTF engine during past preliminary performance comparison with the other concepts, NASA designed, produced and tested a single stage supersonic through-flow fan in order to prove the feasibility and the real performance potential of the SSTF engine. Relevant experimental data were released about the isolated supersonic through-flow rotor.

Recent studies have shown better performance for SSTF engine with a different con-

¹For further information check Appendix [A.1](#)

²The reasons behind this statement are explained in section [2.1.4](#)

figuration from the single stage one³. Hence, the possible performances of an SSTF engine have not been fully explored yet. A first step in doing so is the detailed study of the single supersonic through-flow rotor.

1.2 Thesis Aim and Objectives

The thesis aim is to model and investigate the isolated supersonic through-flow rotor previously tested by NASA, focusing on the effects of geometry variations on isentropic efficiency and total pressure ratio. The project objectives can be summarised as follows:

- To study the NASA test facility in order to understand the inflow supersonic starting/unstarting process which relates to the possible performances instabilities and the different rotor operating modes.
- To create a blade model of the isolated rotor based on the design proposed and tested by NASA and validate it by comparing the subsonic and supersonic experimental results against numerical 3D CFD solutions.
- To provide the reader with a deep understanding of the aerodynamic behaviour of the isolated rotor, relating it to its performance aspects where possible.
- To use the validated model in order to carry out a subsequent optimisation process based on the possible blade angle and thickness distributions in order to maximise isentropic efficiency and total pressure ratio.

³For further information check section 2.1

1.3 Document Structure

The thesis consists of a total of five chapters. In order to help the reader, the organisation of the chapters is listed below:

- *Chapter 1* (the current one) introduces the background information, aim, objectives and structure of the thesis.
- *Chapter 2* reports the full literature review, including the historical background, a full description of the test facility used by NASA and an introduction to the aerodynamic behaviour of the isolated rotor during all its operating modes.
- *Chapter 3* shows a description about the used methodology including the blade modelling, the domain choice, details about the CFD analysis such as boundary conditions, mesh dependency study, turbulence model dependency study and the criteria behind the validation process. The criteria and the algorithms used for the optimisation process are analysed.
- *Chapter 4* contains all the commented results about both the CFD validation and optimisation processes, including a deep analysis of the flow characteristics of both the original and optimised blade.
- *Chapter 5* includes both the conclusions and suggested future work.

Chapter 2

Literature Review

Due to the growing interest in SST for civil applications, several companies have developed their supersonic engine concepts. Nowadays, the trend is toward turbojets or low-bypass engines provided with variable compressor bleed or bypass ratio. Another valid concept is the tandem fan engine which operates as a regular bypass engine during supersonic flight but, at subsonic speed, an inlet and nozzle bypass is open in order to achieve lower specific thrust. More information about such an engine can be found in the European patent [1].

Additional information on current supersonic engine development comes from the NASA Lewis Research Center (now renamed NASA Glenn Research Center). In the 70s, NASA proposed and compared the performance of six new engine concepts, including the SSTF engine. NASA is the only corporation that has studied the SSTF engine concept so far. Hence, no direct performance comparisons between such engine and the ones not included in the NASA program are available in the public domain. Due to the promising results recorded by the SSTF engine studies, NASA then developed and tested a single stage supersonic through-flow fan. The purpose of this chapter is to provide the reader with a general description of such studies, including the engine performance comparisons, the historical development of the fan, the test facility characteristics and the isolated rotor operating modes.

2.1 SSTF Engine Performance Comparisons

In order to prove the SSTF engine potential, a series of performance comparison studies were carried out between the SSTF engine and the new supersonic engine concepts proposed by NASA. The turbine bypass engine (TBE), the variable stream control engine (VSCE), the conventional mixed-flow turbofan (MFTF), the Fan-on-Blade (Flade) engine and the TBE provided with an Inlet Flow Valve (TBE/IFV) were included in the investigation. Conceptual schemes of some of the cited engines are presented from Figure 2.1 to Figure 2.4. It is necessary to point out that all the performance calculations were carried out through a one-dimensional steady-state thermodynamic analysis code, fully described in the work of Plencner and Snyder [2].

2.1.1 SSTF Engine - TBE

A preliminary comparison between the SSTF engine and the turbine bypass engine has been done by Franciscus and Maldonado [3]. The TBE is a variable cycle turbojet engine provided with a compressor bypass system which drives part of the air directly into the nozzle when a lower power setting is required. For a supersonic intake, a reduction of inlet mass flow corresponds to an off-design condition which leads to an increase of inlet spillage drag¹. Thanks to the bypass system, the TBE can reduce the power settings without reducing the inlet mass flow so maintaining a low inlet spillage drag.

A flight mission comparison between the SSTF engine and the TBE is shown in Figure 2.5. The figure shows the maximum possible mission range expressed in nautical miles as a function of the engine mass flow at takeoff expressed in pounds over seconds, which is directly related to the engine size. The chart also shows the takeoff noise reduction required for each configuration, based on the Federal Aviation Regulation (FAR) part 36 updated to 1993. Cruise Mach number and takeoff weight are fixed for both engines. Due to testing data uncertainty, the SSTF engine is represented as a band in which the

¹Further information are reported in Appendix A.2

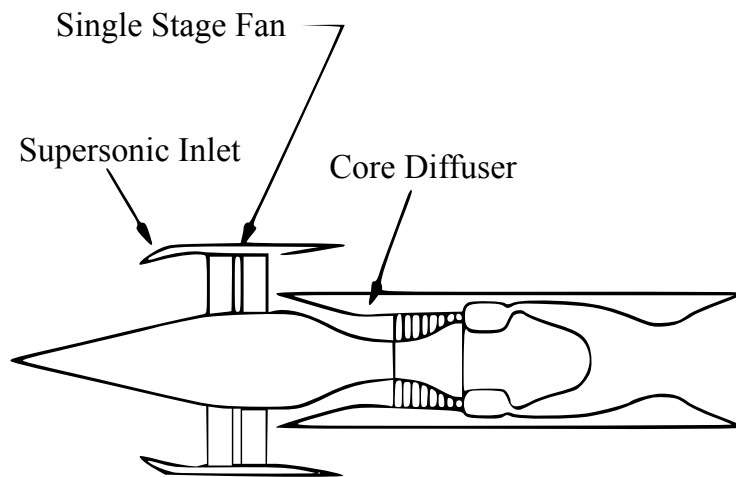


Figure 2.1: Supersonic Through-Flow Fan Engine [4, pp.2]

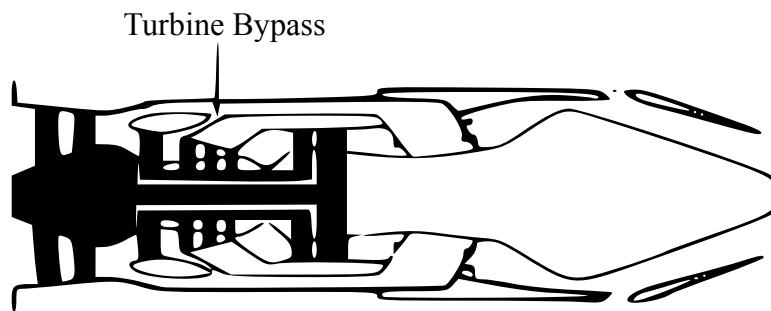


Figure 2.2: Turbine Bypass Engine [5, pp.5]

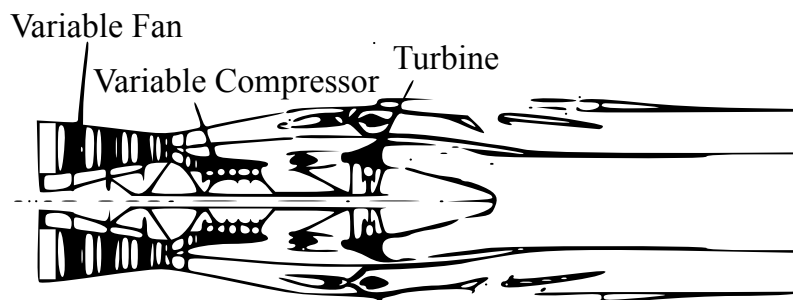


Figure 2.3: Variable Stream Control Engine [6, pp.350]

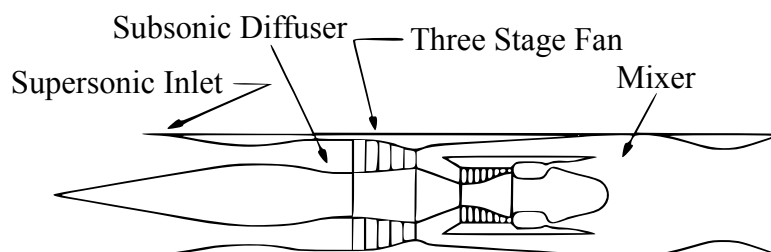


Figure 2.4: Conventional Mixed-Flow Turbofan Engine [4, pp.2]

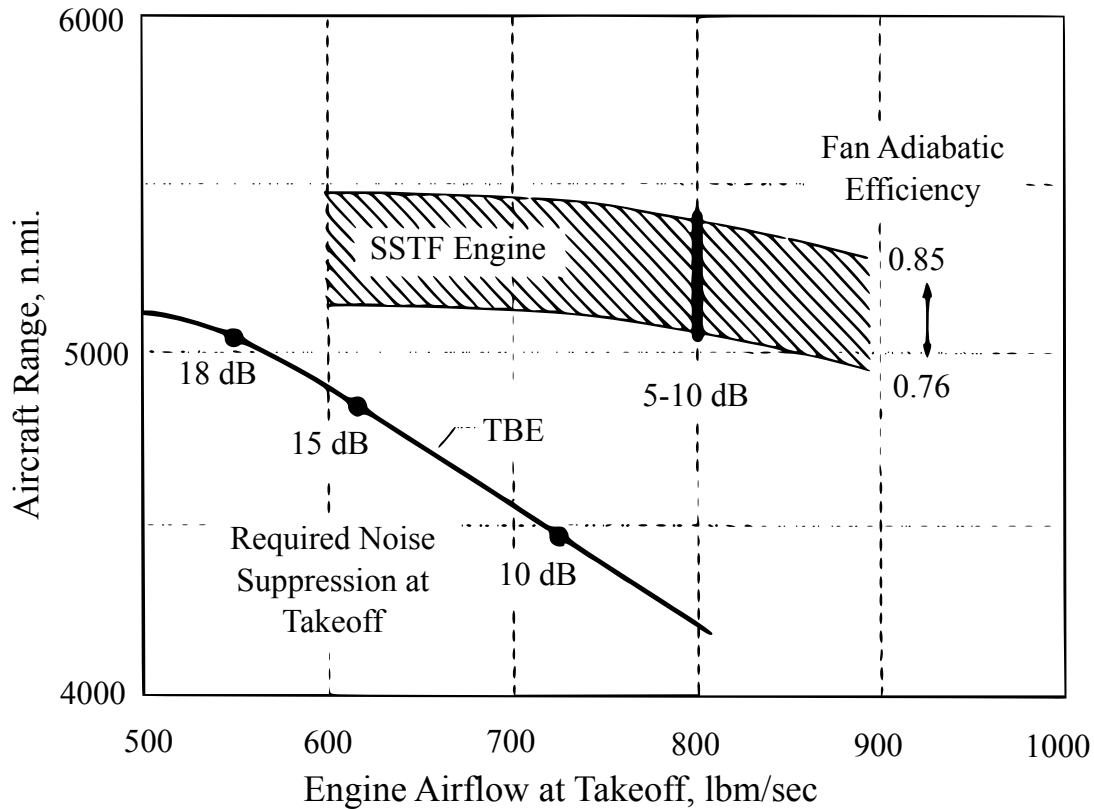


Figure 2.5: Flight mission benefit of the SSTF engine over the TBE [7, pp.4]

fan adiabatic efficiency changes. For a fixed engine dimension, a higher efficiency corresponds to lower specific fuel consumption (SFC) and so to a higher possible mission range. For a fixed thrust, a higher mass flow at takeoff corresponds to a lower jet velocity and so to a lower required noise reduction. At the same time, this leads to a bigger and heavier engine, causing a reduction in the possible mission range. It can be observed that the SSTF engine requires a limited noise reduction if compared with the TBE. Moreover, the eventual implementation of noise suppressors for the SSTF engine does not represent a problem since, at the current technology level, a noise reduction of about 5-10 dB is possible with a competitive performance trade-off. For a 5,000 miles mission at a speed of Mach 3.2, the SSTF engine aircraft resulted 13% lighter than the TBE one.

2.1.2 SSTF Engine - VSCE

Between the variable cycle engine concepts, the variable stream control engine was also analysed. A full description of such concept can be found in the work of Howlett [6]. The engine operates by using a variable geometry multi-stage fan and a variable geometry high-pressure compressor. Such feature permits to regulate the core and the bypass streams separately, resulting in a different jet velocity for the two ducts. It has been observed that, for fixed mass flow and thrust level, a bypass duct jet velocity significantly higher than the core one produces a reduction in jet noise when compared with a single-stream jet. However, a study presented by Franciscus [8] have proven better performances for the SSTF engine, which indicated 20% more mission range, 12% lower SFC and 30% less weight if compared with the VSCE.

2.1.3 SSTF Engine - MFTF Engine

More recent is the study done by Berton et al. [9] where the performances of several propulsion systems for high-speed civil transport were compared, SSTF engine excluded. The results showed how the conventional mixed-flow turbofan engine is the best choice among all the compared configurations which included the TBE, the Flade engine and the TBE/IFV. A full description of such concepts is reported in the same study. Here the discussion is focused on the MFTF since it resulted in the best configuration.

The MFTF is a turbofan engine provided with a mixer downstream of the turbine which forces the bypass flow to rejoin the core one. Doing so results in lower jet velocities and therefore in a quieter engine than a comparable one. A study done by Tran [10] compared an SSTF engine equipped with a supersonic through-flow rotor followed by a supersonic counter-rotating diffuser (SSTR/SSCRD) with the modern MFTF engine. The purpose of the supersonic counter-rotating diffuser is to diffuse the flow up to axial subsonic conditions. A subsequent subsonic stator then removes the flow swirl. Such configuration resulted lighter and more efficient if compared with a single stage SSTF

engine, in which the diffusion process relies on a heavy and complex core engine duct. The study focused on both the weight and on the thermodynamic cycle analysis for a 5,000 miles range mission at a Mach 2.4 by using the same aircraft. The results showed an engine 32% lighter and an aircraft operating empty weight 3% lower if compared to the MFTF configuration. However, improvements are needed concerning fuel consumption since the SSTR/SSCRD engine configuration resulted in 19% additional fuel weight.

2.1.4 SSTF Engine Overall Advantages

Based on the studies made, the SSTF engine advantages over other configurations can be summarised as follows:

- The SSTF can achieve very high total pressure ratios across the stage. This means that a multiple-stage fan, usually present in conventional supersonic engines, is not necessary, resulting in a lighter solution.
- During supersonic flight, for a fixed rotational speed, the SSTF covers a wide range of mass flow without almost any change in total pressure ratio² resulting in a wider fan operability range and so in better control.
- The SSTF engine does not need a subsonic flow at the inlet. Hence, a diffusion process to subsonic conditions is not necessary for the upstream flow. That results in a lighter and less complex intake. The variable geometry feature for the intake could still be present in order to start the inlet flow during supersonic flight.
- Thanks to the inverse relationship between mass flow and rotational speed during supersonic flight, an SSTF engine is able to replicate the behaviour of a VCE but with a lighter configuration, resulting in a better performance.
- SSTF engine can overcome the takeoff and landing noise restrictions also showing very competitive performances when compared with other configurations.

²Characteristic described in both the impulse-type and supersonic rotor operating modes sections, 2.4.2 and 2.4.4

2.2 Historical SSTF Development

An engine capable of accepting axial supersonic inlet flow was first theorised by Ferri [11], who in his work described how such an engine would allow the use of a lighter and simpler intake. Ferri focused on an engine that operates with a shock in the fan rotor passage, resulting in a subsonic outflow suitable for feeding the core compressors. However, due to the presence of the shock, such configuration presented a limited efficiency. A direct evolution of this concept is the SSTF engine, first studied by Trucco [12], in which the flow is axial supersonic throughout the whole fan. Due to the supersonic outflow conditions, such configuration still needs a core diffuser whose purpose is to diffuse the flow to subsonic conditions. Since the losses are only confined to the fraction of air which diffuses before entering the core, the SSTF is overall a more efficient configuration.

Supersonic compressors, referring to compressors with a supersonic flow in the relative frame of reference, were first investigated in 1940's due to their high work capability, allowing a reduction in the number of stages. Such compressors were tested at subsonic inlet conditions and at shock-in-rotor operating mode³. During the same years, supersonic compressors with axial supersonic inlet were not tested for prolonged time intervals, resulting in the lack of experimental data for such a concept. The reason behind that has to be associated to the fact that the SSTF engine concept was initially considered not a feasible one due to the poor technology level, especially concerning material science. Only three programs involving axial supersonic inlet are known to have been run in the past, most of them based on the testing of the isolated rotor. The first one, run by Wilcox et al. [13], took place at the NACA Langley Aeronautical Laboratory during the 1960's, where a rotor with an inflow Mach number of 1.5 was tested, but no relevant data were released. Breugelmans [14] run another one during the 1970's, but apparently, the rotor failed before reaching the design rotational speed. The third and last one, the NASA Lewis Supersonic Through-Flow Fan Program, started in 1986 and went on for more than

³Operating mode in which a shockwave is present inside the blade passage resulting in a subsonic outflow

a decade. The program aimed to demonstrate the feasibility and performance potential of the SSTF engine, accompanied by a full description of the rotor aerodynamic behaviour in all its operating points.

Since no experimental data existed at that time, a baseline fan design has been developed by NASA by following the criteria listed below:

- A stage pressure ratio of 2.45 and a design mechanical tip speed of 1908 ft/sec were required.
- The shock waves at both the LE and blade passage had to be weak in order to avoid a too high blade loading and a low performance due to total pressure losses.
- A constant annulus area was required in order to minimise possible 3D effects caused by a reduction of such area. That was a direct consequence of no proper 3D analysis codes available at that time.
- The static pressures at the TE on both the suction and pressure surface had to be as similar as possible in order to avoid sudden outflow adjustments resulting in total pressure losses.

Starting from such design, since no experimental data were available, NASA used a series of in-house codes involving blade profile design, CFD, structural analysis and flutter potential analysis in order to perform an iterative design procedure. Details and considerations about the design loop are reported in the work of Schmidt et al. [15]. The outcome of such loop is a single SSTF stage, which characteristics are summarised in Table 2.1. Although the design loop was run for the development of a full stage, only experimental results about the isolated rotor will be considered in this document.

Table 2.1: Final SSTF stage characteristics [7, pp.17]

Property	Rotor	Stator
Rotational speed, rpm	17188.7	-
Total-pressure ratio	2.70	-
Blade number	44	52
Tip radius, inches (constant)	10.0	10.0
Hub radius, inches	7.0	7.0
Aerodynamic chord, inches (tip/hub)	4.45/3.56	3.65/3.28
Aspect ratio, span to mean chord	0.97	0.86
Blade element solidity (tip/hub)	3.11/3.56	3.02/3.88
Max. thickness/chord, percent (tip/hub)	4.0/7.0	5.0/5.0
LE thickness/chord, percent (tip/hub)	0.45/0.56	0.41/0.46
TE thickness/chord, percent (tip/hub)	0.81/1.12	0.82/0.82
LE ellipse major/minor length ratio	1.5	1.5
TE ellipse major/minor length ratio	1.5	1.5

2.3 Test Facility

The test facility in which both the isolated rotor and the full stage were tested was located at NASA Lewis Research Center. Initially, the facility was designed to test multistage compressors, not suitable for hosting the SSTF. In order to accommodate the SSTF, the facility underwent different modifications which are fully described in the work of Urasek et al. [16]. A general description of the test facility used for testing the isolated rotor is argued in this section. Details about geometry and data acquisition location are provided. Such information is crucial to determine the domain characteristics and the position of the probing stations to be used during the CFD validation process. The supersonic starting process is also reported since it can be related to the switch between the different rotor

operating modes. A description of the facility used for testing the full stage can be found in the work of Moore et al. [17].

2.3.1 Facility Scheme and Instrumentation Location

A scheme of the used test facility is presented in Figure 2.6. The air flows from the bottom (pressurised air supply) to the top (altitude exhaust). Dry air is supplied from an external facility in order to avoid condensation shocks during the supersonic flow starting process. However, it is possible to add humid air from an external atmospheric air filler. The pressurised dry air flows through an ASME standard orifice from which the fan inlet airflow is measured. The static pressure and the mass flow are regulated by two inlet throttle valves which drive the flow to the plenum. A security rupture disk is mounted on the plenum in order to avoid unexpected increases of static pressure. The air is then driven inside a variable geometry test package in which the rotor is mounted. The flow is regulated by a collector followed by an altitude exhaust system integrated with a series of vacuum bleed pumps directly connected to the test package. The rotor is driven by an external electric 15,000-hp motor provided with a 5.21:1 gearbox. A detailed scheme of the test package is reported in Figure 2.7. The supersonic axial flow starting is possible thanks to the variable geometry feature provided by translating components for both the nozzle and the diffuser. The non-curved constant area domain extends from 5.990 inches upstream of the rotor leading edge to 9.919 inches downstream of it at the shortest configuration possible (from point A to point B).

The test package was provided with pressure, temperature, flow rates and stress sensors. The data acquisition system was not equipped with fast-response sensors. Hence, only a steady-state analysis was carried out. Such measurement system, called Escort, is fully described in the work of Fronek et al. [19]. A pressure rake element for the measure of total pressure was positioned at 6.414 inches downstream of the rotor hub leading edge as shown in Figure 2.8. A temperature rake element was positioned at 7.613 inches downstream of the rotor hub leading edge.

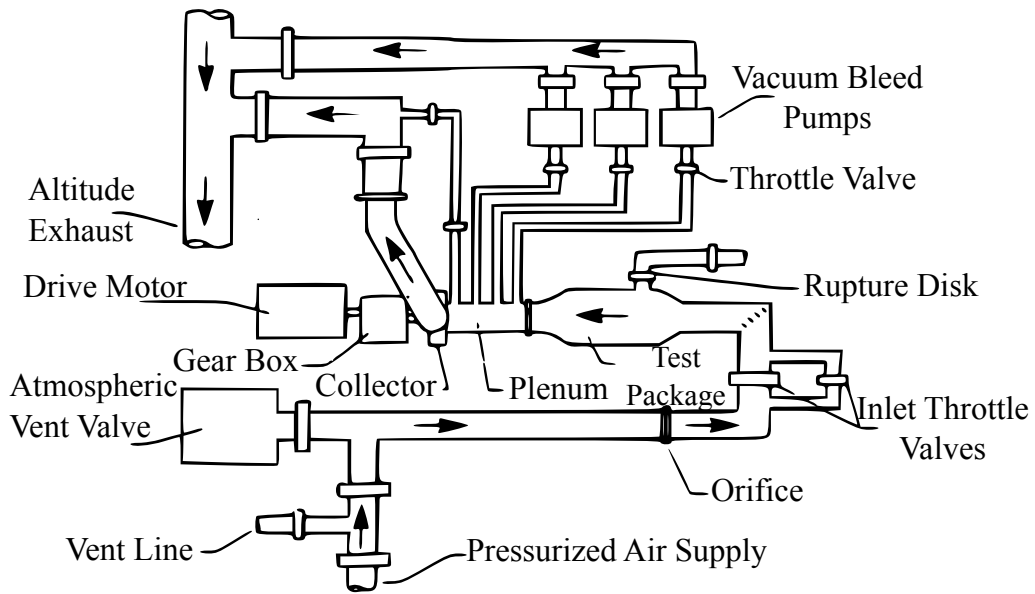


Figure 2.6: Test Facility Scheme [7, pp.25]

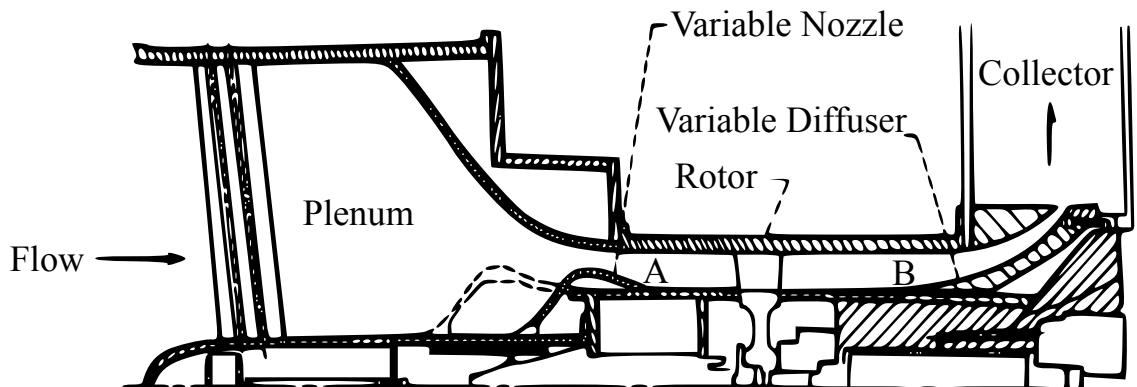


Figure 2.7: Test Package Scheme [18, pp.12]

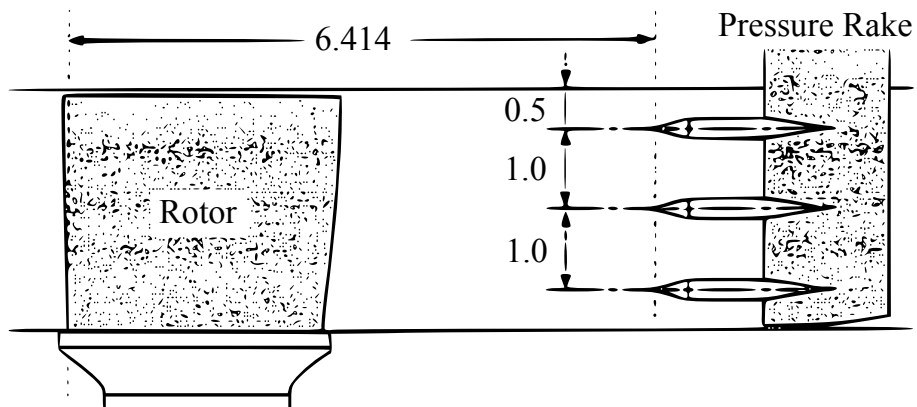


Figure 2.8: Pressure Rake Element Location [7, pp.28]

Rotor inlet Mach numbers, total pressure ratio and rotor isentropic efficiency were calculated with the following relations derived from fundamental gas dynamics and one-dimensional thermodynamic analysis:

$$M = \sqrt{\frac{2}{\gamma-1} \left[\left(\frac{P_2^o}{P_1} \right)^{\frac{\gamma-1}{\gamma}} - 1 \right]}; \quad (2.1)$$

$$PR = \frac{P_2^o}{P_p^o}; \quad (2.2)$$

$$\eta_R = \frac{\left(\frac{P_2^o}{P_p^o} \right)^{\frac{\gamma-1}{\gamma}} - 1}{\left(\frac{T_2^o}{T_p^o} \right) - 1}; \quad (2.3)$$

Ideal air was considered for all the calculations ($\gamma = 1.4$). Regarding the inlet Mach number computations, the total pressure considered was the plenum one, while the static pressure was measured at two inches upstream of the rotor leading edge for subsonic inflow and at one inch upstream of the rotor leading edge for supersonic inflow. The total pressure ratio was computed as the ratio between the total pressure at the pressure rake location and the plenum. The temperature ratio was computed between the plenum total temperature and the one at the temperature rake location measured via the static temperature. All the measurements were circumferentially mass-averaged. The station positions are presented in Figure 2.9. A summary of the test package geometry and measurement locations for performance purposes is provided in Table 2.2.

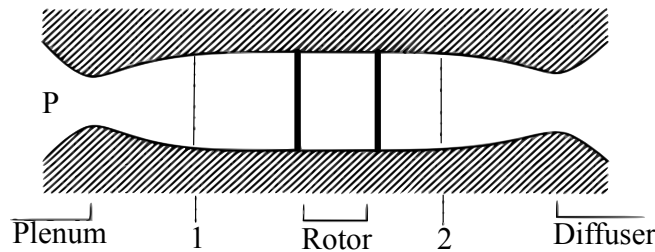


Figure 2.9: Stations Location

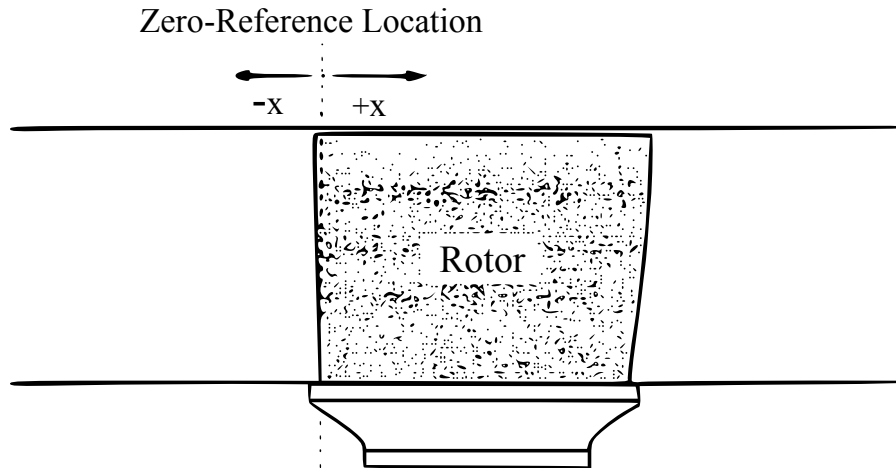


Figure 2.10: Rotor Zero-Reference Location [7, pp.27]

Table 2.2: Test Package Geometry and Measurement Locations

Data	Location [inches]
Non-curved constant area domain inlet (shortest configuration)	-5.990
Non-curved constant area domain outlet (shortest configuration)	+9.919
Inlet total pressure	Plenum
Inlet total temperature	Plenum
Inlet static pressure (subsonic inflow)	-2.0
Inlet static pressure (supersonic inflow)	-1.0
Outlet total pressure	+6.414
Outlet total temperature	+7.613

2.3.2 Supersonic Starting Process

The following discussion is based on a one-dimensional gas dynamics analysis. The supersonic starting process is driven by the sections in which the flow could experience an area reduction in the test package. Such sections are three: the nozzle and the diffuser throats due to the variable geometry feature and the section where the rotor is located since the blade passage area that the upstream relative flow sees depends on its rotational

speed. A scheme of the test package with the cited sections is shown in Figure 2.11.

During subsonic testing, the plenum total pressure was equal to the standard sea-level one, while the collector static pressure was about 20% of the standard one, resulting in a total-to-static pressure ratio of about five. Such condition corresponds to at least one of the three sections to be choked, that is a unitary Mach number across the section itself. During the start-up process, the choked section was the diffuser one. Hence, the flow resulted in all subsonic axial velocities except for the diffuser throat where a sonic condition was present. In order to get an axial supersonic rotor inflow, a choked section upstream of the rotor followed by a divergent geometry is needed, so that the flow can accelerate after the choked section. Such characteristic was reproducible by using the nozzle variable geometry feature which resulted in a smaller nozzle throat followed by a divergent section, as shown by the dashed line in Figure 2.11. Despite the presence of a choked section followed by a divergent section, no supersonic flow was recorded inside the test package. That occurred because, in order to have a stable condition in which two choked sections are present, a normal shock has to exist between them. The presence of the shock prevents the flow to be supersonic after it. Furthermore, the stable shock position was always located in the divergent part of the test package just after the nozzle, resulting in a rotor subsonic axial inflow.

In order to better understand how to get a supersonic flow starting from this condition,

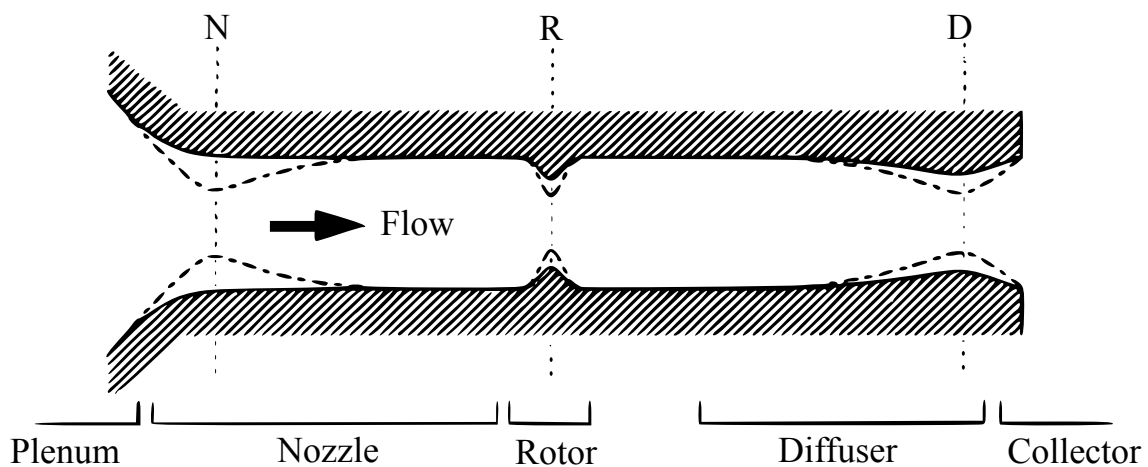


Figure 2.11: Test Package with Possible Area Reduction Sections [7, pp.59]

a duct with two choked sections among which a normal shock is present in the divergent part is represented in Figure 2.12. The duct presents a maximum area at a specific location (A_{max}), in which the divergent part finishes and the convergent one starts. It is essential to keep in mind that the stable shock location is always placed in the divergent part of the duct, no stable locations are possible in the convergent one. By applying the mass flow conservation law on the two choked stations, it is possible to obtain the following expression:

$$\frac{A_1^* P_1^{*o}}{\sqrt{RT_1^{*o}}} f(M_1^*) = \frac{A_2^* P_2^{*o}}{\sqrt{RT_2^{*o}}} f(M_2^*); \quad (2.4)$$

For a duct flow supposed adiabatic, isoenergetic, steady and considering the Mach number unitary in both the choked stations, the expression can be simplified as follows:

$$\frac{A_2^*}{A_1^*} = \frac{P_1^{*o}}{P_2^{*o}} \geq 1; \quad (2.5)$$

Due to the loss generated by the normal shock, the total pressure at the second choked section has to be lower than the total pressure at the first one. As shown in Equation 2.5, this implies that the second choked area must be larger than the first one, which in our case means a diffuser throat bigger than the nozzle one. It is clear from Equation 2.5 that by increasing the second choked throat or by decreasing the first one, the strength of the shock has to increase, resulting in higher losses. That is possible only if the flow

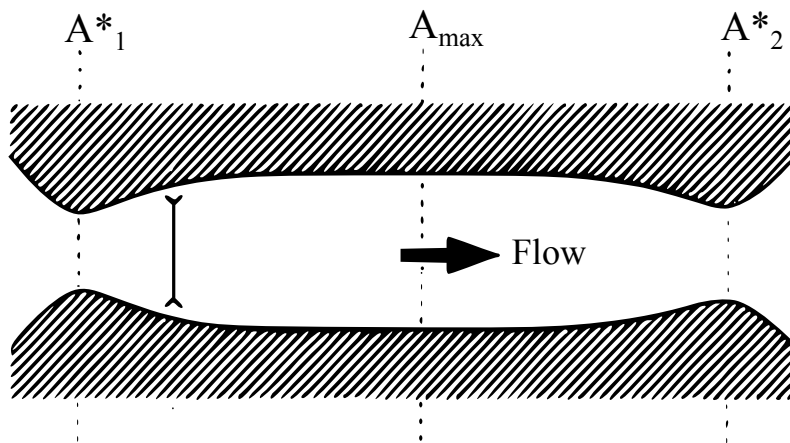


Figure 2.12: Stable Condition in a Duct with Two Choked Throats [7, pp.64]

upstream of the shock gets faster. Such condition occurs if the flow can accelerate more than before, which means that the flow has to pass through a more extended divergent portion of the duct. In other words, an increase of the second choked throat or a decrease of the first one corresponds to a new shock stable position which is situated downstream of the previous one, allowing the flow to accelerate more than before as shown in Figure 2.13. Since a stable location for the normal shock is always situated in a divergent portion of the duct, the limiting condition occurs when the shock is placed at the maximum duct area (A_{max}). If the ratio between the two choked sections is still increased, since the duct section becomes convergent, the normal shock does not find a stable location which is located both after the maximum duct area and inside the duct itself. That results in the jump of the shock directly to a new stable location which will be located somewhere downstream of the duct resulting in a supersonic flow between the two choked sections.

The test package can be considered as constituted by two divergent-convergent ducts: the nozzle-rotor and the rotor-diffuser ones as can be seen in Figure 2.11. Considering the nozzle-rotor duct portion and starting from the condition in which the normal shock was present just after the choked nozzle, based on the discussion done above, the axial supersonic rotor inflow is obtained by reducing the nozzle throat beyond the choking condition. The new stable shock location after the maximum duct area will be situated inside the blade rotor passage resulting in a shock-in-rotor configuration with supersonic

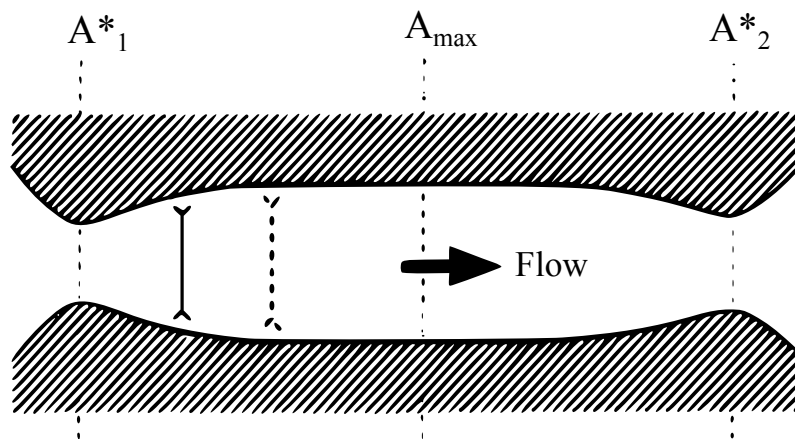


Figure 2.13: New Stable Shock Condition [7, pp.66]

rotor inflow but subsonic rotor outflow. In order to get both a supersonic inflow and outflow, the supersonic starting process has to be done also for the second portion of the test package. That is achieved by moving the shock from the blade passage to the collector located downstream of the diffuser. In such condition, the two choked sections will still be the nozzle and diffuser ones. That can be done by either decreasing the nozzle throat or increasing the diffuser one. Since a decrease of the nozzle throat corresponds to a higher Mach number into the rotor and therefore to a stronger shock inside the blade passage⁴, the second option is desirable. The result of this process is the rotor operating in supersonic through-flow mode with the nozzle throat being the only choked one. The steps to be done in order to obtain a supersonic through-flow rotor operating mode can be summarised as follows:

- After the facility start-up which results in the choked diffuser throat (subsonic through-flow operating mode), the presence of a second choked throat is also necessary. That is done by reducing the nozzle throat thanks to the variable geometry feature. The diffuser throat area has to be bigger than the nozzle one.
- Once the nozzle throat is also choked, a further reduction of such area is necessary in order to move the normal shock from the position just downstream of the nozzle to inside the blade passage. Such process results in a supersonic rotor inflow but a subsonic rotor outflow (shock-in-rotor operating mode).
- In order to get also a supersonic rotor outflow, the diffuser throat area has then to be increased until the normal shock moves from the blade passage to a station inside the collector resulting in a supersonic flow inside the whole test package (supersonic through-flow operating mode).

⁴Such condition corresponds to higher blade stresses.

The rotor tested by NASA has the peculiar characteristic of being always choked for rotational speed above 75% of the design one. If the rotor rotational speed is increased over this level just after the facility start-up and without reducing the nozzle throat area, it will result in both a subsonic rotor inflow and a normal shock located between the choked rotor and the choked diffuser, as shown in Figure 2.14. Starting from this condition, the diffuser throat area can be increased resulting in the supersonic starting of the second portion of the test package. Therefore, the rotor will experience subsonic inflow but supersonic outflow (impulse-type operating mode). A supersonic through-flow operating mode can then be obtained by simply reducing the nozzle throat area which results in the supersonic start of the first portion of the test package. The steps for this alternative supersonic starting process are summarised below:

- After the facility start-up which results in the choked diffuser throat (subsonic through-flow operating mode), the rotor rotational speed is increased until it chokes.
- Once the rotor is choked, the diffuser throat area is increased, resulting in a subsonic rotor inflow but in a supersonic rotor outflow (impulse-type operating mode).
- The nozzle throat area is then reduced in order to start the first portion of the test package which will become supersonic (supersonic through-flow operating mode).

Such procedure is generally preferable to the first one since it avoids the shock-in-rotor operating mode improving the blade lifespan.

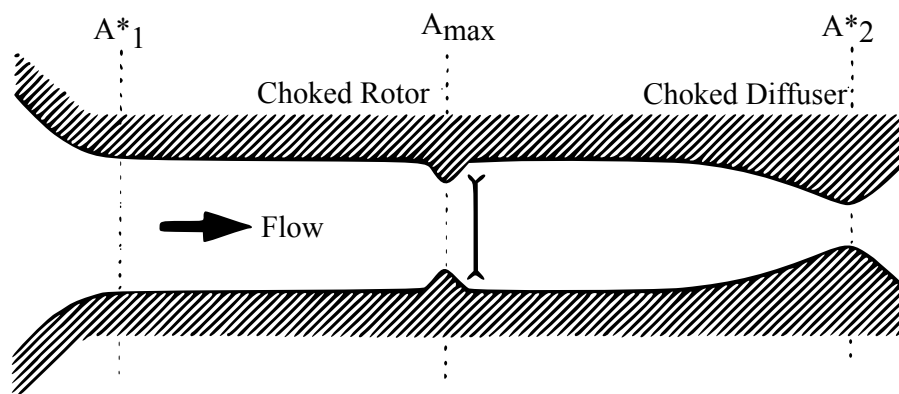


Figure 2.14: Rotor and Diffuser Choked Condition [7, pp.61]

2.4 Rotor Operating Modes

The possible rotor operating modes have already been described in the section dedicated to the test facility supersonic starting, 2.3.2. The operating modes are categorised based on the axial flow characteristics at both the rotor inlet and outlet. A summary of such operating modes is reported in Table 2.3. A more detailed analysis of each operating mode, excluding the shock-in-rotor one, is reported in this section, including the performance maps that will be then used for the blade model validation process.

Table 2.3: Rotor Operating Modes [7, pp.56]

Operating Mode	Rotor Inflow	Rotor Outflow
Subsonic through-flow	Axial-subsonic	Axial-subsonic
Impulse-type	Axial-subsonic	Axial-supersonic
Shock-in-rotor	Axial-supersonic	Axial-subsonic
Supersonic through-flow	Axial-supersonic	Axial-supersonic

2.4.1 Subsonic Through-Flow Mode

The subsonic through-flow operating mode is inevitable and always occurs during the start-up or shutdown of the engine. Hence, it is essential to understand how the rotor behaves in such a condition. As stated before, the subsonic term refers to the axial flow which means that supersonic flows are possible in the relative frame of reference even during subsonic through-flow operating mode. Before proceeding, a brief description of what is a unique-incidence condition is necessary, since part of the rotor performance characteristic is a direct consequence of the presence of such phenomenon.

The unique-incidence condition is the condition which occurs when an axial subsonic flow, a relative supersonic flow and a started supersonic blade passage are present (the passage shock is wholly swallowed). The unique-incidence condition for a flat plate cascade is shown in Figure 2.15. If the incident flow angle is higher than the unique angle (positive incidence), expansion waves will generate from the plate leading edges and, since

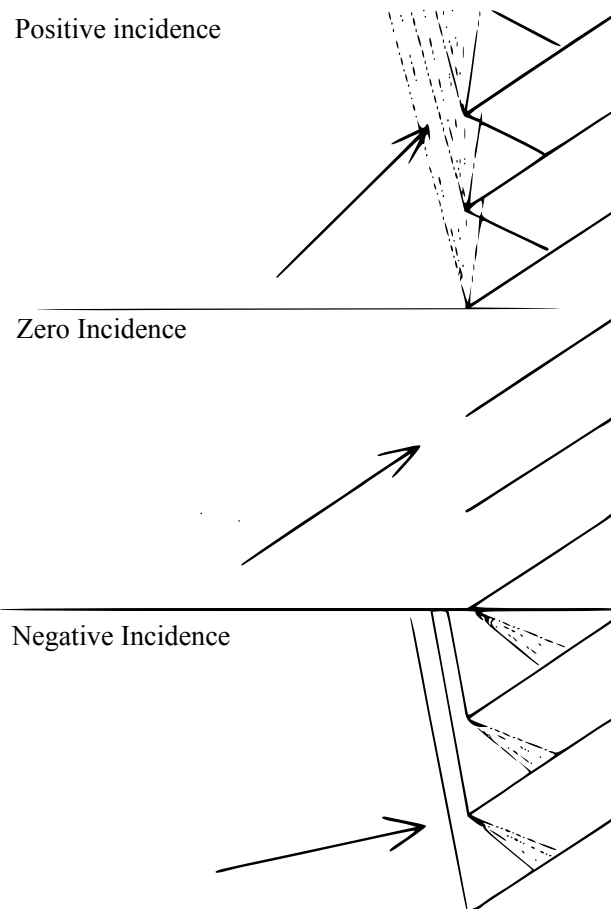


Figure 2.15: Unique-Incidence Condition for a Flat Plate Cascade [20, pp.103]

the axial inflow is subsonic, they will propagate upstream of the cascade. The expansion waves will turn the flow in such a way that it will align with the plates themselves. The same principle applies when the incident flow angle is lower than the unique one (negative incidence), with the difference that the expansion waves will now be replaced by oblique shocks able to travel upstream of the cascade due to the axial subsonic flow condition. The oblique shocks will turn the flow in such a way that it will align with the plates themselves. In other words, during unique-incidence condition, the generation of expansion waves or oblique shocks oblige the flow to enter in the cascade with just one possible incidence, namely the unique incidence. The same principle applies to a blade cascade.

Starken et al. [21] did a full study about the flow behaviour in unique-incidence condition, here only a general discussion is presented. The flow characteristics are shown in Figure 2.16. The blunt leading edge determines the main difference between a flat plate

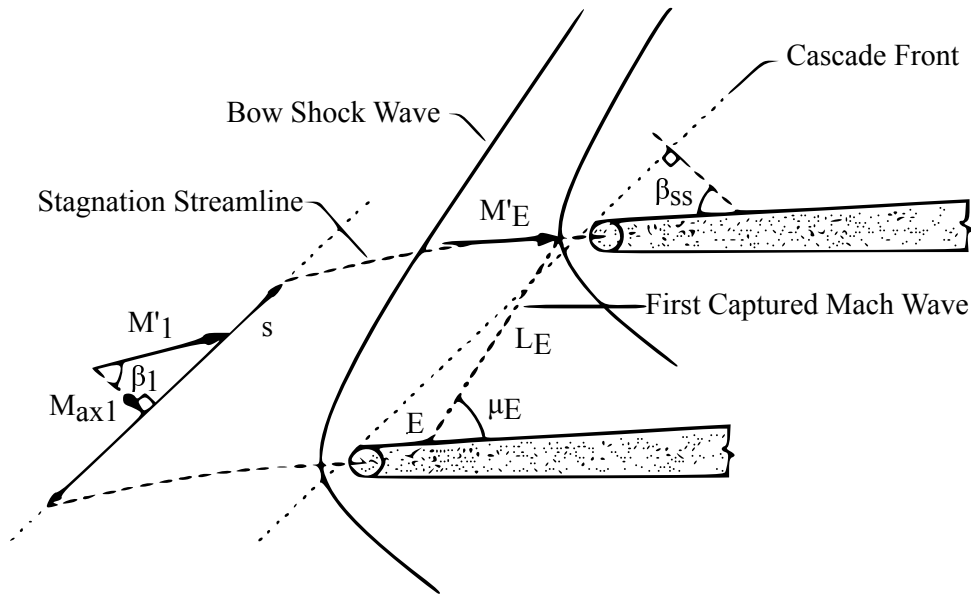


Figure 2.16: Flow Field Model for Unique-Incidence Condition [7, pp.276]

cascade and a blade one. Due to such geometric feature, the simple oblique shocks are replaced by bow shocks which now are present even when the flow incidence angle is equal to the unique one. For a single blade, the shock wave structure results in a series of expansion waves generating from the suction surface present just after the bow shock. Among such expansion waves, the one which determines the amount of mass flow entering in the cascade is called first captured Mach wave. This expansion wave extends from a point E on the blade suction surface to the intersection between the bow shock and the stagnation streamline of the subsequent blade. The Mach number of the flow incident on the cited expansion wave is always equal to one.

The mass flow entering the cascade can be defined as follows:

$$W = \rho_E V_E L_E \sin \mu_E; \quad (2.6)$$

It is clear that the limiting condition is represented by the length of the first captured Mach wave (L_E) and by the angle that such wave forms with the blade suction surface (μ_E). An eventual increase of the relative flow speed⁵ will result in a modification of the

⁵This can be a consequence of an increase of the axial flow speed or an increase of the rotor rotational speed.

wave structure. In particular, the first captured Mach wave generating point (E) will move towards the leading edge of the blade until the wave lies precisely in the cascade front line. During this transition process, the length of the wave increases while the wave angle reduces. The final effect is an increase in inlet mass flow. When the expansion wave lies on the cascade line front, since the incident Mach number is always equal to one, the blade passage can be defined as choked and the entering mass flow will be the maximum one. Further increase of the relative flow speed will result in a fixed position of the first captured Mach wave but in stronger bow shocks which results in a higher shock blockage effect and therefore in a reduction of the mass flow entering in the passage.

The position of the expansion wave generating point (E) is a function of the suction surface angle (β_{ss}) and the relative flow speed (M_1^I). It is possible to carry out a parametric study in order to understand the relationship between such quantities. Straken et al. [21] did such parametric study. The main results are shown in Figure 2.17. The chart shows

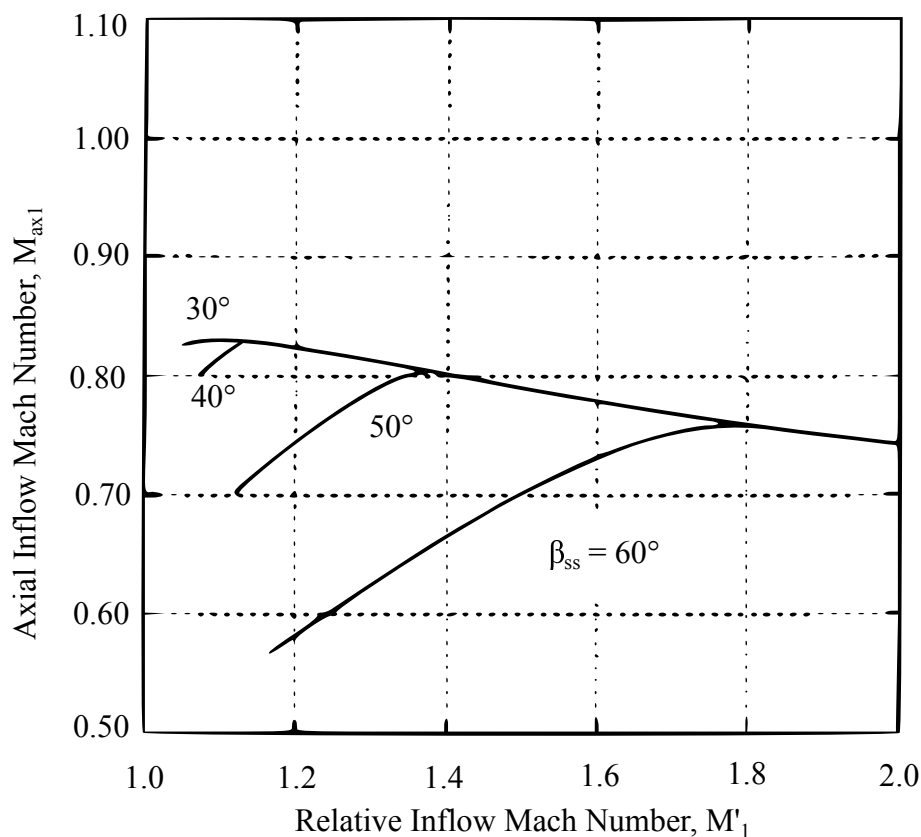


Figure 2.17: Influence of Suction Surface Angle on Inlet Mass Flow [7, pp.282]

the influence of the blade suction surface angle and of the relative flow speed on the axial inflow Mach number which can be related to the inlet mass flow and so to the first captured Mach wave position. For each suction surface angle, there is a condition in which the mass flow is maximum (maximum M_{ax1}). That condition corresponds to the first captured Mach wave lying on the cascade front line which is reached by increasing the relative flow speed. As anticipated, a further increase of the relative flow speed corresponds to a reduction of mass flow (decrease of M_{ax1}). For very low suction surface angles, the maximum mass flow condition occurs as soon as the unique-incidence condition is established. In other words, for such blades, the first captured Mach wave generates directly on the cascade front line. The supersonic through-flow rotor investigated in this document presents a blade suction surface angle from $\beta_{ss} = 32^\circ$ at the hub to $\beta_{ss} = 42^\circ$ at the tip and is, therefore, part of this category. This characteristic also represents the main difference between the supersonic through-flow rotor and a conventional transonic compressor. In a transonic compressor the suction surface angles are generally much higher. Hence, starting from the unique-incidence condition, an increase in rotational speed corresponds to an increase of inlet mass flow. That does not occur in the supersonic through-flow rotor for which, starting from the unique-incidence condition, an increase in rotational speed corresponds to a decrease of inlet mass flow.

The subsonic rotor performance map is shown in Figure 2.18. Due to the reverse mass flow relation for higher rotational speed or higher axial inflow, for the sake of tidiness, all the performance maps are shown as a function of the inlet Mach number. The presence of vertical lines represents a choked blade passage which corresponds to the maximum inlet mass flow for a particular rotational speed. Based on the discussion made so far, the choking condition can be both the result of a higher axial velocity⁶ or of the establishment of the unique-incidence condition. Since such condition occurs when a relative supersonic flow is present, it is firstly established at the tip of the blade where the relative flow speed is higher. For the studied rotor, this occurs at about 60% of the rotational speed. The choking

⁶Such condition corresponds to a lower flow incidence angle and therefore to a gentler diffusion process inside the blade passage resulting in a sonic flow at the passage throat.

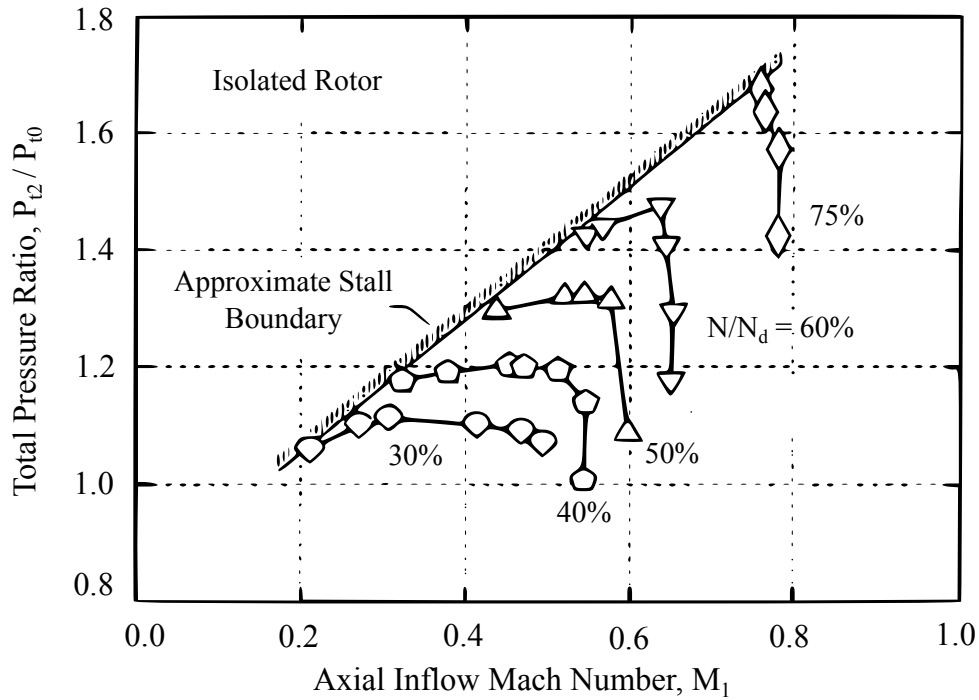


Figure 2.18: Subsonic Rotor Performance Map [7, pp.81]

caused by the unique-incidence condition anticipates others choking processes, resulting in a performance line more and more vertical for higher rotational speed. The relative flow is supersonic in the whole blade at around 75% of the rotational speed, resulting in the establishment of the unique-incidence condition all along the blade. Hence, the speed lines corresponding to rotational speed equal or above 75% are vertical. The presence of a vertical line is a direct consequence of the reached maximum mass flow condition that occurs as soon as the unique-incidence one is established.

2.4.2 Impulse-Type Mode

The impulse-type operating mode is necessary for the supersonic through-flow one to happen. A typical velocity triangle for the rotor outflow is shown in Figure 2.19. Based on the velocity triangle geometry it is easy to derive the following expression:

$$M_2^I = \frac{M_{ax2}}{\cos \beta_2}; \quad (2.7)$$

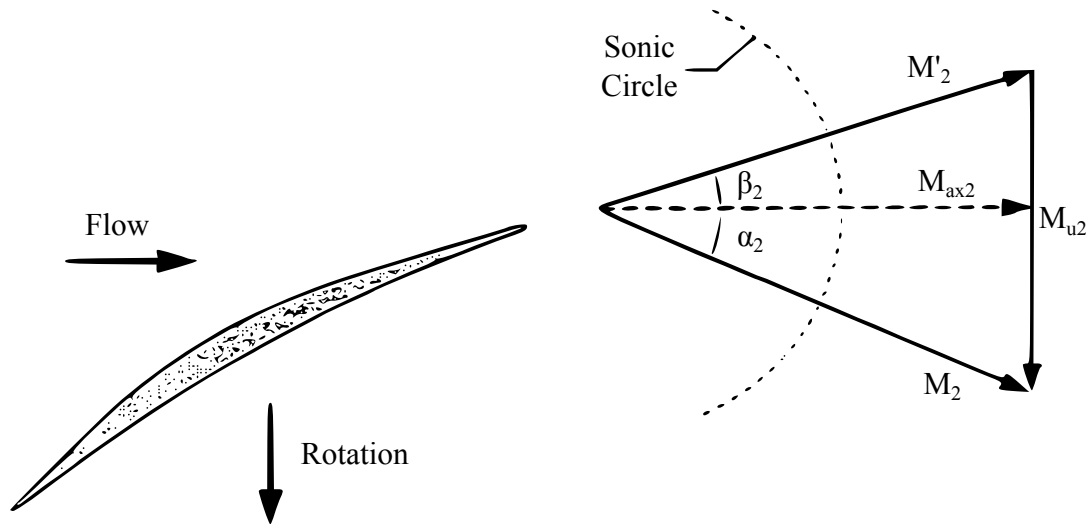


Figure 2.19: Rotor Outflow Velocity Triangle [7, pp.152]

From Equation 2.7 and considering that during impulse-type operating mode the axial outflow velocity has to be supersonic ($M_{ax2} > 1$), it is possible to derive the combination of relative flow velocity and relative outflow angle for which the impulse-type mode is possible. The results are shown in Figure 2.20. The crossed area corresponds to a subsonic axial outflow ($M_{ax2} < 1$) and therefore to an impossible impulse-type operating mode.

During impulse-type mode, the relative outflow angle is more or less aligned with the blade exit angle. The supersonic through-flow rotor is designed with a blade exit angle of $\beta_2 = 15^\circ$ in order to make the establishment of the impulse-type mode as easy as possible. This feature is in contrast with the one of a conventional transonic compressor where high blade exit angles are present preventing the establishment of impulse-type mode. The work done by the rotor in this operating mode can be expressed in terms of total temperature ratio. That is possible by combining the Euler momentum equation applied to the isolated rotor with no inlet swirl (Equation 2.8) with two relations derived from the velocity triangle geometry (Equation 2.9 and 2.10). The results are shown in Figure 2.21.

The dependency of the total temperature ratio from the axial outflow Mach number is increasingly less pronounced with the reduction of the relative outflow angle. For a null relative outflow angle, such dependency disappears as can be seen by imposing $\beta_2 = 0$ in Equation 2.9 and by substituting the resulting expression in Equation 2.8. For blade exit

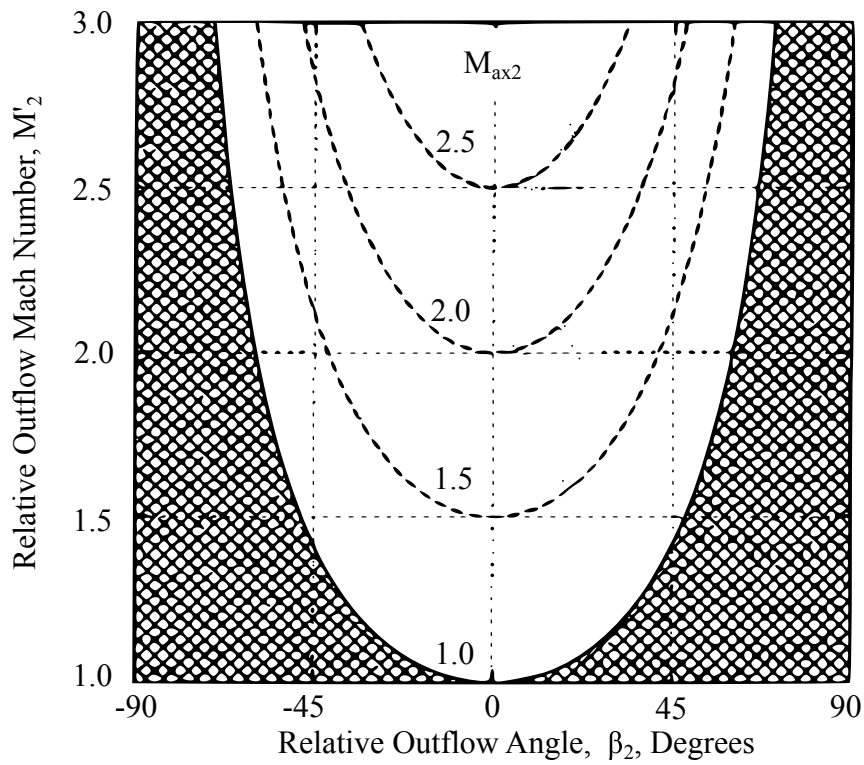


Figure 2.20: Conditions Necessary for Impulse-Type Operating Mode [7, pp.153]

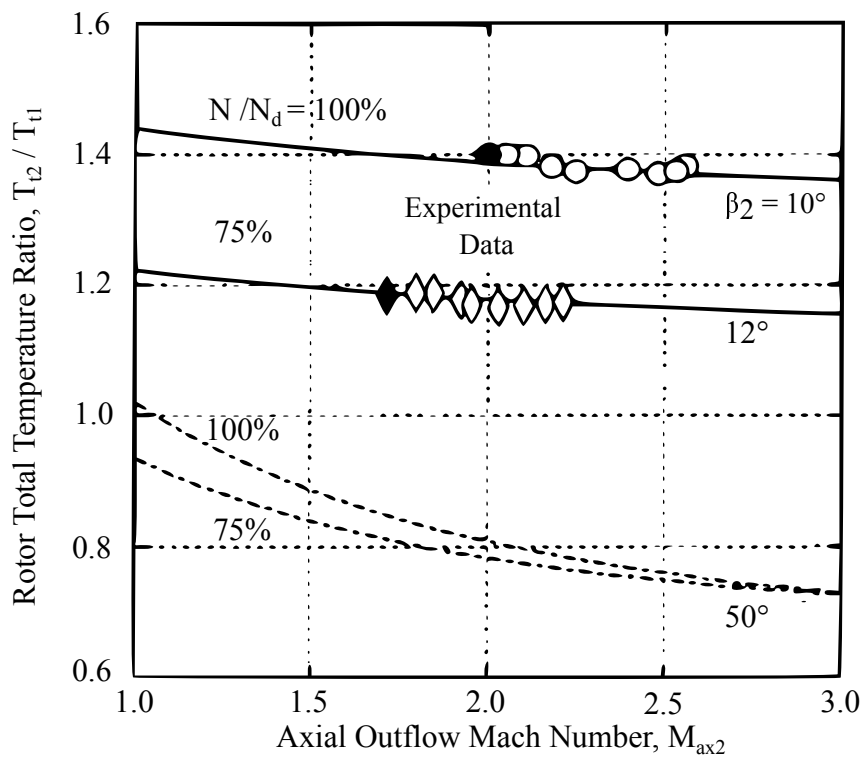


Figure 2.21: Rotor Total Temperature Ratio During Impulse-Type Mode as a Function of Axial Outflow Mach Number and Relative Outflow Angle [7, pp.155]

angles greater than 40° , the isolated rotor behaves like a turbine since the corresponding temperature ratio is less than one, therefore a conventional transonic compressor with a supersonic outflow needs to operate in a shock-in-rotor operating mode in order to do work on the flow⁷. The supersonic through-flow rotor has been designed with a low blade exit angle resulting not only in a total temperature ratio higher than one but also with an almost constant work in a vast range of outflow velocities.

$$\frac{V_{\theta_2}}{a_2} = \frac{\left(\frac{T_2^o}{T_1^o}\right) - 1}{(\gamma - 1) \left(\frac{U_2}{a_1}\right) \sqrt{\frac{T_2^o}{T_1^o}}}; \quad (2.8)$$

$$\frac{\frac{U_2}{a_1}}{\sqrt{\frac{T_2^o}{T_1^o}}} - \frac{V_{\theta_2}}{a_2} = \frac{M_2^I \sin \beta_2}{\sqrt{1 + \frac{\gamma-1}{2} M_2^2}}; \quad (2.9)$$

$$M_2^2 = \frac{\left(\frac{V_{\theta_2}}{a_2}\right)^2 + (M_2^I \cos \beta_2)^2}{1 - \frac{\gamma-1}{2} \left(\frac{V_{\theta_2}}{a_2}\right)^2}; \quad (2.10)$$

2.4.3 Supersonic Inflow Starting

The difference between the impulse-type operating mode and the supersonic through-flow one stands in the supersonic inflow starting. The supersonic inflow is started when, depending on the flow incidence angle, the expansion waves or the oblique shocks are contained in the blade passage, as shown in Figure 2.22. Since the waves are not able to propagate upstream of the cascade due to the supersonic inflow, no unique-incidence condition can exist, and the unique-incidence angle is now defined as zero incidence or nominal incidence angle. The started condition is attainable by increasing the relative flow speed, which means increasing whether the rotational speed, the axial inflow velocity or both. It is possible to determine an unstart boundary beyond which the supersonic through-flow operating mode is established. In other words, for a fixed rotational speed, a minimum axial inflow velocity is required to start the blade passage.

⁷Conventional transonic compressors are designed with a high exit blade angle.

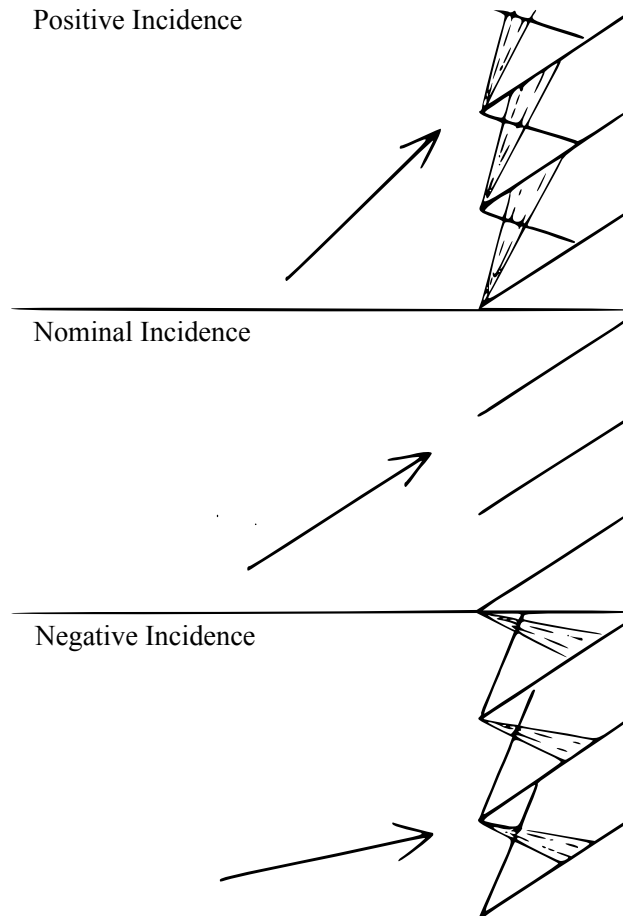


Figure 2.22: Supersonic Inflow Starting Condition [20, pp.104]

Depending on the combination of both the rotational speed and the axial inflow velocity, the unstart condition can correspond to a positive, negative or nominal flow incidence. Lichtfub and Starcken [22] have studied the unstart process for all these configurations. Zero or positive incidence unstart occurs when the expansion waves generating from the blade leading edge interact with the bow shock region next to the leading edge of the adjacent blade, resulting in the propagation of the bow shock upstream of the cascade. Negative incidence unstart occurs when the oblique shock generating in the upper blade surface stands at less than 90° to the axial flow, resulting in a shock propagating upstream of the cascade. For a too low axial inflow velocity, in the supersonic through-flow rotor, positive or zero incidence unstart occurs for a rotational speed equal or above 75%, while for rotational speeds below such value negative incidence unstart occurs.

The same conditions described so far, including limits and flow characteristics, are

valid for the starting process. Moore and Tweedt [23] have studied the rotor performance evaluation during such process. The supersonic axial inflow starting process coincides with the ingestion of the nozzle shock wave inside the blade passage, as described in the test facility supersonic starting section (2.3.2). It has been observed that for a zero or positive incidence start, the expansion waves generating from the blades leading edges during subsonic condition have the same magnitude of the shock entering in the passage. That resulted in shock attenuation and an almost null variation in blade loading, rotor torque and power during the transition phase. On the other hand, a negative incidence start resulted in large discontinuities due to the presence of oblique shocks at the blade passage entrance. Such observation suggests that a supersonic through-flow rotor for a real application should be designed for a positive or zero incidence starting process in order to avoid eventual starting problems due to the required torque discontinuity. That also justifies why experimental results about the supersonic through-flow operating mode are present only for rotational speeds equal to 75% or above.

2.4.4 Supersonic Through-Flow Mode

The supersonic through-flow and impulse-type mode performance map is shown in Figure 2.23. Such map contains experimental results along with results originated from CFD and off-design codes developed by NASA. As stated before, the supersonic through-flow operating mode can be considered as a particular impulse-type mode with axial supersonic inflow, that is why the two operating modes are represented together. Many phenomena discussed so far are present in the map:

- The surge limit is now substituted by the unstart boundary which for a fixed rotational speed occurs for a too low axial inflow velocity.
- The difference in performance between the impulse-type mode and the supersonic through-flow one adjacent to the unstart boundary is almost null for rotational speed equal to 75% or above.

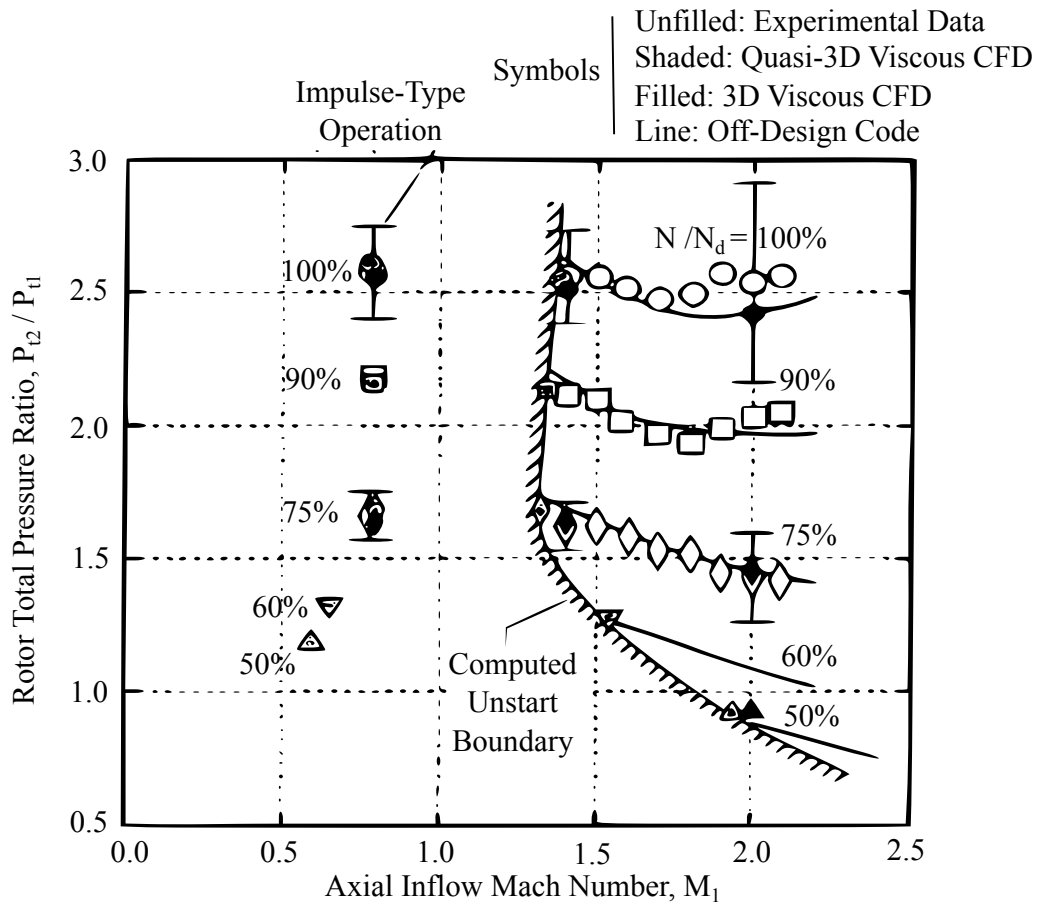


Figure 2.23: Supersonic Rotor Performance Map [7, pp.180]

- During supersonic through-flow operating mode, the rotor performance is almost constant for a wide operating range. That is coherent with the work done on the flow during impulse-type condition, where an almost constant total temperature was present across the operating range thanks to a small blade exit angle.

The experimental design point conditions are a rotational speed of 17,188.70 rpm, an axial inflow Mach number equal to 2.0 and a corresponding total pressure ratio of around 2.5. The presence of measurement uncertainty, caused by complex shock pattern which occurred around the experimental rakes, could justify the discrepancy between the original design total pressure ratio of 2.7 and the experimental one.

The next chapter introduces the reader to the used methodology including the criteria behind the blade modelling, the domain choice, details about the CFD analysis and the principles behind the optimisation process.

Chapter 3

Methodology

The used methodology is described in this chapter. A general methodology scheme is firstly presented, showing all the carried out steps necessary to obtain the final results. Each step is then analysed in the subsequent sections, justifying where possible why some choices have been made over others. This includes the domain choice, the blade modelling, details about the CFD analysis such as boundary conditions, mesh design and turbulence models choice and the criteria behind the validation process. Finally, the criteria and the algorithms used for the optimisation process are described.

3.1 Methodology Scheme

All the software tools that will be cited from now on are part of the commercial package ANSYS[®]. All the software settings are reported in Appendix [B](#). The scheme of the used methodology is shown in [Figure 3.1](#). The steps can be summarised as follows:

- Both the rotor blade tested by NASA and the related fluid domain are replicated by using BladeGen.
- The model is then validated by comparing CFD results with the experimental ones. CFX and of TurboGrid are used respectively for CFD simulations and grid generation.

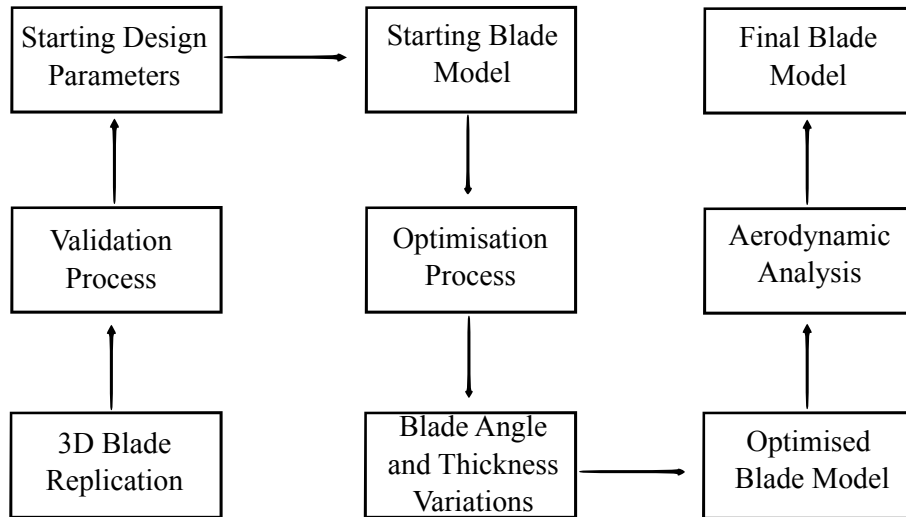


Figure 3.1: Methodology Scheme

- Once the model is validated, its geometrical parameters such as blade angle and thickness distributions are used to carry out an optimisation process focused on maximising efficiency and total pressure ratio. The optimisation loop is set via the use of DesignXplorer.
- The result of the optimisation process will be a new blade model in which the aerodynamic features are then analysed via the use of CFD. If necessary, geometry adjustments will be carried out obtaining a final and optimised blade model.

3.2 Domain Definition

The domain to be used during the CFD analysis should reflect as much as possible the geometry used during the rotor testing. Its dimensions should be determined in such a way to make possible the evaluation of the performance quantities in the same stations as the experimental ones. It has to be considered that the mesh will be created based on the domain design, with the cells aligned to its sidewalls¹. "The alignment of grid lines with the absolute flow streamlines has a beneficial effect in helping to reduce numerical diffusion" [24, pp.42]. Since the inlet flow is axial, a straight domain is preferable, at least

¹True only if a structured mesh is used.

for the section upstream of the blade. For the sake of simplicity, the replicated domain is fully straight, except for the blade position, and does not take into account the variable geometry feature of the test facility which can instead be replicated by setting proper boundary conditions. Therefore, the domain length has been set equal to the length of the straight section in the shortest configuration of the test package², already presented in the dedicated section (Table 2.2). A domain of such length includes the location of the experimental rakes. Details about the domain design settings can be found in Appendix B.1.

3.3 Original Blade Modelling

The blade modelling process involved the analysis of several different blade designs due to the lack of manufacturing data. The blade geometry was adjusted until the CFD validation process was satisfactory, which indirectly means that a proper blade geometry was produced. The blade was modelled by using BladeGen. BladeGen has two distinct modes of operation, the angle/thickness mode and the pressure side/suction side mode. In this project, the angle/thickness mode was used. A general scheme of how BladeGen works in such a mode is presented in Figure 3.2. The model represents the blade system in three dimensions and contains data about the meridional profile and the blade. The meridional profile is used for creating the fluid domain and is determined by a set of curves defined at the hub, shroud, inlet, and outlet. This data is integrated with the leading and trailing edge curves and with a list of layers, as shown in Figure 3.3. Each layer represents a streamline and is defined as a meridional curve that represents a surface of revolution. By default, the total number of layers is equal to five. Each blade consists of an angle and thickness definition made up of curves that the user can modify in the respective view. A single curve references to a single layer. By default, the adjustable layers are three, namely at 0%, 50% and 100% of the blade span. The default settings were maintained and the full

²The shortest configuration has been chosen in order to reduce the number of cells of the final mesh and so the computational cost of the simulations.

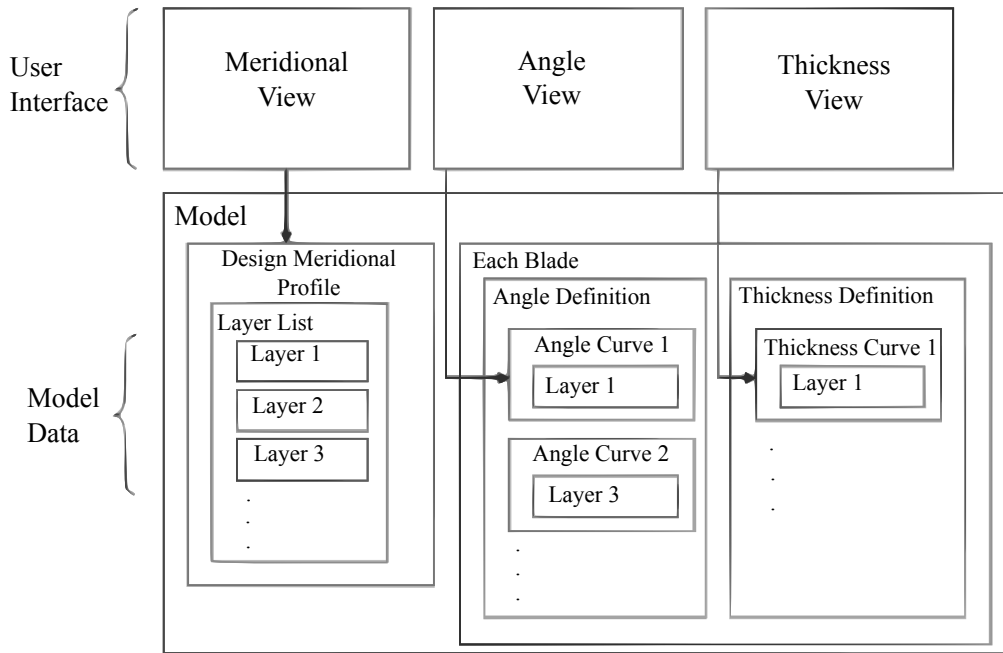


Figure 3.2: BladeGen Working Scheme [25, pp.64]

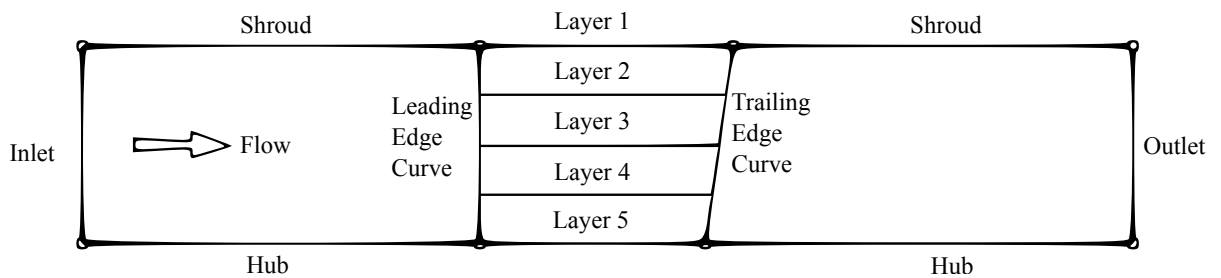


Figure 3.3: Meridional Profile

blade model was then obtained via the interpolation of the distributions at such stations.

All curves used in BladeGen are generated from a user-defined number of points and so are made by one or more segments. A list of the available curve segment types is reported below.

- **Piecewise Linear Segment:** The points that make up this segment type are joined by straight lines. Usually used to define the meridional profile. Not recommended for other applications.
- **Cubic Spline Segment:** These curves use an interpolation formula that is continuous through the second derivative at the junctions between piecewise curves. This

results in a smooth curve that passes through all of the points.

- **Bezier Segment:** This type of curve is defined by control points constituted by the endpoints and the intermediate points. The curve passes through the endpoints but it does not necessarily pass through the intermediate points. Bezier curves are recommended for the design of a blade in the angle/thickness views because of their smoothness and of their resistance to local curve distortions.
- **Best Fit Polynomial Segment:** This segment type is defined by a polynomial curve, the coefficients of which are determined from the least squares fit to the data points in the segment. This type of curve is used where some smoothing is required.
- **Arc Segment:** This segment consists of a 3-point circular arc and can be used only for the meridional profile design.

The blade angle and thickness distributions were discretised with a variable number of points and by using cubic splines or Beizer segments due to the smoothness of such curves. In order to allow the repeatability of the analysis, both the general software settings and the locations of the blade angle and thickness distribution discretisation points are presented in Appendix [B.2](#). The final blade integrated with the domain is shown in [Figure 3.4](#). The blade hub, mid and tip section are reported from [Figure 3.5](#) to [Figure 3.7](#).

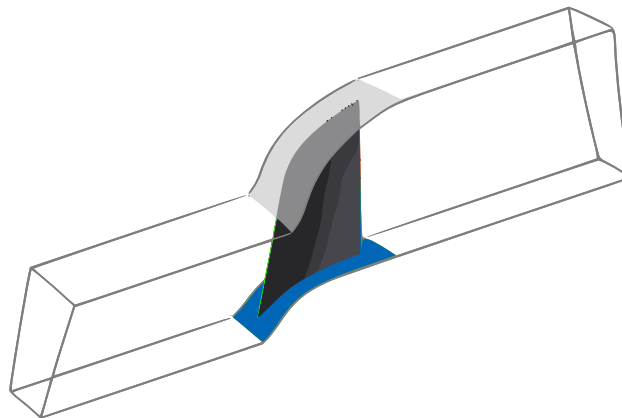


Figure 3.4: Original Blade Model and Domain Representation

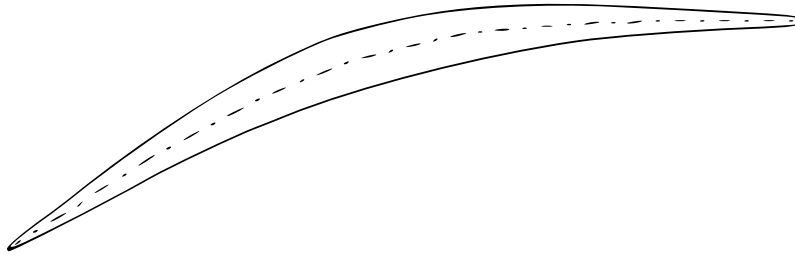


Figure 3.5: Original Blade Hub Section

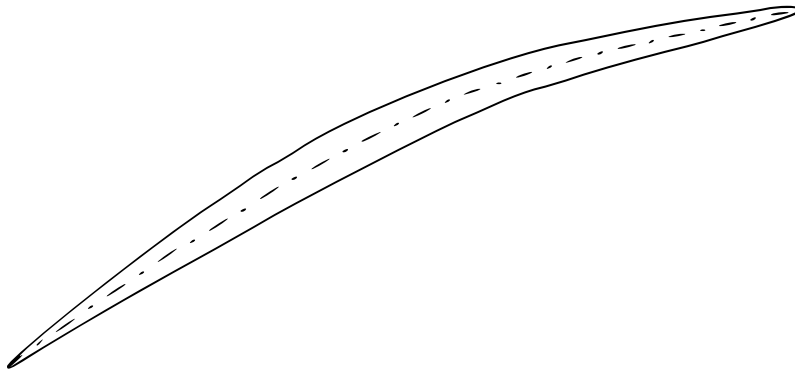


Figure 3.6: Original Blade Mid Section

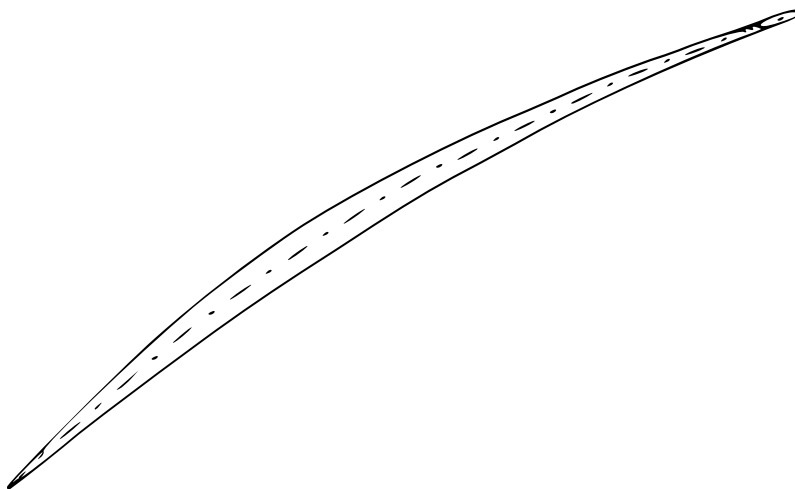


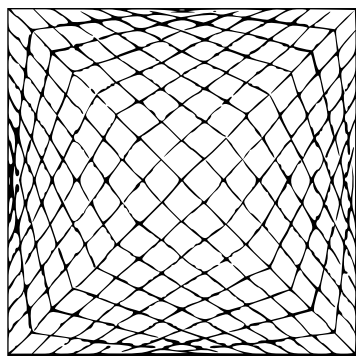
Figure 3.7: Original Blade Tip Section

3.4 Mesh Design

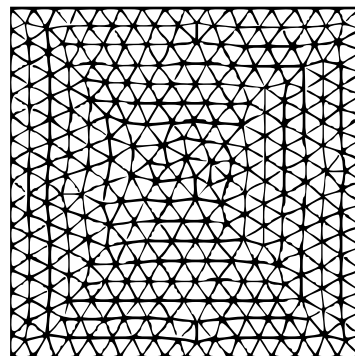
”The user must think about model and solver settings before generating the grid” [26, pp.5]. First of all, the kind of mesh to be used has to be determined. A structured mesh is defined as a mesh with regular connectivity, while an unstructured mesh is defined as a mesh with irregular connectivity. The differences between such meshes are shown in Figure 3.8. Generally, a structured mesh is used for turbomachinery simulations since such mesh is less costly concerning computational power and more tolerant to mesh defects such as skew and high expansion rates. Moreover, geometry adaption capabilities typical of unstructured meshes are not needed for blade profiles, unless sharp edges are present. Based on the considerations made, a structured mesh has been selected.

One of the objectives of the CFD analysis is to capture all the fluid flow characteristics, including boundary layer transition effects and wake turbulence modelling. In order to do so, the recommended mesh guidelines are a max $y^+ \leq 1$, a wall normal expansion ratio ≤ 1.1 and about 70 mesh nodes in the blade streamwise direction [27]. Moreover, a proper mesh should have a minimum number of nodes inside the boundary layer. As a general rule, a boundary layer ought to be settled with no less than ten nodes [28]. The y^+ is the adimensional wall distance defined as follows:

$$y^+ = \frac{\Delta y}{\nu} \sqrt{\frac{\tau_w}{\rho}} = \Delta y \sqrt{\left(\frac{\partial u}{\partial y}\right)_{=0} \sqrt{\frac{\rho}{\mu}}} \quad (3.1)$$



Structured Mesh



Unstructured Mesh

Figure 3.8: Structured and Unstructured Mesh [24, pp.26]

In order to create a valid mesh, the first element offset Δy has to be computed for a specific desired y^+ value. The velocity gradient can be related to the local Reynolds number in the following way:

$$\left(\frac{\partial u}{\partial y}\right) \approx \left(\frac{\partial u}{\partial x}\right) \sqrt{Re_x} \quad (3.2)$$

The local Reynolds number is also proportional to the free stream flow speed U_∞ , as shown below:

$$Re_x = \frac{\rho U_\infty x}{\mu} \quad (3.3)$$

In other words, it is possible to compute the first element offset by knowing the fluid flow characteristics which change depending on the set boundary conditions and the turbulence model used. Ideal air has been considered for the calculations. A first element wall distance suitable for keeping a $y^+ < 1$ for all the cases has been determined, and it is reported, with all the meshing settings, in Appendix [B.3](#). In the settings tables, only the final mesh is presented. Such mesh is the result of a mesh dependency study and a mesh quality assessment. As an example, the y^+ value at mid-span for the design point simulation using the $k - \omega$ turbulence model is reported in Figure [3.9](#).

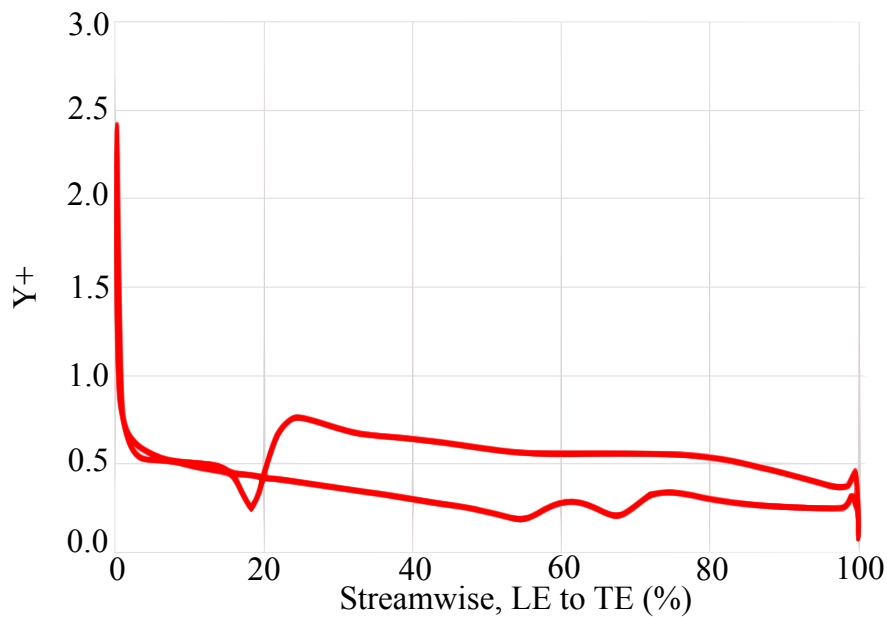


Figure 3.9: Mid-Span Y^+ at Design Point Conditions

3.4.1 Mesh Dependency Study

The results between a fine and a coarse mesh differ due to the different resolution of the flow occurring phenomena, such as shockwaves or expansion waves. A finer mesh usually provides better results but also requires a higher computational cost. A mesh dependency study aims to do a trade-off between results grid independency and computational cost. The $k - \omega$ turbulence model has been selected to carry out the study due to its relatively low computational cost and due to its capability of resolving the near-wall characteristics via an automatic wall function. The investigated parameter was the rotor isentropic efficiency and the boundary conditions were set in order to replicate the design point conditions. Such condition is characterised by complex shock patterns and is therefore considered suitable for a grid dependency study in terms of isentropic efficiency. The meshes quality was checked before running the study in order to ensure that it was not affected by factors not related to the grid refinement. The results are reported in both Table 3.1 and Figure 3.10³.

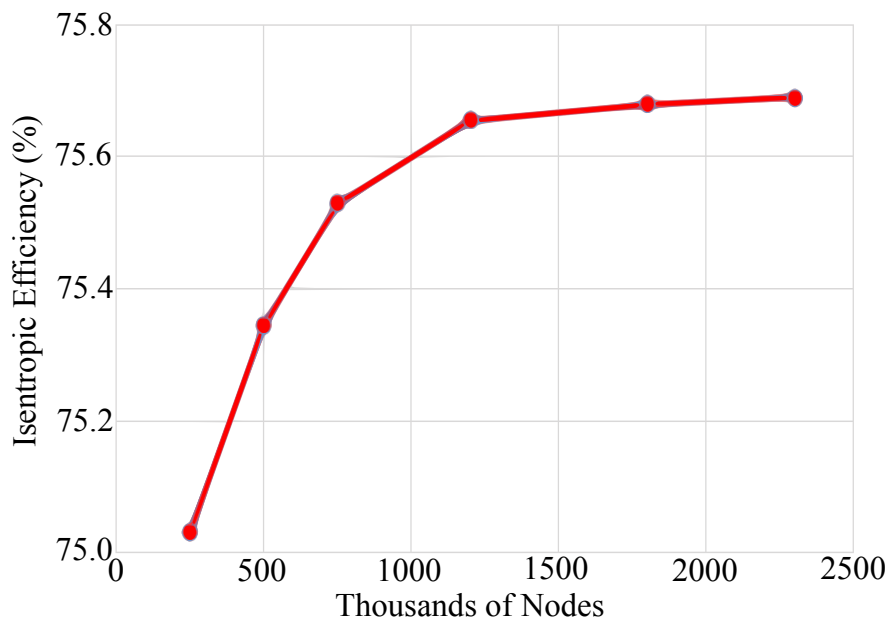


Figure 3.10: Isentropic Efficiency Grid Dependency

³The efficiency is the one calculated automatically by CFD Post which considers the total pressure and total temperature ratios at the domain inlet and outlet. The value of such efficiency is different from the experimental one but is still a valid parameter to be monitored for a mesh dependency study.

Table 3.1: Isentropic Efficiency Grid Dependency

Mesh Number	Number of Nodes	Isentropic Efficiency (%)	$\Delta\eta_R$ (%)
1	250,000	75.032	-
2	500,000	75.345	0.415
3	750,000	75.530	0.245
4	1,200,000	75.656	0.165
5	1,800,000	75.680	0.032
6	2,300,000	75.690	0.013

Based on the study results and the available computational power, the mesh number 3 has been selected for the CFD simulations. Usually, a good 3D mesh of a blade section should be composed by at least 400,000 nodes [29]. Probably due to the complex supersonic flow features and due to the complex shockwave patterns, a mesh of around 750,000 nodes resulted more suitable in this case.

3.4.2 Grid Quality Assessment

The mesh quality study is done by checking specific parameters reflecting the cell geometry characteristics. A general guideline can be found in the ANSYS[®] Turbogrid User's Guide [30], here only a summary is reported. The parameters to be checked are listed below in order of importance:

1. **Minimum Volume:** Evaluates the minimum element volume in order to avoid the presence of negative volume elements. For such reason, this parameter has to be greater than zero.
2. **Minimum/Maximum Face Angle:** Evaluates the minimum/maximum angle between the two edges of the faces that touch a node. That can be considered a measure of cell skewness, which represents how close to the ideal equiangular element the cell is. A minimum face angle not below 15° and a maximum face angle not over 165° are recommended.

3. **Edge Length Ratio:** For a single cell, it is defined as the ratio between the longest edge of a face and the shortest one. Can be considered as a measure of the cell aspect ratio. For double precision problems, this parameter should be less than 1,000.
4. **Element Volume Ratio:** It is the ratio between the maximum volume and the minimum one of the cells which touch a node. Can be considered as a measure of the local expansion factor. Such parameter should be less than 20.
5. **Connectivity Number:** Represents the maximum number of cells that touch a node. This parameter is important only for unstructured meshes where the geometry of the cell can vary.

The quality parameters for the final selected mesh are reported in Table 3.2. The mesh showed excellent quality and was therefore selected for the CFD simulations. The final mesh is presented in Figure 3.11.

Table 3.2: Mesh Quality Parameters

Mesh Measure	Value	Bad Elements(%)
Minimum Volume	$2.36 e^{-13} \text{ [m}^3\text{]}$	0.0
Minimum Face Angle	59.57 [deg.]	0.0
Maximum Face Angle	115.02 [deg.]	0.0
Maximum Edge Length Ratio	817.18	0.0
Maximum Element Volume Ratio	3.11	0.0
Connectivity Number	10	0.0

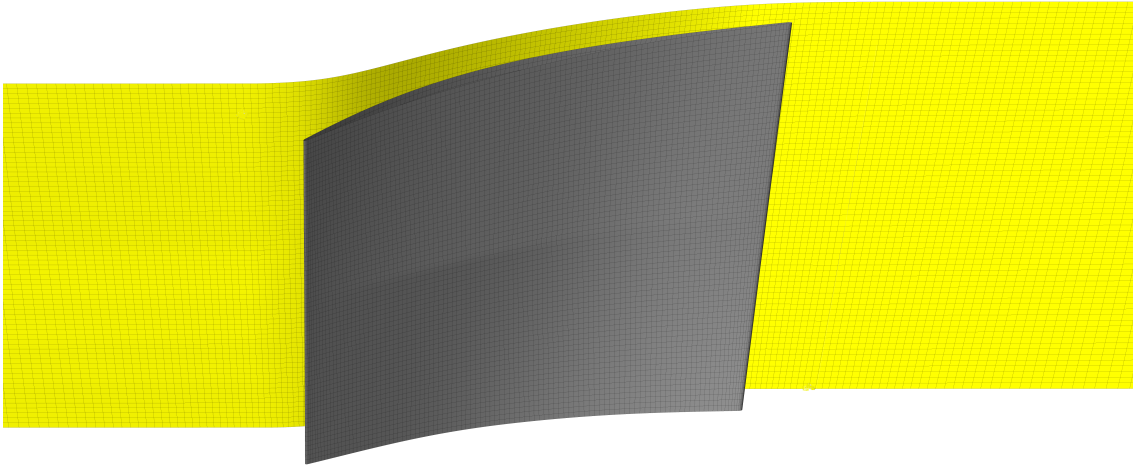


Figure 3.11: Final Mesh - Lateral View

3.5 Computational Fluid Dynamics

Both the validation and optimisation processes are based on computational fluid dynamics (CFD) simulations. The reliability of the results depends strongly on how the flow characteristics are modelled. One of the most important aspects to model is the flow turbulence. Turbulence occurs when the inertia forces in the fluid become significant compared to viscous forces. Turbulence capture would generally involve length scales much smaller than the smallest finite volume mesh requiring a too high computational cost.

In order to predict the effects of turbulence effectively, statistical turbulence models based on the Reynolds Averaged Navier-Stokes (RANS) equations have been developed. Depending on the nature of the simulation, some of them are more reliable than others. Usually, a turbulence model sensitivity study is done to find out which is the best turbulence model to use for a specific application. The turbulence sensitivity study is here done in concurrence with the validation process. The results are shown in the dedicated section [4.1](#).

A full theoretical description of the available turbulence models is reported in ANSYS[®] CFX-Pre User's Guide [\[31\]](#). Here only a brief and qualitative description is presented in order to justify why certain turbulence models have been selected for the turbulence sensitivity study over others.

The available turbulence models and the respective descriptions are listed below:

- **$k - \varepsilon$** : It is a two-equation model accounting for the flow kinetic energy k and for the dissipation rate ε of the turbulence kinetic energy into internal thermal energy. Due to its stability, accuracy and numerical robustness, it is considered the industry standard model. It assumes the flow fully turbulent and therefore is not able to capture transition points. The standard version is a good one for capturing the general behaviour of the flow. There are applications for which this model may not be suitable such as flows with boundary layer separation or flows over curved surfaces. The Explicit Algebraic Reynolds Stress Model (EARSM) enables an extension of the standard $k - \varepsilon$ model in order to capture effects of secondary flows and flows over curved surfaces.
- **$k - \omega$** : Turbulence models using the ε equation predict the onset of separation too late and under-predict the amount of separation. That is, such models provide optimistic performance characteristic. The standard $k - \omega$ model can overcome such problem by expressing the dissipation rate via another equation, namely the ω equation. However, the main problem with such model is the strong sensitivity to freestream conditions. In order to avoid such problem, the Baseline (BSL) version of the model has been developed. It permits a blending between the $k - \omega$ model near the surface and the $k - \varepsilon$ model in the outer region. Even if the BSL version overcomes the freestream conditions dependency problem, it still fails in predicting flow separation from smooth surfaces. The Shear-Stress-Transport (SST) version was designed in order to predict such separation properly. An EARSM version of the BSL model exists in order to capture effects of secondary flows and flows over curved surfaces.
- **Reynolds Stress Models (RSM)**: Compared to the $k - \varepsilon$ model, the standard Reynolds Stress Model has six additional turbulence transport equations resulting in usually higher accuracy for complex flows but also in a reduced numerical robustness and a

higher computational cost. RSM based on the ε equation give an inaccurate prediction of flow separation as stated before. In order to avoid these issues, RSM based on the ω equation have been developed including also a Baseline version (BSL RSM) which is insensitive to freestream conditions.

Since the $k - \varepsilon$ model is not able to capture boundary layer separation and flows over curved surfaces properly, it has been considered not suitable for the analysis of a flow field as complex as the one in the supersonic through-flow rotor. Both $k - \omega$ and RSM models have been used, including the SST, BSL or EARSM extensions in order to account for secondary flows and independence from the freestream conditions. Therefore, the validation process has been carried out by using the following turbulence models: Standard $k - \omega$, SST $k - \omega$, BSL EARSM $k - \omega$ and BSL RSM.

3.5.1 Boundary Conditions

The domain has been divided into different parts as shown in Figure [3.12](#). To each part has then being assigned a proper boundary condition. All the details about the settings are reported in Appendix [B.4](#). As a general description, all the lateral interfaces of the domain have been set periodic, so that only one blade passage can be analysed rather than the full rotor. All the walls have been set as no-slip walls meaning that the fluid immediately next to the wall assumes the velocity of the wall itself which is zero by default. Subsonic conditions have been replicated by setting pressure and temperature equal to the plenum conditions (standard day conditions) at the inlet and by modifying case by case the average static pressure at the outlet. A higher back static pressure condition brings the rotor next to the surge line, while a lower back static pressure condition brings it to the choking line. Impulse-type conditions have been replicated by merely reducing the back static pressure to a level for which the rotor outflow resulted supersonic. Supersonic conditions have been replicated by setting a simply supersonic boundary condition at the outlet and by regulating static pressure, static temperature and flow normal speed at the inlet in order to replicate the experimental inlet Mach numbers. For all the cases, the turbulence

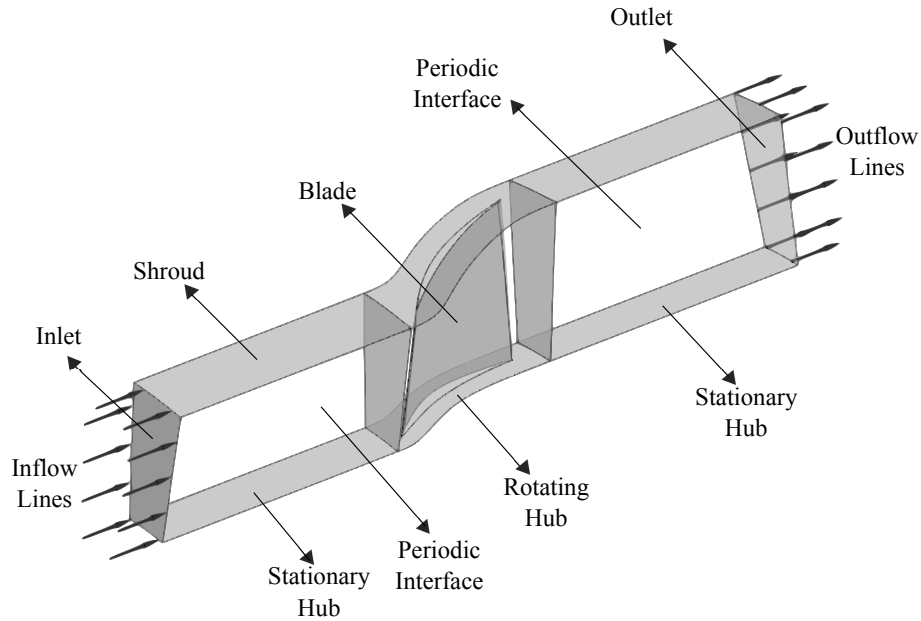


Figure 3.12: Domain Suddivision

intensity and the turbulence length scale should be set at the inlet. Such data usually come from the experimental results and are not available for the supersonic through-flow rotor. According to the manual guidelines, the default turbulence intensity value of 3.7% is a reasonable estimation in the absence of experimental data. The turbulence length scale is then automatically computed based on the domain dimensions.

3.5.2 Solver Settings

Solver settings details are reported in Appendix [B.4](#). High resolution has been set for the turbulence solving process. The used convergence criterion was an iterative one based on the monitoring of the residuals tolerances. The simulations have been considered converged when the residuals were below $1e^{-5}$. Since a low residual tolerance does not necessarily mean that the simulation has converged, the stability of the isentropic efficiency has also been checked. An outlet monitoring point has also been created in order to monitor the mass flow stability. For instance, the residuals along with the isentropic efficiency stability for the choking conditions at 50% of the rotational speed are showed in Figures [3.13](#) and [3.14](#).

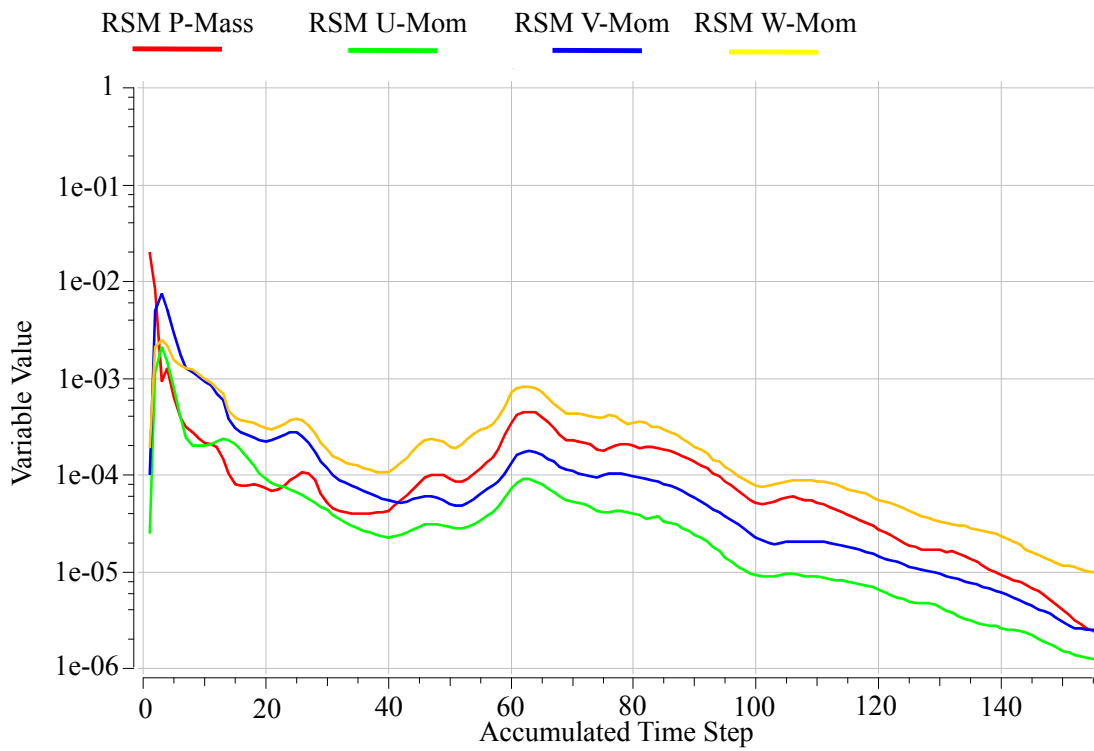


Figure 3.13: Residuals for choking conditions at 50% rotational speed

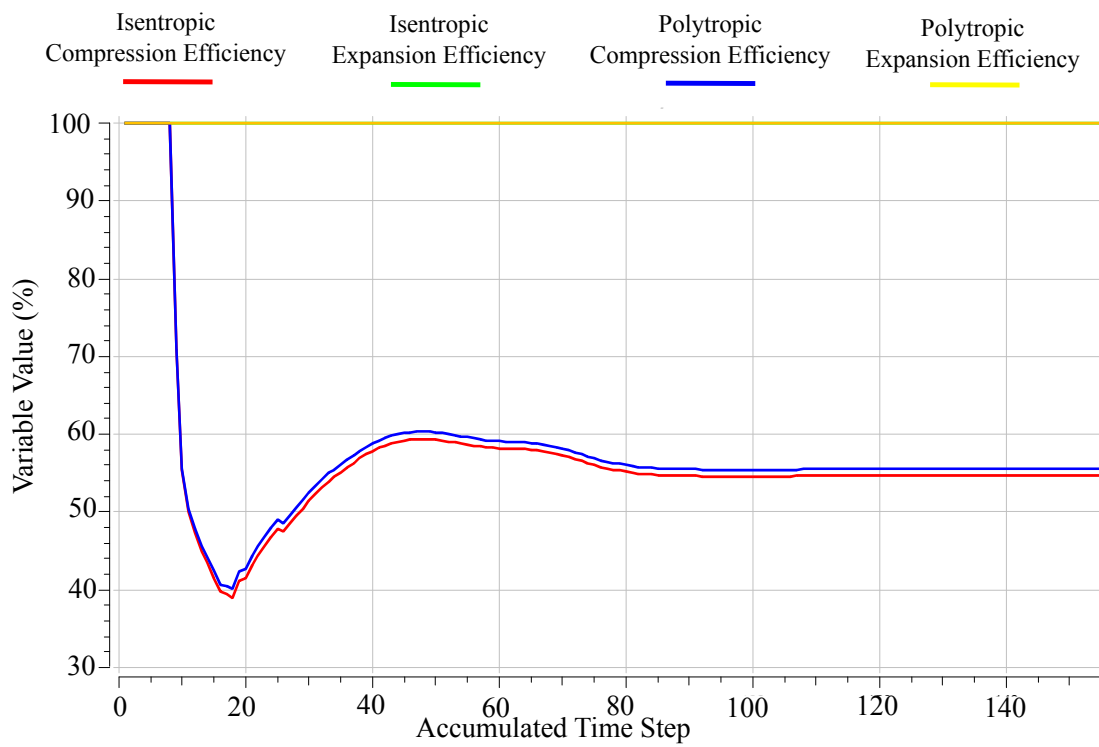


Figure 3.14: Efficiency Stability for choking conditions at 50% rotational speed

3.6 Optimisation Process

Part of the thesis aim is to investigate how blade angle and thickness variations can influence both the isentropic efficiency and total pressure ratio. The group of parameters that can be varied to improve the design are called design variables, while the studied outputs are called objective functions. In this case, the design variables are some of the blade angle and thickness distribution discretisation points, while the objective functions are isentropic efficiency and total pressure ratio.

As described in section 3.3, the blade has been designed by acting directly on three layers, namely hub, mean and tip. The original blade geometry presented in Appendix B.2 has been adapted in order to discretise the blade angle distribution of each layer with 5 points resulting therefore in a total of 15 points for the whole blade model. The thickness distribution discretisation points were not altered. All the 15 points representing the blade angle distribution plus 3 points corresponding to the maximum thickness of each layer were selected for the optimisation process, resulting in a total of 18 discretisation points. A summary of the location of such points is provided in Table 3.3. For the used nomenclature refer to Appendix B.5. In order to avoid a high problem complexity, only one degree of freedom was provided to each discretisation point, resulting in 18 design variables. The blade angle discretisation points were altered regarding value but not in terms of position along the blade chord (points movement possible only along the y-axis), while the thickness discretisation points were altered regarding position but not in terms of value (points movement possible only along the x-axis). By doing so, it is possible to modify the blade geometry together with the position of the blade passage throat. The allowable movement for each discretisation point was of $\pm 15\%$ from the starting value. The design variables can be denoted with the following vector.

$$\vec{x} = (x_1, x_2, \dots, x_{18})^T \quad (3.4)$$

Table 3.3: Adapted Blade Model Discretisation Points Location

Layer	Distribution	Curve Type	Discretisation Points	x	y
0% Span	Angle	Bezier	HA1	0.0	-31.8
			HA2	30.0	-37.7
			HA3	46.0	-9.7
			HA4	70.0	2.8
			HA5	100.0	0.0
50% Span	Angle	Bezier	MA1	0.0	-38.1
			MA2	3.3	-31.0
			MA3	52.0	-40.5
			MA4	53.5	-9.7
			MA5	100.0	-12.2
100% Span	Angle	Bezier	TA1	0.0	-42.0
			TA2	16.0	-44.4
			TA3	54.0	-23.9
			TA4	89.5	-20.3
			TA5	100.0	-19.3
0% Span	Thickness	Bezier	HT	57.2	11.04
50% Span			MT	37.2	10.36
100% Span			TT	43.0	9.3

The optimisation process aims to find the set of design variables that maximise the two cited objective functions. That is done by exploring the design space which can be described by response surfaces.

3.6.1 Response Surface Methodology

The main problem in carrying out the study via the direct application of CFD is the high computational cost required for a full point-by-point analysis. A possible solution is to use approximation methods which result in a much less computational cost. Such methods can be classified as local or global, depending on the range of application. Usually, local methods are based on the approximation via the Taylor series expansion, while global methods can have a different nature.

The global approximation technique called Response Surface Methodology (RSM) has been selected for this study. All the details about the response surface technique are reported in the work of Box and Draper [32]; here only a brief introduction is presented. RSM is defined as a collection of mathematical and statistical techniques for an empirical model building where the relation between design variables and a response (objective function) is studied. The outcome of the RSM is called response surface. Mathematically it can be defined as follows:

$$y = f(x_1, x_2, \dots, x_{18}) + \varepsilon \quad (3.5)$$

Where y is the response, ε is the noise error which occurs due to differences in numerical convergence and the surface defined by $f(x_1, x_2, \dots, x_{18})$ is the response surface.

The first step in RSM is to find a suitable approximation to the true relationship. The most common forms of approximation are first or second order polynomials integrated with the least-squares method. An approach which uses genetic algorithms and described in section 3.6.4 is here adopted. Hence, the resulting response surface is a combination of all the response surface types available in DesignXplorer, namely the second order polynomial, the Kriging, the non-parametric regression type, the neural network type and the sparse grid type. Each of these response surface types is more suitable for a particular problem over another. By using the genetic aggregation approach, the structure of the response surface is not assumed a priori but is given as part of the solution, thus leading

to the best approximation quality. A fundamental part for the generation of a response surface is the design of experiments (DoE). The choice of a certain DoE over another can have a large influence on the final accuracy of the response surface, as well as on its computational cost.

3.6.2 Design of Experiments

A detailed description of DoE application for response surfaces is presented in the book of Myers and Montgomery [33], here only a general summary is reported. DoE is a strategy which permits to select the points where the response should be evaluated by using certain criteria. Before presenting an overview of the available DoE algorithms, a series of definitions are needed. The possible settings of each design variable in the N-dimensional space are called levels. For example, if only the upper and lower limits of each design variables are defined means that a two-level design is being studied. There are two possible ways to construct an approximation model starting from DoE: full factorial design in which all the possible design variables combinations are considered, and fractional factorial design in which only a few significant combinations are considered in order to save computational cost. For instance, a full factorial design which involves three design variables each one defined on three levels (lower bond, upper bond and central value) results in a total of $3^3 = 27$ combinations, as shown in Figure 3.15.

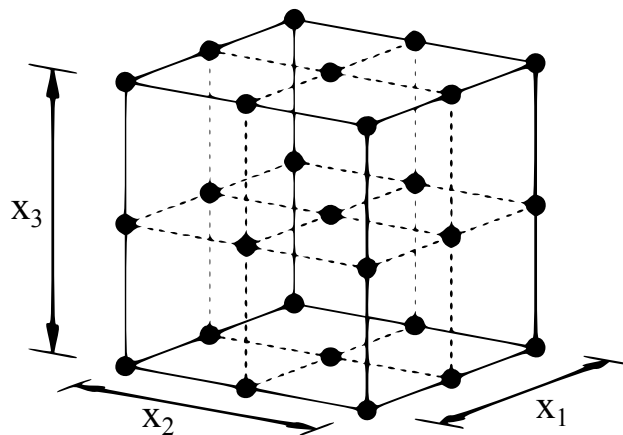


Figure 3.15: Full Factorial Design for Three Design Variables on Three Levels [35, pp.21]

In order to justify why an algorithm has been chosen over another, a general description of the ANSYS[®] available DoE algorithms is here reported. Full details can be found in ANSYS[®] DesignXplorer User's Guide [34].

- **Central Composite Design (CCD):** It is a three-level fractional factorial design which locates the points at the centre of each face formed by any two of the design variables. The method involves only corner factorial points. In this way, a lower amount of combinations are considered reducing the computational cost. For instance, a CCD which involves three design variables results in 15 combinations rather than 27, as shown in Figure 3.16. In case of a large number of design variables, the method could be still not feasible due to the high computational cost.
- **Box-Behnken Design:** It is a variant of the CCD in which the factorial points are located at midpoints of edges formed by any two design variables rather than at the corners. That results in a lower number of combinations considered also allowing to evaluate the design space in points which are far from extreme factor combinations.

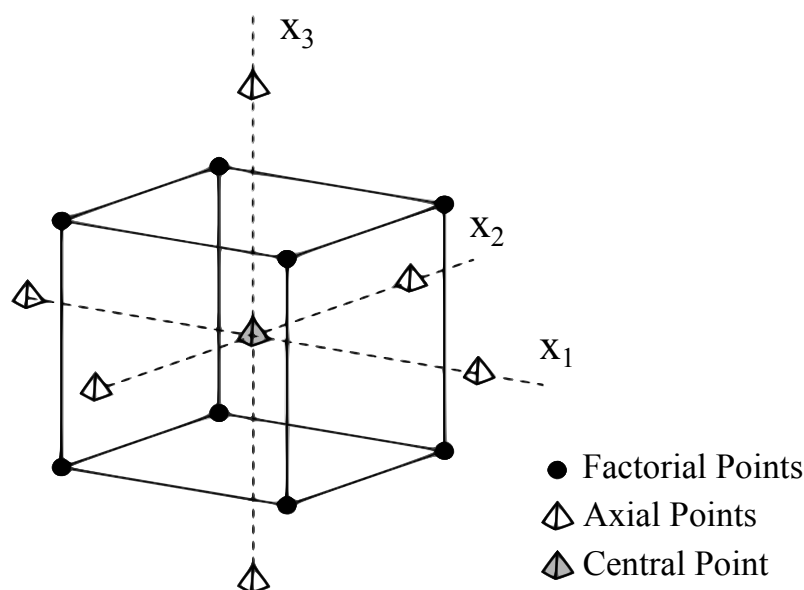


Figure 3.16: Central Composite Design (CCD) for Three Design Variables [35, pp.23]

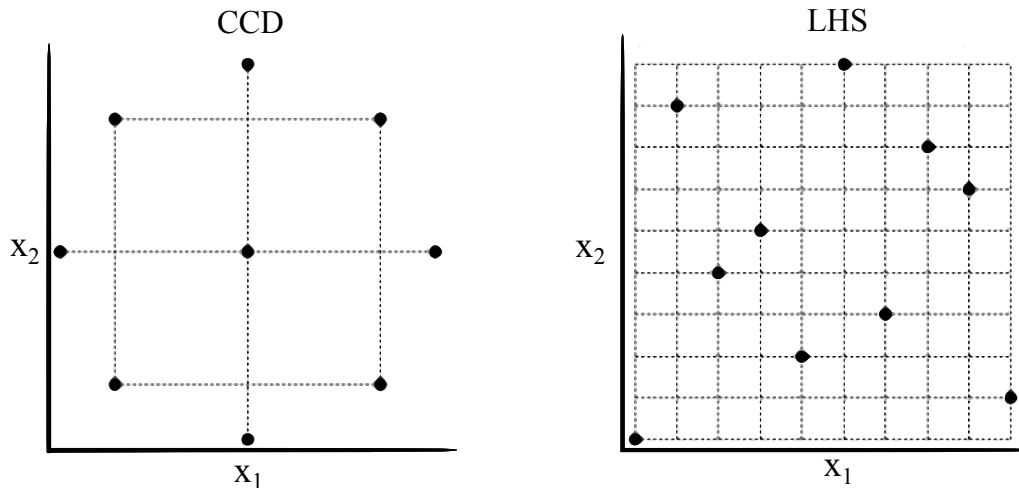


Figure 3.17: Comparison between LHS and CCD for Two Design Variables [35, pp.27]

- **Latin Hypercube Sampling (LHS):** It is a fractional factorial design which generates combinations randomly in the design space avoiding samples clustering. For instance, considering two design variables, no two points shares a row or a column of the grid. That results in a better-covered design space. A comparison with a CCD for two design variables is presented in Figure 3.17.
- **Optimal Space-Filling Design (OSF):** It is an LHS method extended with a post-processing part in which the combinations are not chosen randomly but are determined in order to maximise the distance between any two points. That results in a more uniform design space coverage but a higher computational cost if compared with LHS.

Among the available algorithms, LHS was chosen since it is the best compromise between design space filling and computational cost. Full quadratic model samples were used as samples type.

3.6.3 Response Surface Quality Assessment

Response surfaces are built from a series of design points in order to provide the approximated values of the objective functions quickly and without having to perform a complete CFD solution. In order to guarantee the success of the optimisation process, the reliability

of the response surface has to be high. If the quality of the prediction is not good enough, the associated risk is to end up with a surface in which the approximations are very far from the real output values, resulting therefore in a blade with real performances far from the expected ones. The accuracy of a response surface depends on the complexity of the solution, on the number of points used for building the surface and on the response surface type. Since the response surface type is determined by the genetic algorithm, the only way to guarantee a certain level of quality is to check the response surface goodness of fit.

For all response surface types, the goodness of fit is computed by comparing the learning and the verification points with the response surface predictions. The learning points are defined as the points used to build the response surface (DoE and eventual refinement points), while the verification points are defined as points in which real CFD simulations are performed. In other words, the evaluations of learning points give an idea about the quality of the interpolation, while the evaluations of verification points give an idea about the quality of the prediction. By default, the verification points are placed in locations that are as far as possible from the learning points ones.

For each output, the goodness of fit is shown in a table which includes the following criteria:

- **Coefficient of Determination:** It is defined as the ratio between the variation of the output parameter predicted by the response surface and the real total variation computed from the learning points. Its values are between zero and one where one indicates that all the output variation is explained by the response surface and is, therefore, the best possible value. Mathematically expressed as:

$$R^2 = 1 - \frac{\sum_{i=1}^N (y_i - y_i^*)^2}{\sum_{i=1}^N (y_i - y_i')^2} \quad (3.6)$$

- **Root Mean Square Error:** It is defined as the square root of an arithmetic mean of the squares of the residuals evaluated at the learning or verification points. The best value is equal to zero. Mathematically expressed as:

$$RSME = \sqrt{\frac{1}{N} \sum_{i=1}^N \left(\frac{y_i - y_i^*}{y_i} \right)^2} \quad (3.7)$$

- **Relative Average Absolute Error:** It is defined as the average of the residuals relative to the standard deviation of the actual outputs. The relative error for an output parameter is the error between the predicted and the observed output values, normalised by the known maximum variation of the output parameter. The best value is equal to zero. Mathematically expressed as:

$$RAAE = \frac{1}{\sigma_y} \frac{1}{N} \sum_{i=1}^N |y_i - y_i^*| \quad (3.8)$$

3.6.4 Genetic Algorithms

Holland [36] fully describes the genetic algorithm method, here it is briefly described focusing on its application for this case. Genetic algorithm (GA) is an evolutionary algorithm (EA) based on computer implementations of some of the evolutionary mechanisms found in nature. GA generates and maintains a certain number of individuals by implementing natural processes such as selection, reproduction (crossover) and mutation. The initial population is randomly chosen in the design space. Each individual then receives a measure of its fitness which is a measure of how desirable the individual is if compared with the other ones. In the case of the response surface generation, the fitness is associated with the surface accuracy and stability, while in the case of the response surface evaluations the fitness is related to the individuals' isentropic efficiency and total pressure ratio. Individuals with a fitness value below a certain threshold are discarded. The initial individuals' number is then maintained by producing new child individuals from the previously filtered parent ones by using crossover and mutation (Figure 3.18). Crossover is

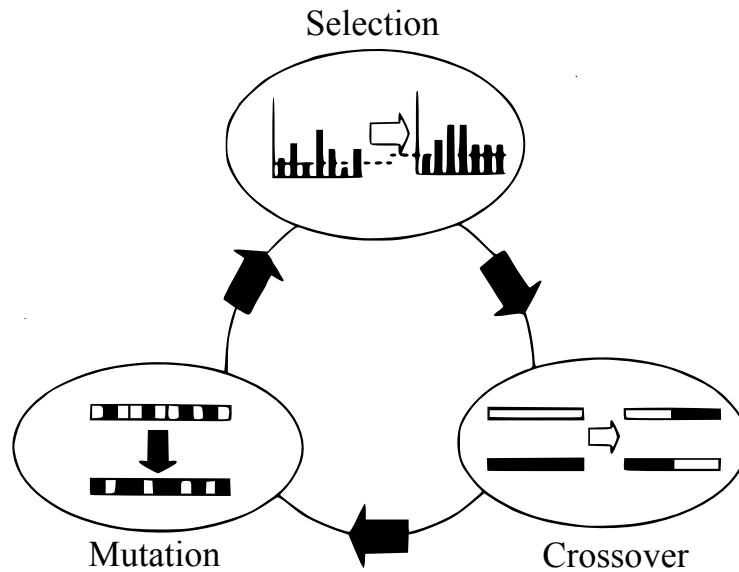


Figure 3.18: Genetic Algorithm Process [37, pp.110]

the process that mates two chromosomes (parents) to produce a new chromosome (child). The idea behind crossover is that the new chromosome may be better than both of the parents if it takes the best characteristics from each of them. Mutation is the process that alters one or more gene values in a chromosome. This can result in entirely new gene values being added to the gene pool. With these new gene values, the genetic algorithm may be able to reach a better solution avoiding also to stuck on local optima.

As anticipated in section 3.6.1, GA has been selected as the method for building the response surface since it results in the best response surface combination for a particular objective function, without assuming a priori the structure of the approximation. During the response surface generation, the crossover can occur between the same types of response surface or between two different types of response surfaces. In the first case, a part of the settings from the first parent is exchanged with the second one. In the second case, a new response surface which is a combination of the two parents is created. The mutation acts on one or several response surface settings of the parent surfaces.

DesignXplorer provides two possible algorithms for a multi-objective optimisation based on response surface evaluations, namely the Screening method and the MOGA (Multi-Objective Genetic Algorithm). Due to its quasi-random sampling method, the

Screening approach is mostly used for preliminary design evaluations. Hence, the MOGA method is here preferred. MOGA follows the steps already presented in Figure 3.18. The steps are repeated until convergence which occurs when the difference between the mean and the standard deviation of a population with regards to the previous one is below a set value. In the case of continuous numerical design variables, the parents are composed by a certain number of floating genes. The crossover between two parents brings to two new individuals that can be defined by the following equation:

$$Child1 = a * Parent1 + (1 - a) * Parent2 \quad (3.9)$$

$$Child2 = (1 - a) * Parent1 + a * Parent2 \quad (3.10)$$

Where a is a random coefficient. For instance, considering parents consisting of four floating genes and a coefficient $a = 0.7$ the result of the crossover is the following:

$$Parent1 = (0.3)(1.4)(0.2)(7.4)$$

$$Parent2 = (0.5)(4.5)(0.1)(5.6)$$

$$Child1 = (0.36)(2.33)(0.17)(6.86)$$

$$Child2 = (0.402)(2.981)(0.149)(6.842)$$

For continuous parameters, mutation is instead implemented via a polynomial mutator. It can be defined as:

$$Child = Parent + (UpperBound - LowerBound)\delta \quad (3.11)$$

Where δ is a small variation computed from a polynomial distribution, while the upper and lower bound are constraints set by the user.

GA was selected also for response surface evaluations over other methods due to its balance between exploration and exploitation. Exploration is defined as the ability to investigate new areas of the design space, while exploitation is defined as the ability to make

use of the knowledge gained in order to reach better positions in the design space. Exploration is guaranteed by working with a population rather than a single point reducing the risk of capturing local minima, while exploitation is guaranteed by using a probabilistic search method rather than a deterministic one.

3.7 Summary

The fluid domain was created in order to make possible the evaluations of total pressure and total temperature at the corresponding experimental rakes locations so that a direct comparison with the experimental data was possible. The blade was designed by setting the blade angle and thickness distributions at three layers, namely at 0%, 50% and 100% of the blade span. The full model was obtained via the interpolation of the distributions at such stations. The grid quality was checked and a mesh dependency study was carried out in order to ensure that the results were not affected by elements not related to the flow characteristics. Due to the nature of the CFD problem, Standard $k - \omega$, SST $k - \omega$, BSL EARSM $k - \omega$ and BSL RSM were chosen as turbulence models to investigate. The optimisation method used a combination of response surface evaluations and genetic algorithms. LHS with full quadratic model samples is the algorithm used for the DoE, while genetic aggregation and MOGA are the algorithms used respectively for the response surface generation and the response surface evaluations.

The next chapter introduces the reader to the final results including both the validation and the optimisation ones.

Chapter 4

Results and Discussions

The final results are shown in this chapter. The validation process of the original blade model is firstly described, including the performance aspects during all the possible rotor operating modes and justifying where possible the rotor behaviour. Subsequently, details about the optimisation process and about the generated response surface are shown. The optimised blade geometry is then reported and its performance is then compared with the original model one for all the possible operating modes.

4.1 Validation Process

Before proceeding with the optimisation process, the blade model has to be validated. As stated many times, such validation is done by comparing experimental results with CFD ones, particularly by using Standard $k - \omega$, SST $k - \omega$, BSL EARSM $k - \omega$ and BSL RSM as turbulence models as explained in the dedicated methodology section [3.5](#). Different blade models have been created due to the lack of manufacturing data. All the results here presented are only about the final blade model and include also a comparison between the cited turbulence models. That is done in order to understand which is the most suitable model for the supersonic through-flow rotor case. Since it is not possible to carry out the optimisation process with multiple turbulence models due to the high computational cost that this would imply, the identification of the most suitable model

is a crucial part. That is, only one between the cited models will then be used during the optimisation process. The results of the validation process can be categorised into two separate parts: the subsonic operating mode one and the supersonic through-flow operating mode coupled with the impulse-type one. In fact, it has already been evidenced that the supersonic through-flow mode can be considered as a particular impulse-type mode with supersonic axial inflow.

4.1.1 Subsonic Through-Flow Operating Mode

The experimental rotor subsonic total pressure and isentropic efficiency maps are here presented along with the CFD results (Figures 4.1 and 4.2). Regarding the computed results, the total pressure ratio is computed by measuring the total pressure at both the domain inlet and the one at a location 6.414 inches downstream of the blade leading edge, the absolute Mach number is evaluated at 2.0 inches upstream of the blade leading edge and finally the isentropic efficiency is computed by using the cited total pressure locations and by evaluating the total temperature at both the domain inlet and at a location 7.613 inches downstream of the blade leading edge. Such locations are coherent with the position of both the experimental rakes and the test package plenum.

In both the performance and the efficiency maps, a maximum rotational speed of 75% is reported. This is the case since the experimental supersonic inflow was started at such rotational speed due to the low discontinuity in the blade loading between the subsonic and the supersonic operating mode. Experimental data of the rotor operating in subsonic mode at 100% of the rotational speed are not available, but it is possible to show the characteristics of such flow via the use of CFD. It is visible from the performance maps how there is little or almost no difference between the turbulence models predictions. The different points positions are a direct consequence of the different boundary conditions set, but no model seems to fit better the experimental results over the others. The efficiency is not predicted in such a well way as occurs with the total pressure ratio. A very well fitted performance map associated with a bit of discrepancy in the efficiency one is not an

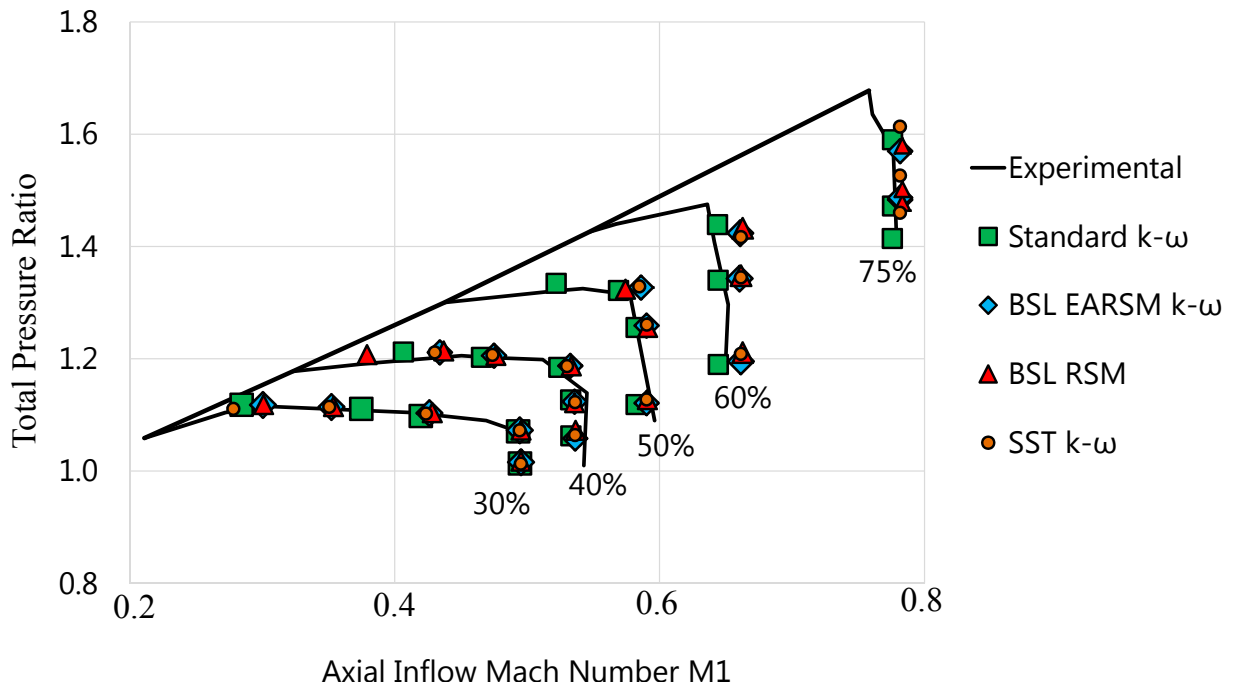


Figure 4.1: Subsonic Performance Map

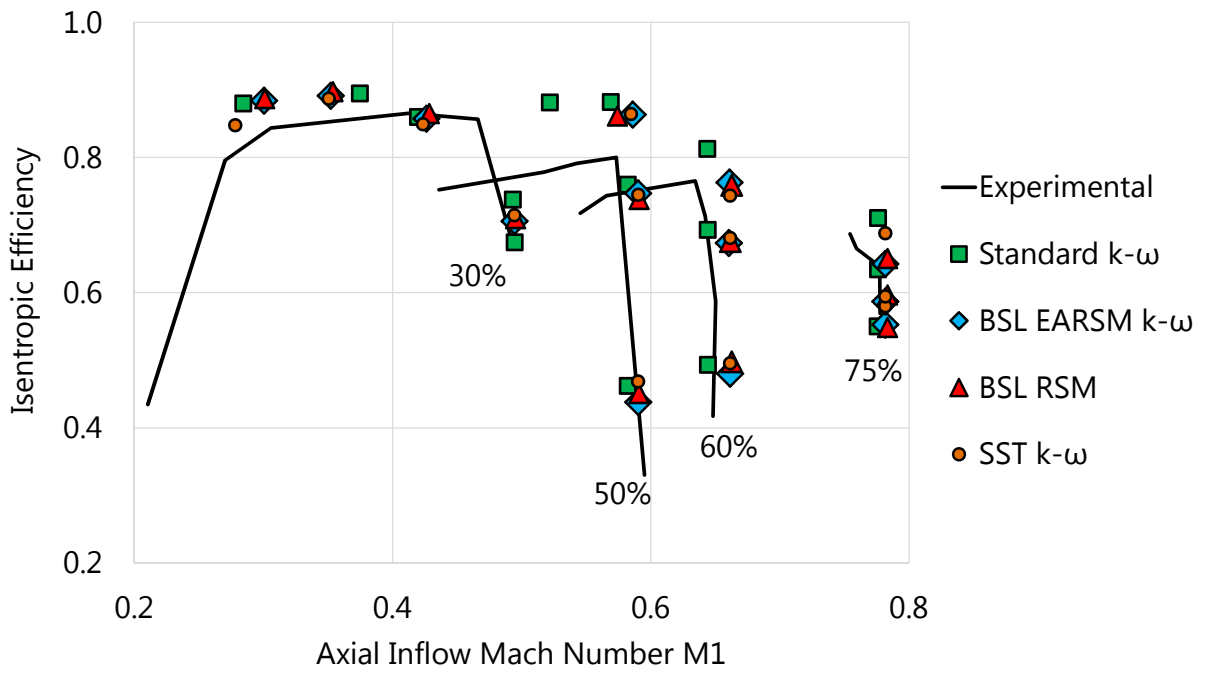


Figure 4.2: Subsonic Isentropic Efficiency Map

unexpected situation since the efficiency is a more difficult parameter to predict correctly by the use of CFD. Moreover, points next to the surge line were difficult to predict resulting therefore in a higher computed efficiency in such conditions.

It is possible to extend the validation process from the replication of the performance maps to the general flow characteristics analysis, confirming if possible the theoretical aspects. All the flow contours and characteristics that will now be showed are the results of the standard $k - \omega$ turbulence model. The blade mid-span Mach number contours at choking condition and 50% of the rotational speed are shown in Figures 4.3 and 4.4, respectively in the absolute and relative frame of reference. The thick blue line represents the location in which a unitary Mach number is present. Both the absolute axial inflow and outflow are subsonic. In both the frame of reference, it is possible to notice how the flow inside the blade passage becomes supersonic. That is possible thanks to the particular convergent-divergent blade passage geometry with the minimum section located at around mid-chord. In order to obtain a subsonic outflow, a strong shock is present inside the passage just after the minimum area section. Such shock not only brings the flow back to subsonic conditions but also induces a high flow separation causing a considerable reduction in isentropic efficiency as can be seen in the corresponding map. The position of the shock depends on the back static pressure set, particularly the lower it is the further downstream the shock will be. Moreover, a further downstream shock implies a faster flow impinging on it resulting therefore in a stronger shock and so a lower rotor isentropic efficiency. This efficiency downtrend ends when the passage shock is located outside of the blade passage, or in other words when the impulse-type conditions are established.

The choking condition at 50% of rotational speed does not correspond to the establishment of the unique-incidence condition, but is the condition at which, for a fixed rotational speed, the maximum inlet mass flow is reached. The unique-incidence condition occurs only if the relative inflow is supersonic, characteristic not present in this case. That is confirmed by the presence of the choking plane located in both the frame of reference just upstream of the blade minimum passage rather than between the blade leading edges. In

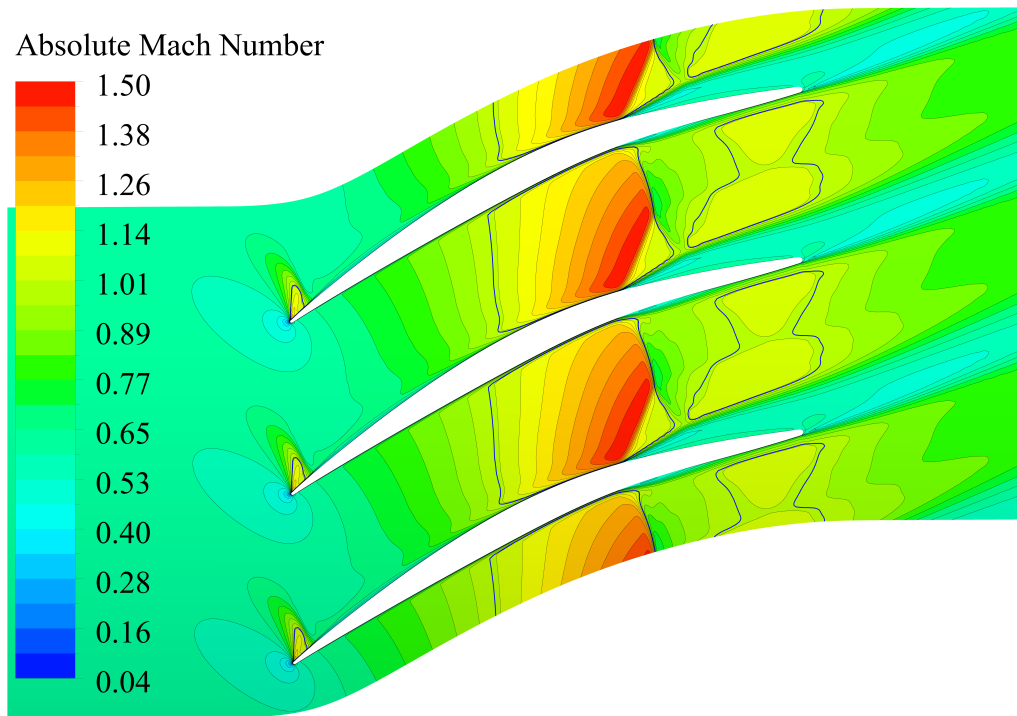


Figure 4.3: Mid-Span Absolute Mach Number Contours at Choking Conditions and 50% of Rotational Speed

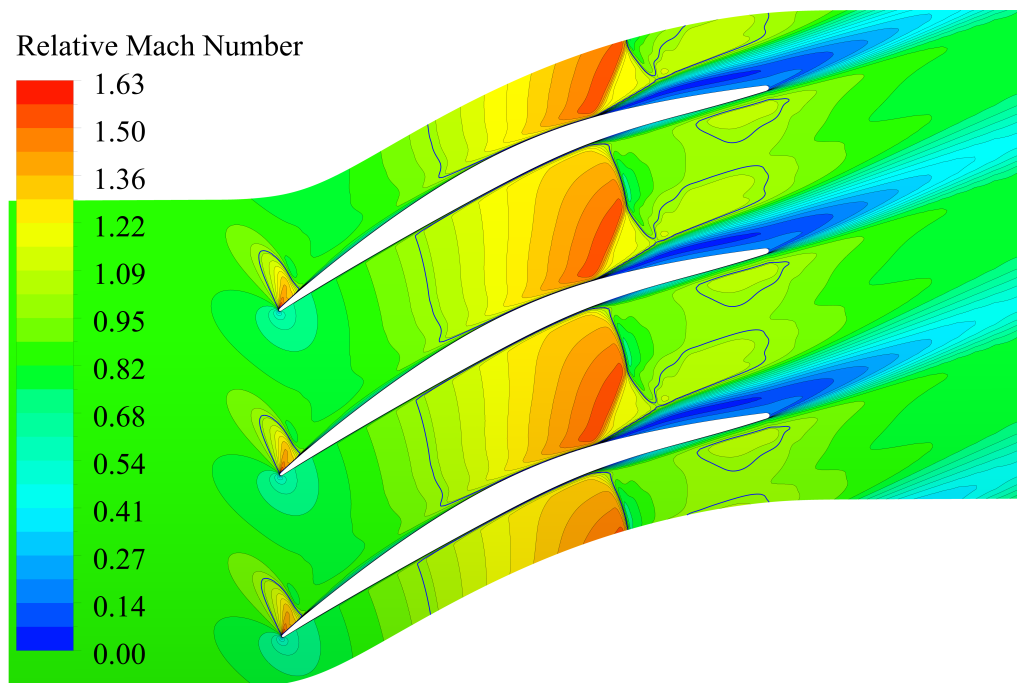


Figure 4.4: Mid-Span Relative Mach Number Contours at Choking Conditions and 50% of Rotational Speed

fact, one of the supersonic through-flow rotor characteristics is to have the choking plane located just in front of the blade passage as soon as the unique-incidence condition is established. A supersonic bubble is present in such location instead. A supersonic bubble is defined as a supersonic region surrounded by subsonic flow and is characterised by expansion waves travelling upstream. The higher the flow speed, the bigger the bubble until the whole relative inflow results supersonic. Therefore, the unique-incidence condition is the one that occurs as soon as the supersonic bubble is fully extended. Such conditions can be reached only by increasing the relative flow speed, which means by increasing the absolute axial inflow, the blade tangential rotational speed or both. In other words, for a fixed rotational speed the supersonic bubble at the blade tip is bigger if compared with the one present at the hub. That implies that the unique-incidence condition is firstly established at the blade tip section and it extends to the whole blade by further increasing the relative flow speed.

The mid-span relative Mach number contours at 60% of rotational speed are shown in Figure 4.5. It is visible how the supersonic bubble is now much more extended due to the higher relative flow speed. The blade meridional contours of the absolute Mach number at 65% of rotational speed are shown in Figure 4.6. The black lines represent the blade leading and trailing edges. The thick blue line represents the sonic conditions next to the leading edge. It can be noticed how the absolute sonic conditions are not present in the whole blade but are initially established only at the tip zone. Moreover, the transition is not linear and creates a sort of S-shaped contour just after the blade leading edge which, by the increase of rotational speed, is gradually moved to the blade hub.

The absolute Mach number contours and the mid-span relative Mach number contours with the associated velocity vectors at 75% of the rotational speed are shown in Figures 4.7 and 4.8. Due to the supersonic relative inflow, a bow shock is produced just in front of the blade leading edge which strength depends mainly by the leading edge bluntness and by the flow relative speed. The represented condition corresponds to the unique-incidence one. That is proven by the presence, in the relative frame of reference, of the

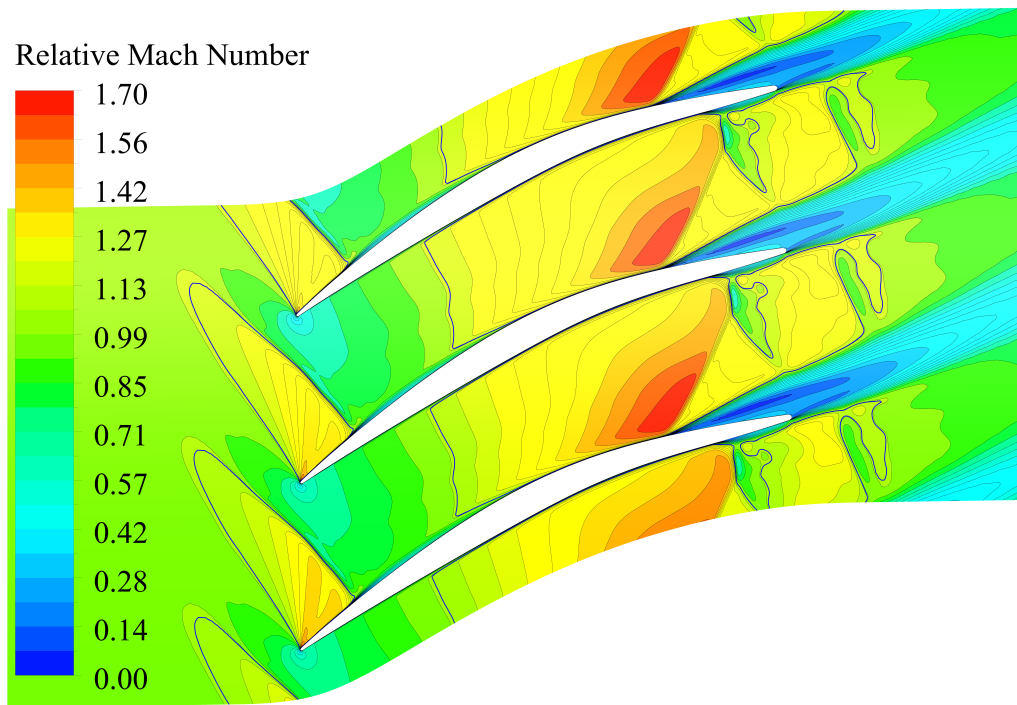


Figure 4.5: Mid-span Relative Mach Number Contours at Choking Conditions and 60% of Rotational Speed

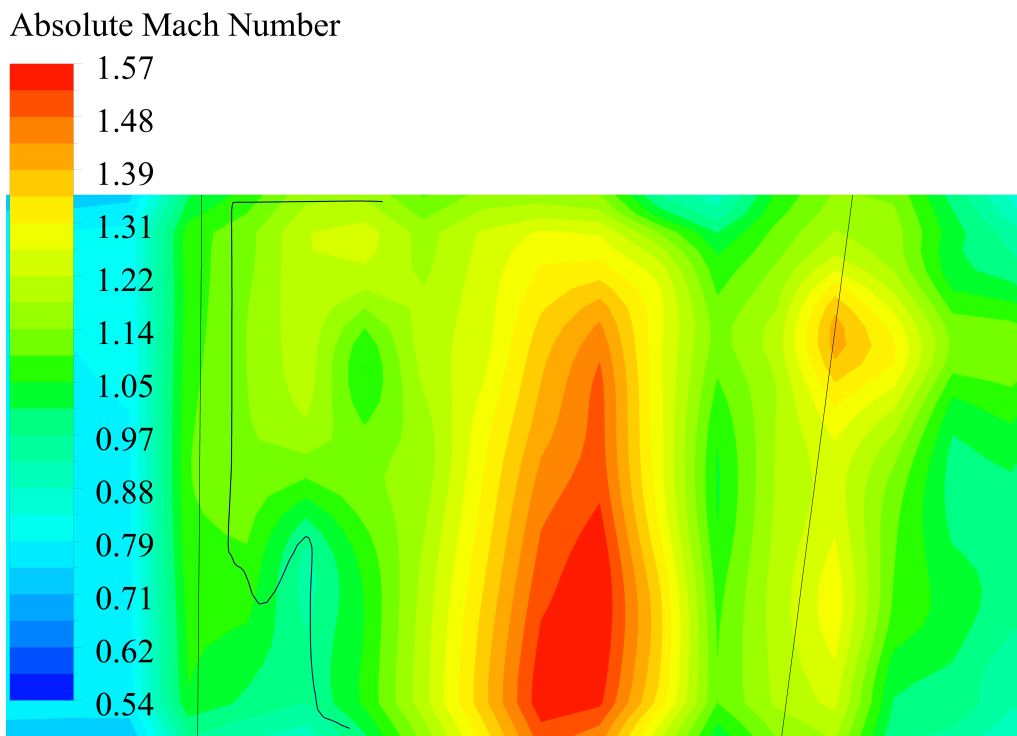


Figure 4.6: Meridional Absolute Mach Number Contours at Choking Conditions and 65% of Rotational Speed

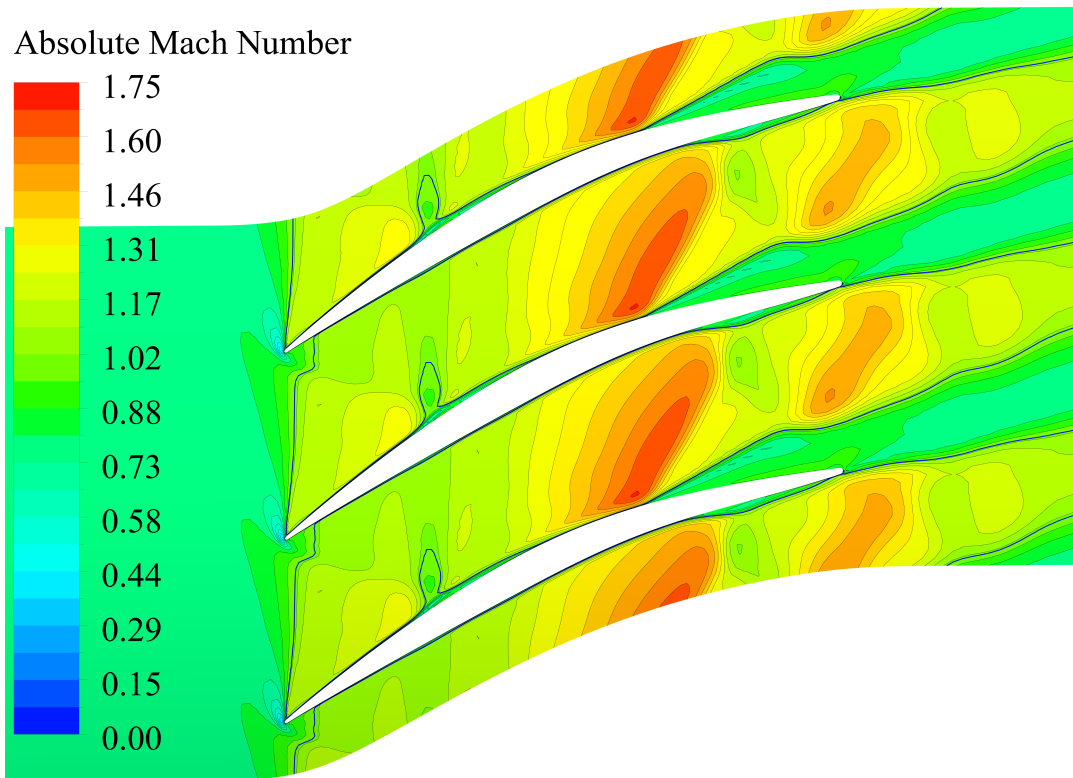


Figure 4.7: Mid-span Absolute Mach Number Contours at Choking Conditions and 75% of Rotational Speed

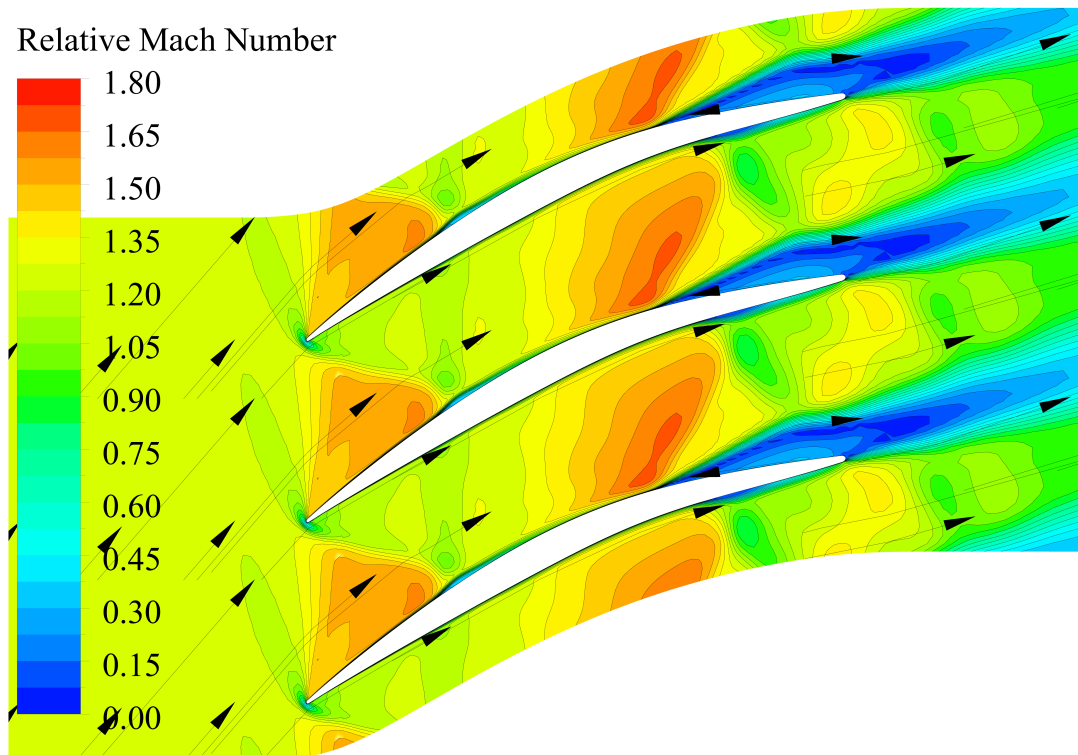


Figure 4.8: Mid-span Relative Velocity Vectors at Choking Conditions and 75% of Rotational Speed

expansion waves just after the bow shock which deploys upstream of the blade leading edges. Both the bow shock and the expansion waves cause the deflection of the flow before entering in the blade passage, forcing the flow to enter in the passage with just one possible incidence. The leading edge bow shock interacts with the suction surface of the adjacent blade causing the flow to create a separation bubble which in turn induces a strong normal shock which creates a subsonic region in the blade passage. In the absolute frame of reference, it is possible to notice the first captured Mach wave that lies just in front of the blade passage entrance, a condition in which the maximum possible mass flow is reached. In conventional transonic compressors, by increasing the relative flow speed, such Mach wave moves toward the leading edge. In the supersonic through-flow rotor, such Mach wave is located at the leading edge as soon as it is formed. Therefore, a further increase in rotational speed will result in the same qualitative flow but in a reduction in mass flow due to the increase of the bow shock strength and so due to a higher flow blockage effect.

Absolute and Relative Mach number contours at 100% of the rotational speed are shown in Figures 4.9 and 4.10. As stated before, the flow is qualitatively the same as the one at 75% of rotational speed but with stronger shocks. Both the separation bubble and the absolute flow choking in the blade leading edges plane are still present. The supersonic axial absolute inflow condition is not established due to the expansion waves travelling upstream of the blade passage. As soon as such waves are contained inside the blade passage, axial supersonic inflow conditions will be established. Since the maximum rotor rotational speed has been reached, that is possible only by increasing the axial inlet flow velocity.

4.1.2 Impulse-Type and Supersonic Through-Flow Operating Modes

The experimental rotor supersonic total pressure and efficiency maps are here presented along with the CFD results (Figures 4.11 and 4.12). As already stated in the previous section, neither during supersonic through-flow operating mode there is a turbulence model

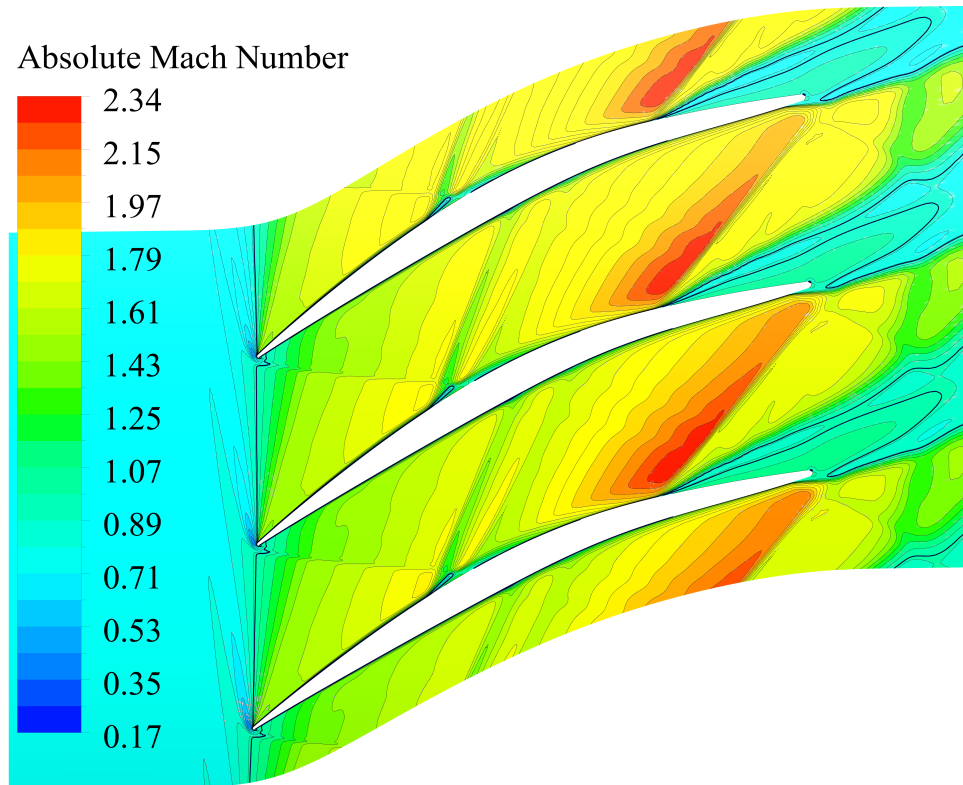


Figure 4.9: Mid-Span Absolute Mach Number Contours at Choking Conditions and 100% of Rotational Speed

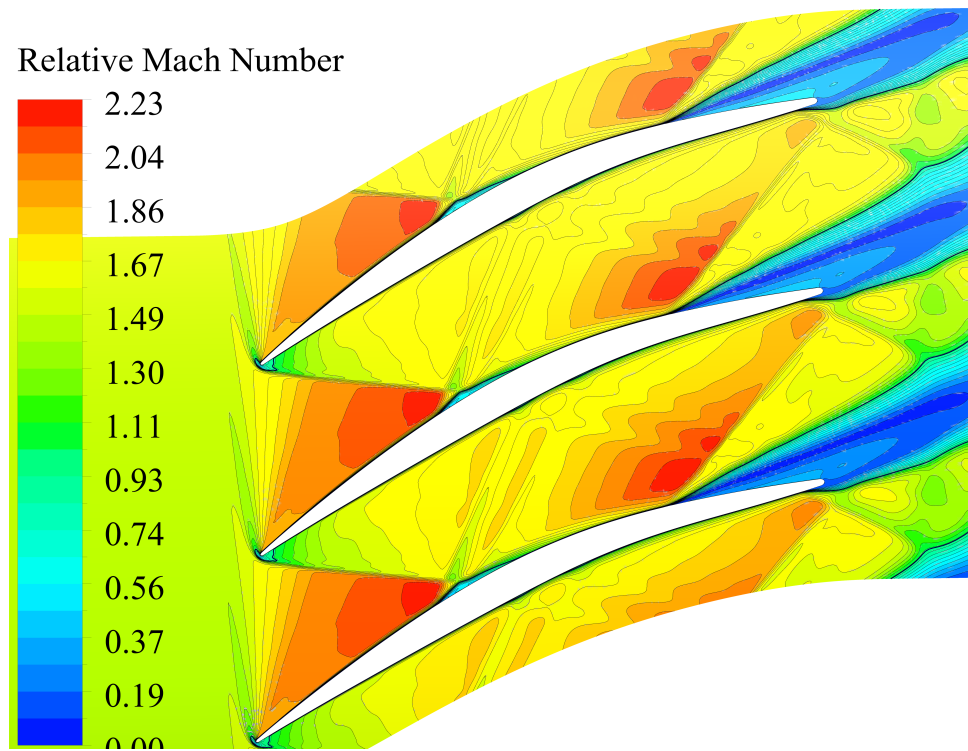


Figure 4.10: Mid-Span Relative Mach Number Contours at Choking Conditions and 100% of Rotational Speed

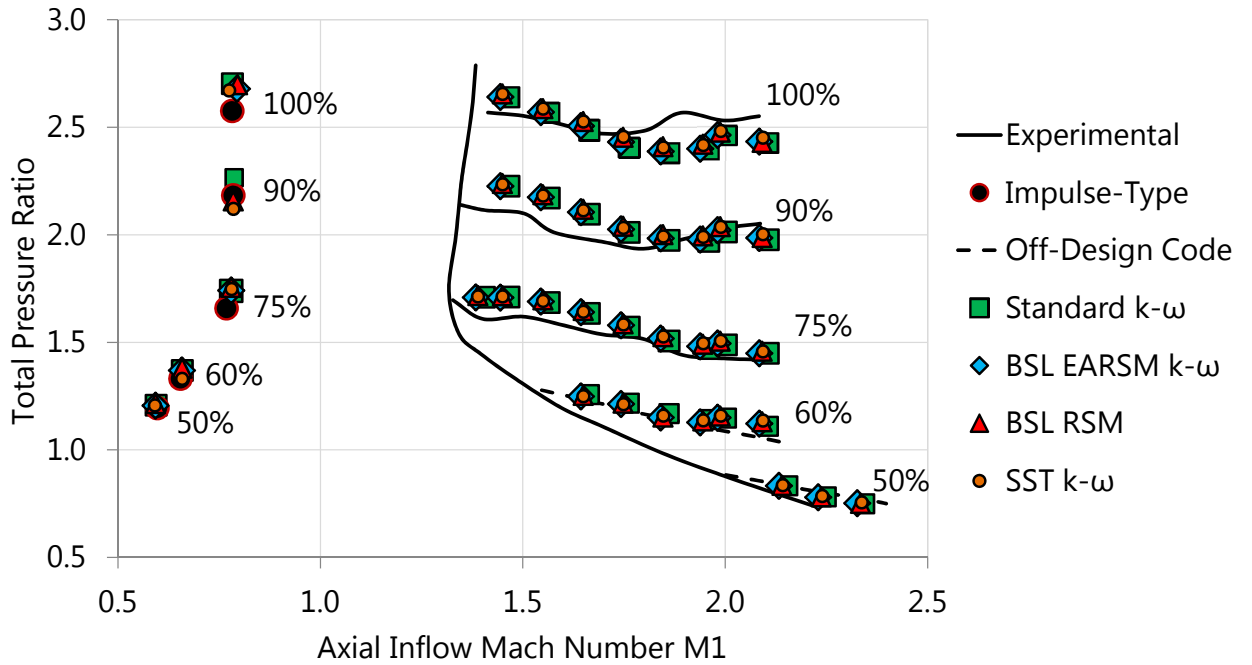


Figure 4.11: Supersonic Total Pressure Map

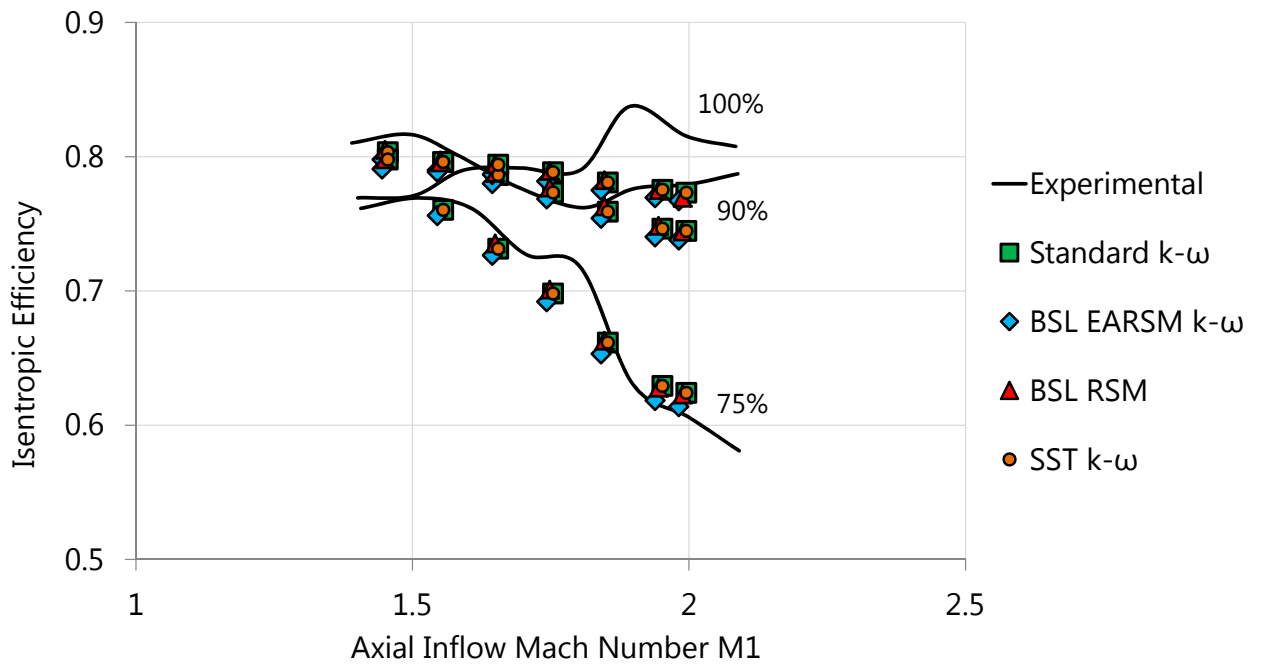


Figure 4.12: Supersonic Efficiency Map

which fits better the experimental results over the others. The total pressure and temperature were measured as done for the subsonic operating mode analysis. The only difference stands in the inlet Mach number which was evaluated at a station located 1.0 inch upstream of the blade leading edge. Since the supersonic through-flow conditions were established starting from 75% of the rotor rotational speed, the experimental data covers the conditions between 75% and 100% of the rotor rotational speed. The 60% and 50% speed lines were obtained by using an off-design code developed and used by NASA. As occurred in the subsonic case, the total pressure map has been well captured while the efficiency map has some discrepancies, particularly at higher rotational speed. That can be associated with the presence of experimental uncertainty bars which were extended up to $\pm 10\%$ from the reported value.

Both the impulse-type and the supersonic through-flow conditions are represented in the total pressure ratio map and are separated by the unstart boundary line. Such line is the one corresponding to the surge line during subsonic through-flow mode and represents the minimum axial Mach number needed in order to start supersonically the blade inflow. Concerning the supersonic through-flow rotor, the unstart that occurs at rotational speeds equal or below 60% is defined as a negative unstart since at such conditions the relative flow has a negative incidence. For a conventional transonic compressor, such unstart process occurs due to the leading edge oblique shock which, when the axial Mach number is low enough, moves upstream establishing the subsonic unique-incidence conditions. In the case of the supersonic through-flow rotor instead, the negative unstart process occurs as soon as the blade passage is choked. The started conditions are characterised by the movement and disgregation of the blade passage choking plane (Figures 4.13 and 4.14). As soon as the blade passage is not choked, the leading edge oblique shock is contained in the blade passage itself corresponding therefore to an absolute supersonic axial inflow. The unstart that occurs at 75% of the rotational speed is defined as a zero incidence unstart since the flow is almost tangent to the blade suction surface metal angle. Such unstart occurs also for positive incidence flows and so at higher rotational speeds. The unstart

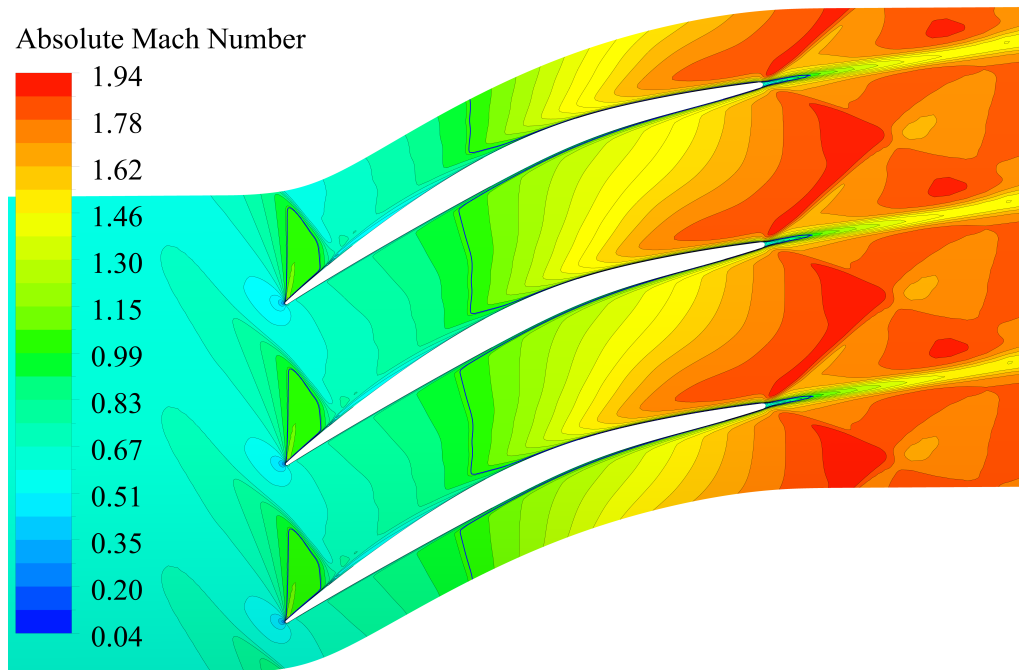


Figure 4.13: Mid-Span Absolute Mach Number Contours at Unstarted conditions and 60% of Rotational Speed

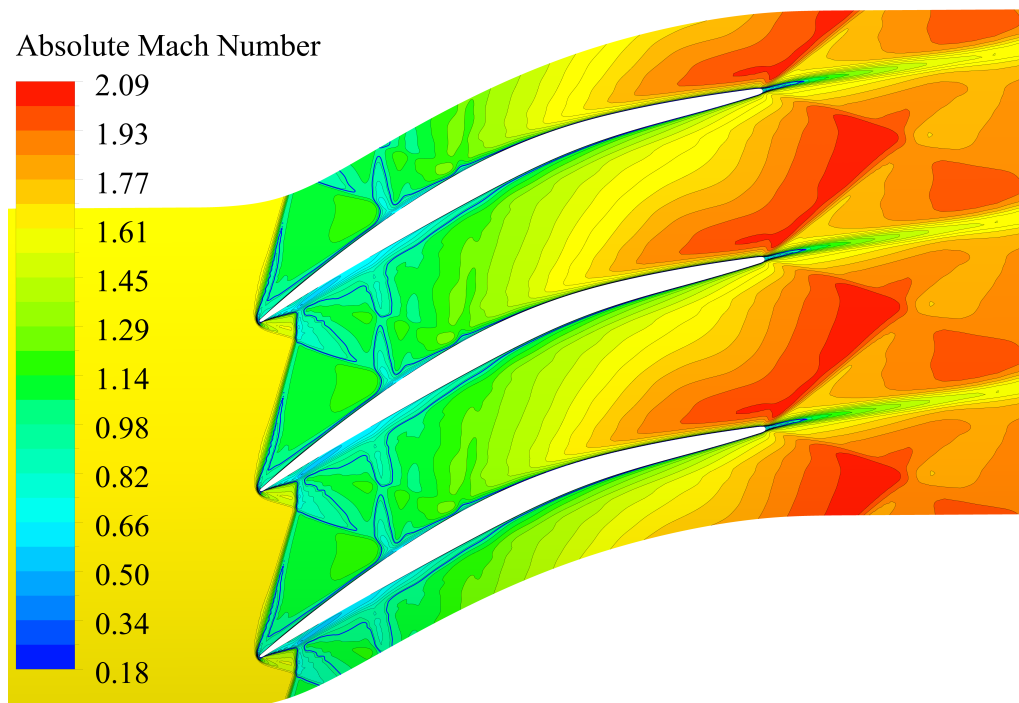


Figure 4.14: Mid-Span Absolute Mach Number Contours at Started conditions and 60% of Rotational Speed

is experienced due to the interaction between the expansion waves present just after the leading edge bow shock and the bow shock of the adjacent blade, clearly visible in the relative frame of reference (Figure 4.15). As soon as this interaction occurs, the bow shock moves upstream creating the unique-incidence condition. As stated before, one of the supersonic through flow rotor characteristics is the presence of the first captured Mach wave in the blade front plane as soon as unique-incidence is established (Figure 4.16). All the unstarted conditions also correspond to an impulse-type operating mode with axial subsonic inflow but an axial supersonic one.

As already described in section 2.3.2, the supersonic outflow starting in the test facility is done by opening the diffuser throat. Such condition can be easily replicated in CFD by reducing the normal back static pressure until the typical shock present inside the blade passage during the subsonic operating mode is moved outside, resulting therefore in a supersonic outflow. The flow characteristics are the same as the ones corresponding to a subsonic operating mode with the only difference that the outflow is now supersonic. The absence of the shock inside the blade passage permits to avoid the strong flow separation resulting in a higher isentropic efficiency if compared with a subsonic case at the same rotational speed.

During supersonic through-flow operating mode, the higher the flow speed, the more contained are the shock waves. At design point conditions, the shock is wholly contained inside the blade passage due to the axial inflow Mach number being equal to 2.0. In the absolute frame of reference, it is possible to see an oblique shock originating from the blade leading edge and impinging in the adjacent blade pressure surface (Figure 4.17). A bow shock is instead present in the relative frame of reference. The main difference from the other operating points is that, since the bow shocks are contained in the blade passage, they interact next to the blades' pressure surfaces. After the interaction, each bow shock is then attenuated by the expansion waves present just after them (Figure 4.18). The shocks are attenuated until they vanish inside the blade passage itself. Moreover, this results in a smaller bubble at the blades' suction surfaces if compared with the axial subsonic inflow

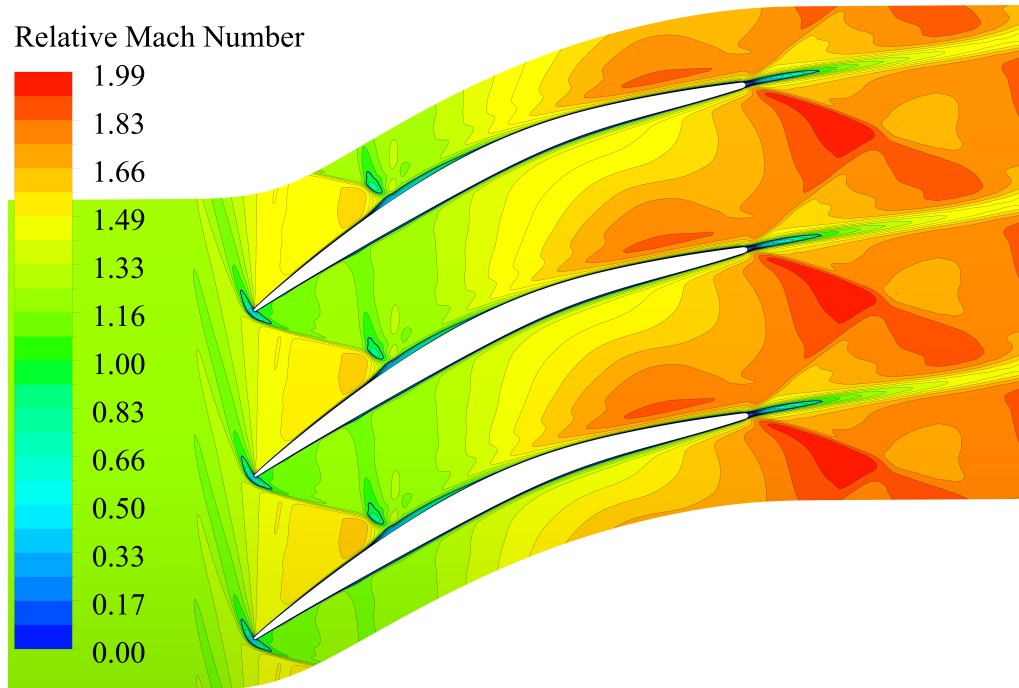


Figure 4.15: Mid-Span Relative Mach Number Contours at Unstarted conditions and 75% of Rotational Speed

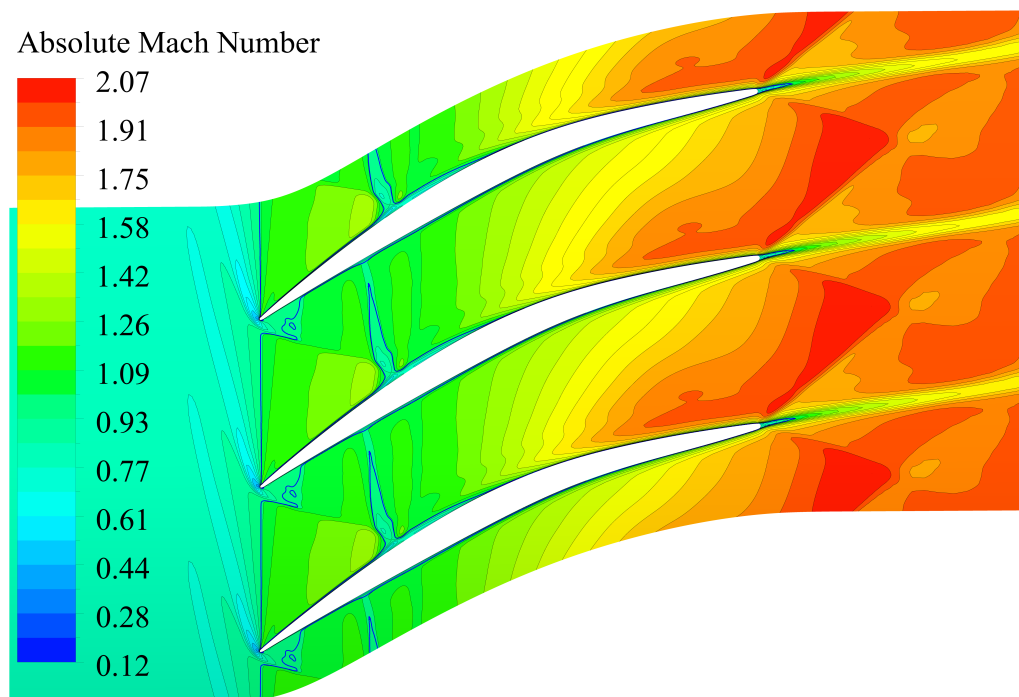


Figure 4.16: Mid-Span Absolute Mach Number Contours at Unstarted conditions and 75% of Rotational Speed

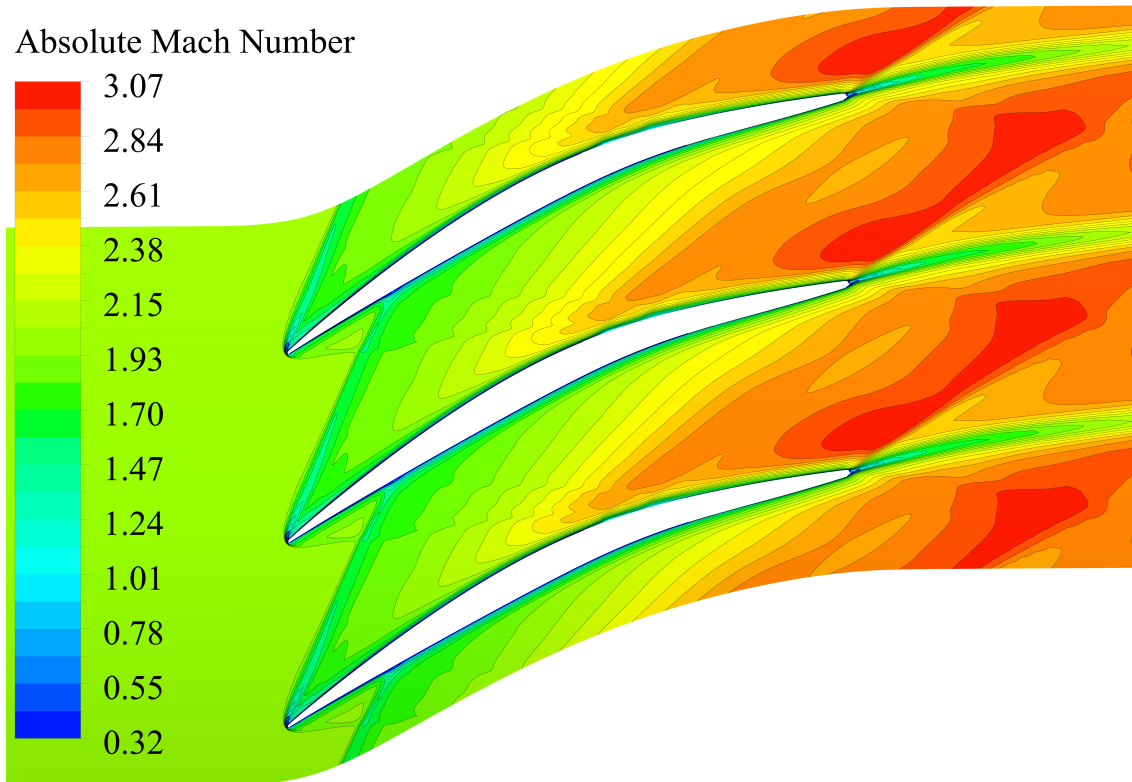


Figure 4.17: Mid-Span Absolute Mach Number Contours at Design Point

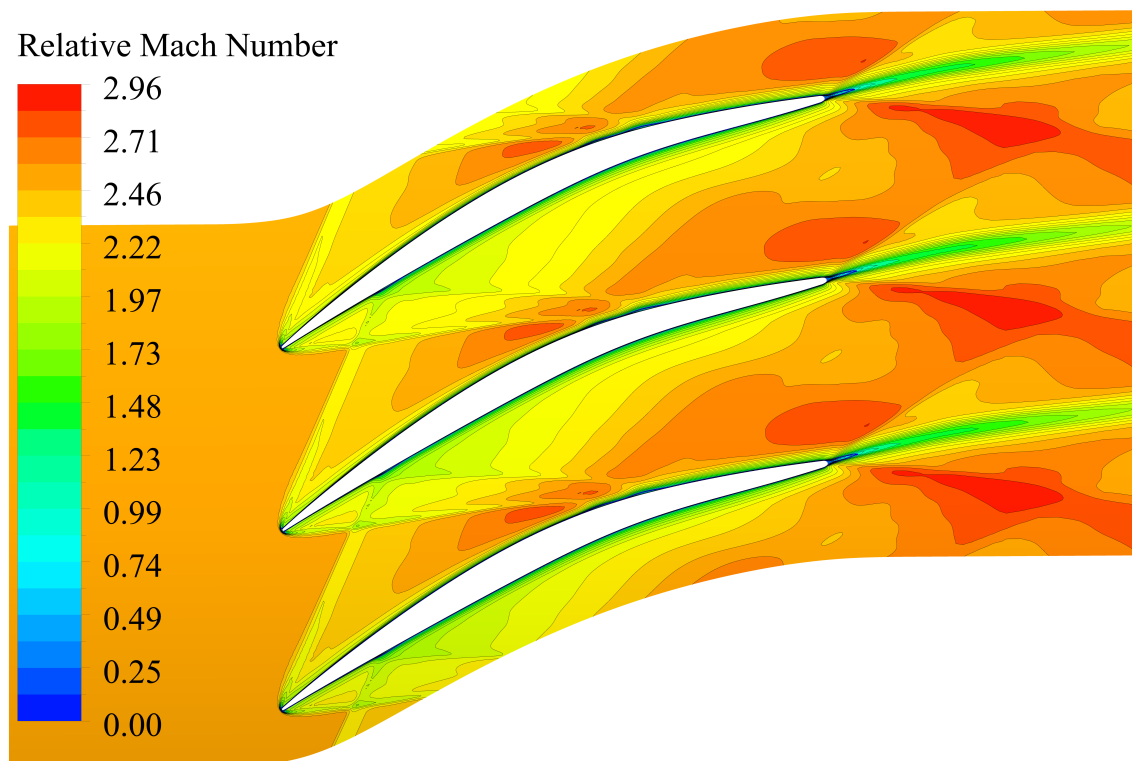


Figure 4.18: Mid-Span Relative Mach Number Contours at Design Point

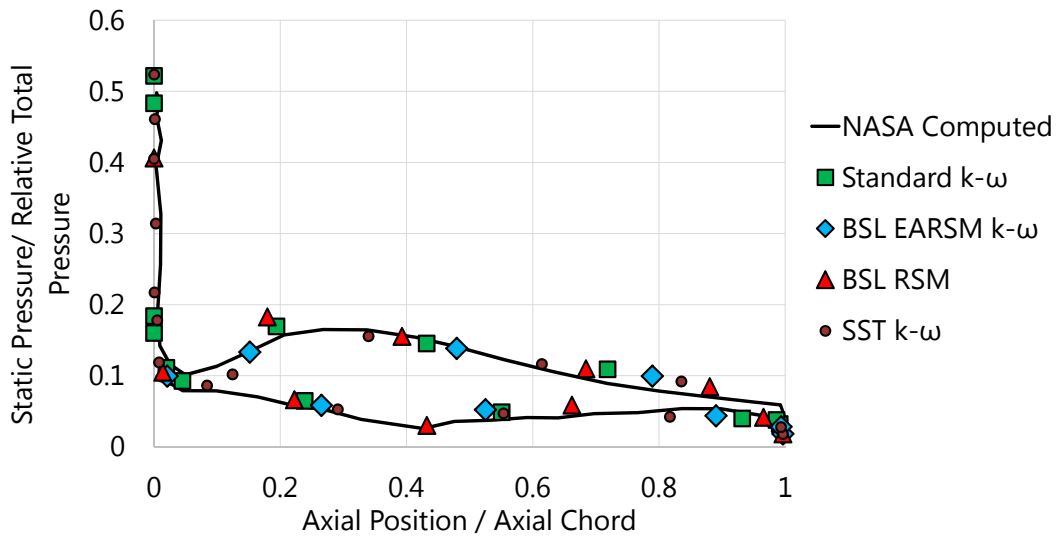


Figure 4.19: Hub Blade Loading at Design Point

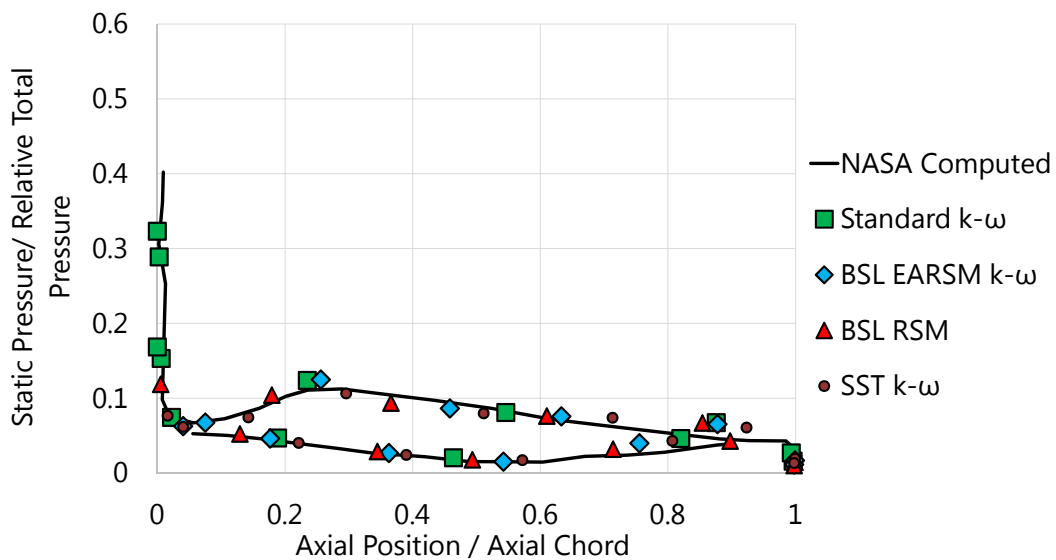


Figure 4.20: Tip Blade Loading at Design Point

conditions.

The NASA computed design point blade loadings at both the blade hub and tip are reported along with the CFD results (Figures 4.19 and 4.20). No turbulence model captures better the blade loading over the others. Based on the showed results, it can be stated that the blade model has been validated with success.

4.2 Optimisation Process

As already described in section 3.6, the design variables are some of the blade angle and thickness distributions discretisation points. Since the optimiser requires a limited number of design variables, the original blade geometry has been adapted in a way to satisfy such constrain. The optimised blade geometry distributions are presented in Appendix B.5. The nomenclature regarding the new discretisation points is presented in the same section and will be used from now on. The optimised blade geometry is extracted from a Pareto front generated by a genetic algorithm applied to the results of a previously produced response surface. The response surface generation and so the whole optimisation, are based on simulations at the design point flow conditions. Since no significative difference existed between the turbulence models, Standard $k - \omega$ has been used during the optimisation process due to its lower computational cost.

4.2.1 Response Surface Generation

The most critical part associated with the generation of the response surface is related to its goodness of fit, as presented in section 3.6.3. The response surface on which the genetic algorithm has been used was initially generated with a total of 189 learning points, as required by the LHS DoE method. The surface was then refined by using 50 verification points and by checking the goodness of fit at each step. In the case the goodness of fit was not satisfactory, the produced verification points were used as refinement points, and a new set of 50 verification points were produced in order to check the quality of the refined surface. The final response surface is constituted of 600 refinement points, for a total of 789 learning points. The final surface goodness of fit is presented in both Figure 4.21 and Table 4.1. The used criteria are described in section 3.6.3. All the represented points values are normalised relative to the input data range. The diagonal represents the optimal situation since it corresponds to the same output values provided by both the response surface and the verification points.

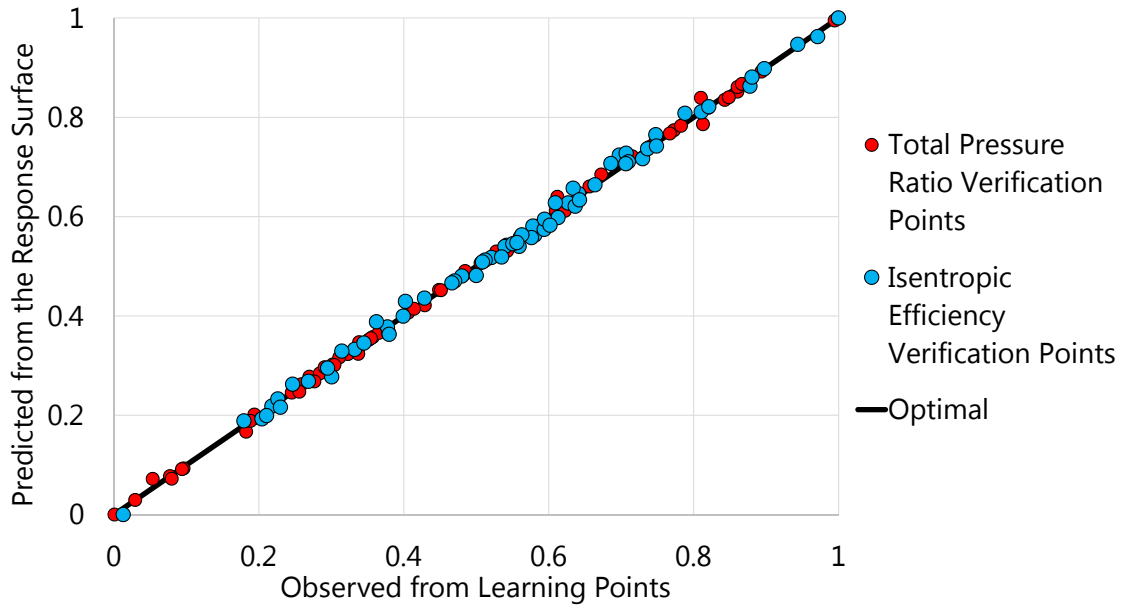


Figure 4.21: Predicted and Observed Outputs

Table 4.1: Goodness of Fit Criteria

Criterion	Total Pressure Ratio	Isentropic Efficiency
Coefficient of Determination	0.998	0.987
Root Mean Square Error on Learning Points	$1.33e^{-8}$	$3.58e^{-7}$
Root Mean Square Error on Verification Points	0.006	0.155
Relative Average Absolute Error on Learning Points (%)	0.0	0.0
Relative Average Absolute Error on Verification Points (%)	1.74	3.66

Since the verification points are not taken into account in building the response surface, the closer they are to the diagonal the better the response surface is predicting the outputs. As expected, the isentropic efficiency is more difficult to predict, but the results can be considered satisfactory.

A characteristic which is automatically provided with the response surface generation is the input parameters' local sensitivity which allows to verify the impact of the input parameters on the output ones. The term 'local' refers to the fact that the calculations consider the outputs variations based on the change of a single input and by keeping fixed the other ones. A higher sensitivity corresponds to a more significant change of the output parameter when varying a particular input. A positive value corresponds to a direct proportionality between the input and the output parameter, while a negative value corresponds to an inverse proportionality between the input and the output parameter. A sensitivity study can be used in order to limit the number of input parameters for a future optimisation loop, reducing the response surface generation difficulties and the associated computational cost.

The total pressure ratio and isentropic efficiency local sensitivity charts are reported in Figure 4.22 and 4.23. The used nomenclature is the same as the one reported in Appendix B.5. It is possible to notice how, for both the efficiency and the pressure ratio, the input parameters that influence more the performances are the ones relative to the mid-span layer. In order to visualise the response surface, an N-dimensional space is needed, where N is the sum of input and output parameters that the user wants to visualise. For the sake of simplicity, only 3D surfaces are here reported. Two of the possible 3D surfaces are presented in Figure 4.24 and 4.25, respectively one for the total pressure ratio and one for the isentropic efficiency. The whole optimisation process, including the response surface generation, is carried out by using the outputs calculated automatically by ANSYS[®] which considers the total pressure and total temperature at the domain inlet and outlet. The reported values of such outputs are slightly lower than the actual ones.^[1] In any case, the optimisation process aim is to identify the geometry characteristics at which the blade performs better. If the outputs are computed consistently during the whole optimisation study, such geometry characteristics are captured, independently from the outputs values.

¹By actual total pressure ratio and isentropic efficiency are meant the ones obtained by measuring total pressure and temperature at the experimental rake positions. By doing so, a direct comparison with the original design is possible since its performance maps are based on the measurements at such locations.

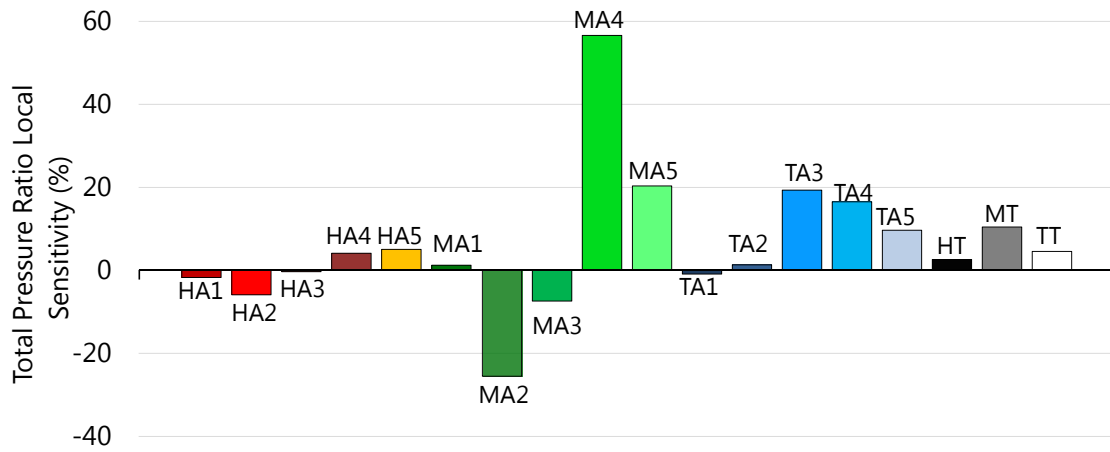


Figure 4.22: Total Pressure Ratio Local Sensitivity



Figure 4.23: Isentropic Efficiency Local Sensitivity

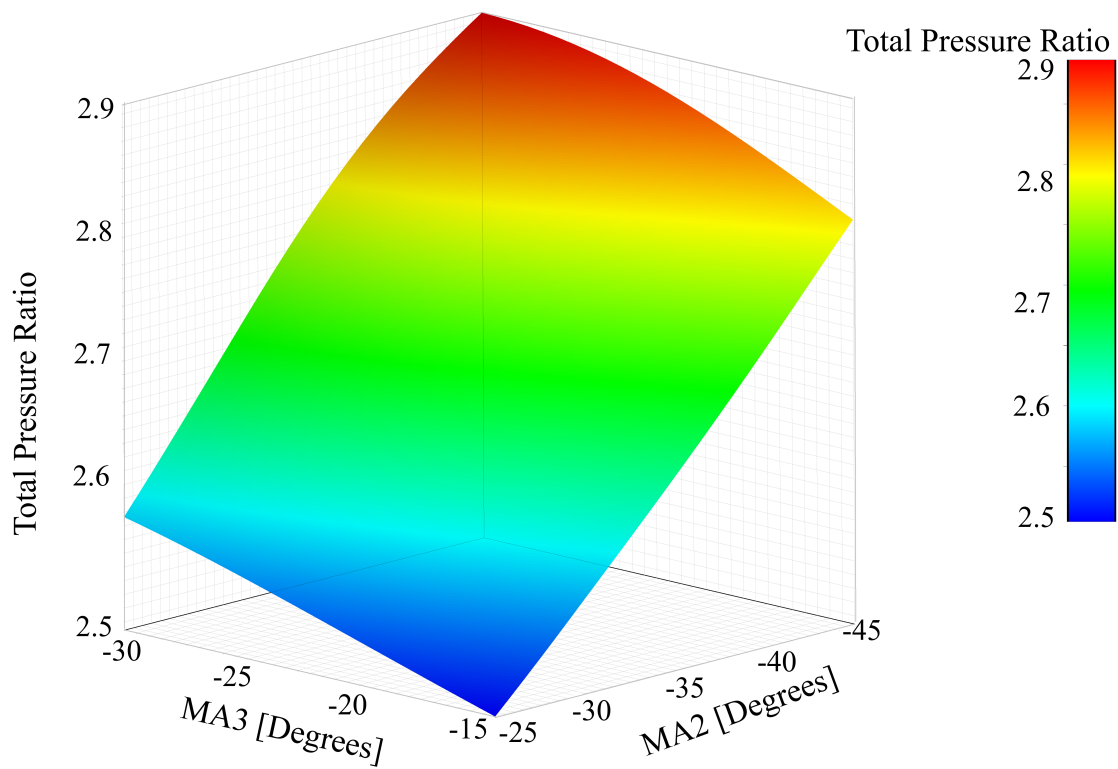


Figure 4.24: Total Pressure Ratio Response Surface

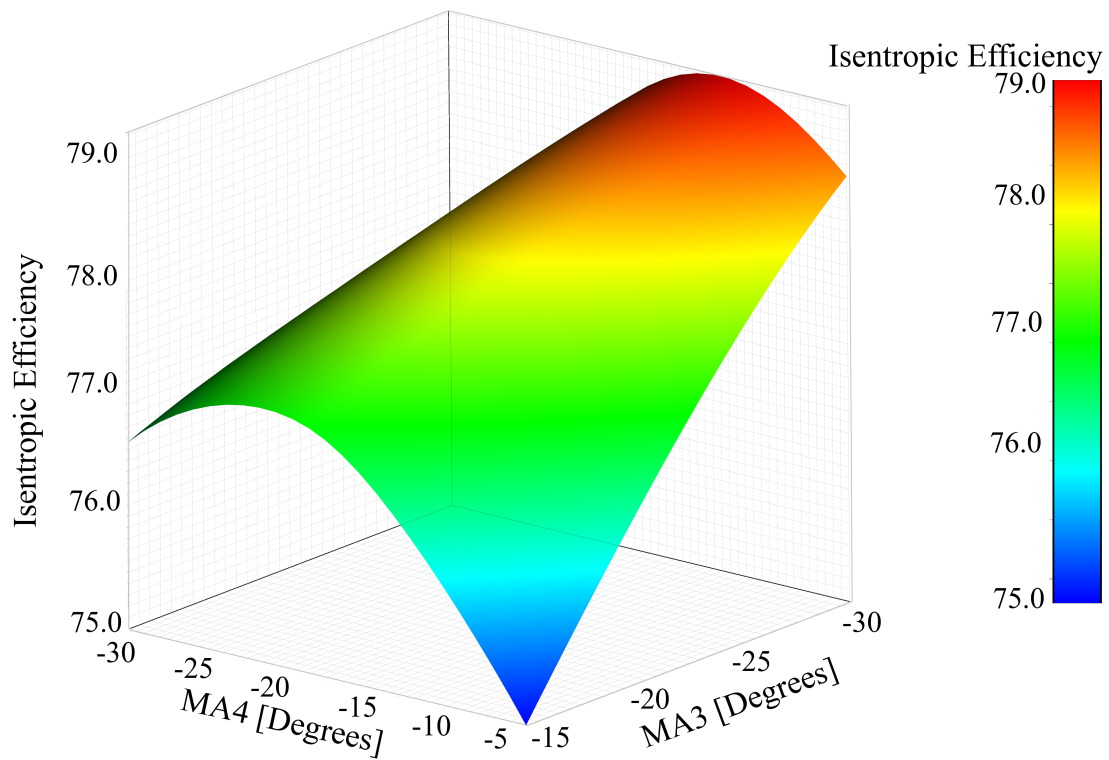


Figure 4.25: Isentropic Efficiency Response Surface

This means that the optimal point captured by the optimisation process will still be in all likelihood the actual optimal point.

Since the angle discretisation points at the mid-span layer are the ones that influence more both the outputs, some of such input points are used to show the response surfaces. All the other input parameters are fixed at the values corresponding to the final optimised blade geometry which is reported in Appendix B.5. The shapes of the response surfaces confirm the local sensitivity prediction. In Figure 4.24, the two input parameters are inversely proportional to the total pressure ratio. Hence, a reduction of their values brings to a higher total pressure ratio. In Figure 4.25, one of the inputs is directly proportional to the isentropic efficiency (MA4), while the second one is inversely proportional to it (MA3). The result is an arc-shaped surface with the maximum nearer to the extreme value of the input parameter with the higher local sensitivity (MA3).

4.2.2 Pareto Front Generation

The result of every multi-objective optimisation algorithm is a tradeoff chart between two or more outputs. From such a chart, it is possible to evidence a first Pareto front which is defined as a group of optimal solutions consisting of non-dominated points. A non-dominated point is a point for which, when considered in regard to another point, is the best solution for any of the optimisation objectives. In other words, a first Pareto front is the group of best possible design points presented in the tradeoff chart.

The first Pareto front generated by the genetic algorithm applied to the blade geometry is presented in Figure 4.26. For this particular case, all the design points below the first Pareto front are worse if compared to the front ones and no design point exists above it. Therefore, all the points that lie on the front are possible candidate points. The choice of a candidate point over another depends on the rotor application. The chosen design is shown in Figure 4.26. It corresponds to a total pressure ratio of 2.867 and an isentropic efficiency of 78.89%.

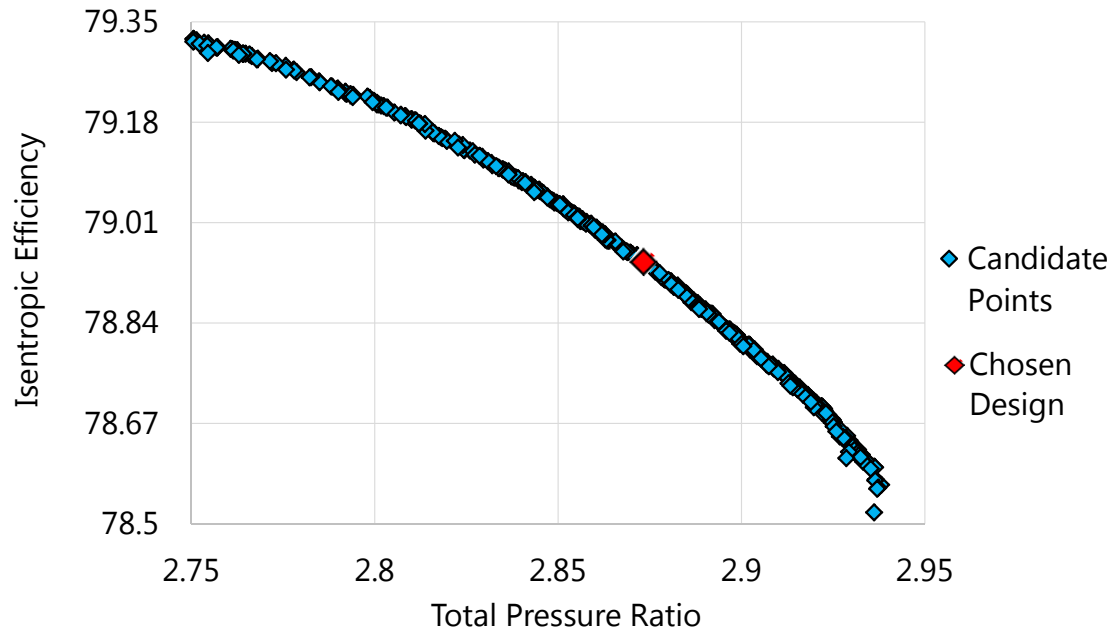


Figure 4.26: First Pareto Front

4.3 Optimised Blade Model

The final blade geometry distributions are reported in Appendix [B.5](#), while the hub, mid and tip sections compared with the original blade ones are presented from Figure [4.27](#) to Figure [4.29](#). One of the optimisation process constrains was to keep fixed the leading and trailing edges projections on the meridional plane. Hence, the optimised blade does not present any sweep difference from the original one. Almost no difference exists in both the blade exit angle and the blade suction surface angle. Therefore, both the possible axial supersonic outflow establishment and the peculiar characteristic of reaching the maximum mass flow condition as soon as unique-incidence is established are maintained (the first captured Mach wave is still generated directly next to the leading edge as occurred with the original blade). Due to this features, the main flow field characteristics of the optimised blade are expected to be the same as the original one. The main difference between the two blades stands in the blade passage area distribution that the relative flow sees (Figure [4.30](#)). The throat location of the optimised blade is moved upstream and the blade passage results generally wider.

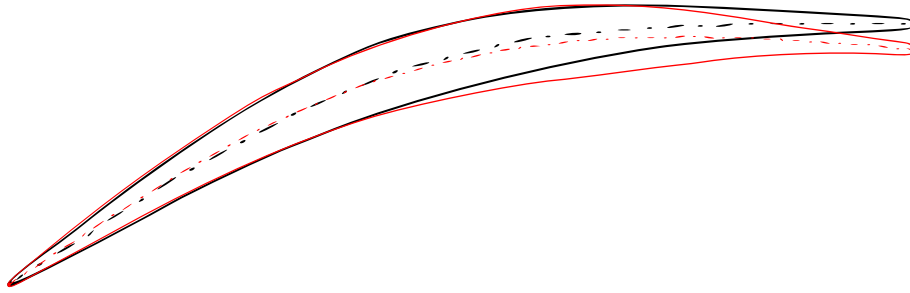


Figure 4.27: Optimised (Red) and Original (Black) Blade Hub Sections

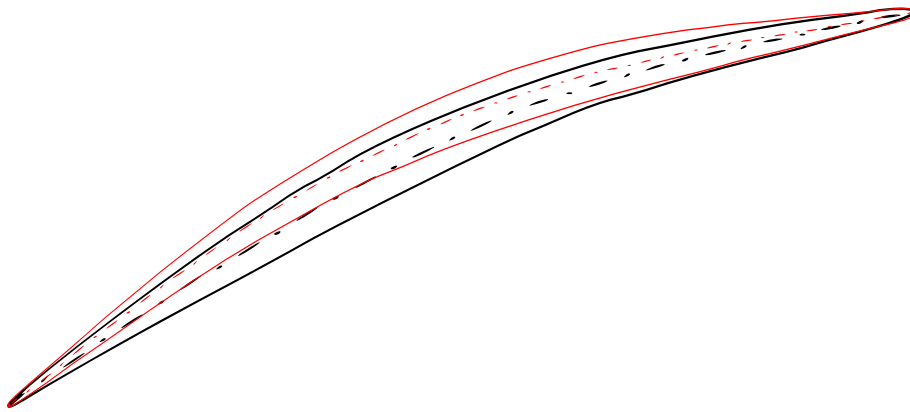


Figure 4.28: Optimised (Red) and Original (Black) Blade Mid Sections

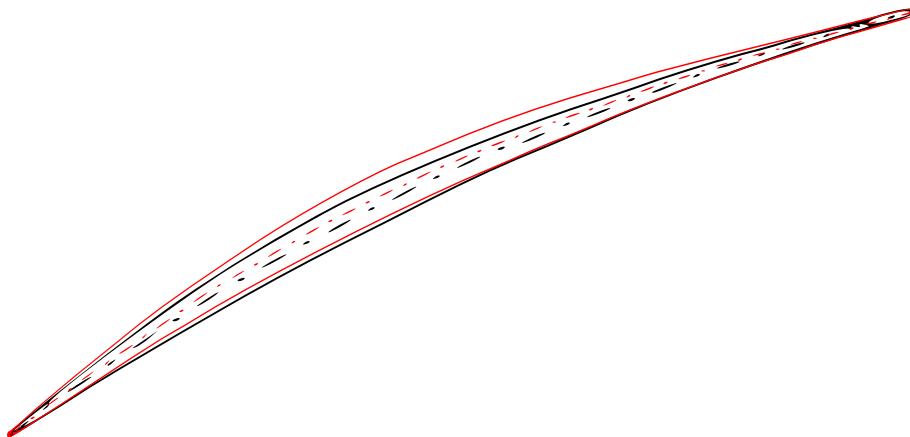


Figure 4.29: Optimised (Red) and Original (Black) Blade Tip Sections

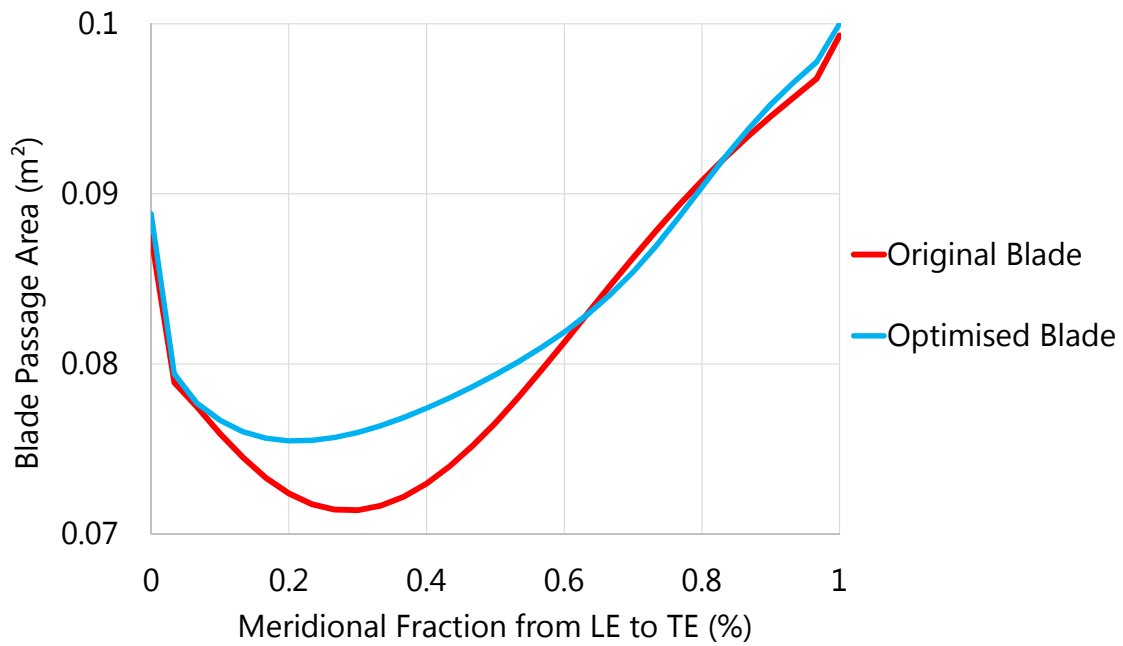


Figure 4.30: Blade Passage Area Distributions for the Original and Optimised Blades

Table 4.2: Blade Solidities

Layer	Original Blade Solidity	Optimised Blade Solidity
Hub	3.56	3.51
Mid	3.27	3.24
Tip	3.11	2.95

In the first part, the divergent part is less aggressive ending up being more aggressive at the back. The leading edge front area is slightly wider in the case of the optimised blade. The original and optimised blade solidities are presented in Table 4.2. The optimised blade presents a lower blade solidity for each layer.

A comparison between the design point performance predicted by the response surface and the one predicted by the CFD simulation is presented in Table 4.3. The response surface prediction and the CFD results are the ones computed automatically by ANSYS[®] which do not correspond to the actual ones due to the measurement location different from the experimental rakes one. The actual rotor performance is presented in the respective performance maps showed in the next sections. As expected the difference between the

Table 4.3: Response Surface Prediction and CFD Results Comparison at Design Point

Property	Response Surface	CFD Simulation	Δ (%)
Total Pressure Ratio	2.867	2.886	0.66
Isentropic Efficiency	78.89	78.04	1.08

predicted and computed isentropic efficiency is larger than the total pressure ratio one.

4.3.1 Subsonic Through-Flow Operating Mode

The optimised blade subsonic performance maps are presented along with the original blade performances in Figures 4.31 and 4.32. The rotational speeds reported in the maps are relative to the NASA experimental data and therefore to the original blade model. The rotational speeds relative to the optimised blade are reported in the legends. As expected, the map trends are the same meaning that the blades behave in the same way. No significant improvement in terms of performance is present². The only significant difference stands in the axial inflow Mach number measurements. For a fixed rotational speed, the optimised blade choking occurs after the original blade one. Particularly, the choking conditions of the optimised blade correspond to the choking conditions of the original one at a rotational speed of 10% higher. For instance, it is possible to notice how the 50% speed line of the optimised blade superimposes utterly with the 60% one of the original blade since, at such rotational speed, the blade results always choked. This behaviour can be justified by the presence of a wider blade passage throat area for the optimised blade which corresponds to a higher inlet mass flow in choking conditions. Unique-incidence condition is firstly established at 65% of the rotational speed rather than at 75% as occurred with the original one. In such conditions, the choking plane moves at the leading edge front line. Hence, the inlet mass flow is proportional to the blade passage front area. Since the optimised blade presents a slightly larger front area, the unique-incidence condition shows a higher inlet mass flow. Therefore, for a fixed rotational speed, the speed

²This is not an unexpected situation since the optimisation process has been carried out for the design point conditions only.

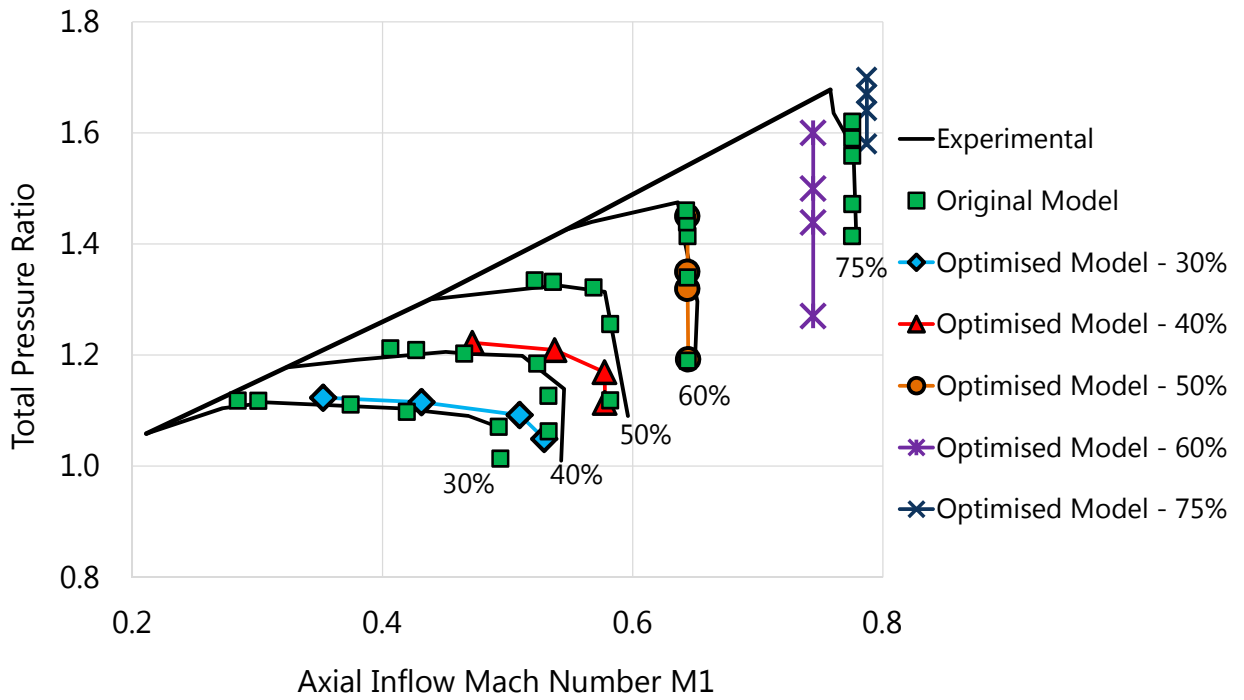


Figure 4.31: Subsonic Total Pressure Map

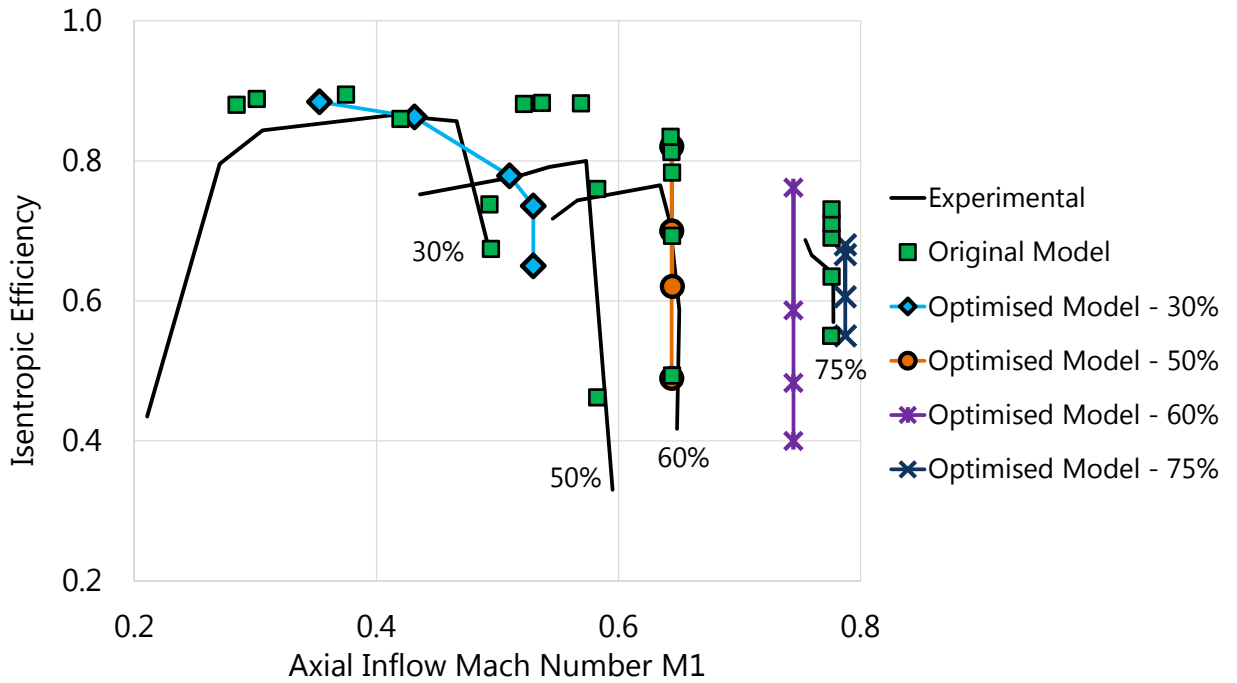


Figure 4.32: Subsonic Efficiency Map

lines at which correspond unique-incidence condition present a higher inflow Mach number than the original model's ones. The only difference between unique-incidence condition speed lines stands in the total pressure ratio due to the different rotational speed. The 65% speed line would be located at the same position as the 75% one but with a lower maximum total pressure ratio.

The optimised blade absolute and relative Mach number contours at 50% of the rotational speed are shown in Figures 4.33 and 4.34. As usual, the thick blue line represents the choking location. By comparing such contours with the original blade ones, it is possible to notice how the choking plane of the optimised blade is slightly closer to the leading edge³. The maximum relative Mach number is lower than the original blade one, probably due to the less aggressive blade passage divergence after the throat. Due to the new geometry, the absolute flow tends to be more axial and so is faster if compared with the relative one. As anticipated, the main flow field characteristics are the same as the original blade ones. It is possible to notice the presence of the supersonic bubble which dimensions depends on the relative flow speed in the leading edge zone. Also in the optimised blade the unique-incidence condition occurs as soon as the bubble is fully developed, which corresponds to a supersonic relative inflow.

4.3.2 Impulse-Type and Supersonic Through-Flow Operating Modes

The optimised blade supersonic performance maps are presented along with the original blade performances in Figures 4.35 and 4.36. In the total pressure ratio map, both the supersonic and the impulse-type operating modes are presented. For the supersonic operating mode, the mass flow is proportional to the first captured Mach wave length and to the blockage effect caused by the leading edge bow shock, which is, in turn, proportional to the shock strength. Such strength depends mainly on the leading edge bluntness and the relative flow speed. No difference exists in the leading edge bluntness between the

³Referring to the relative frame of reference since the blade passage area distributions are evaluated in such frame of reference.

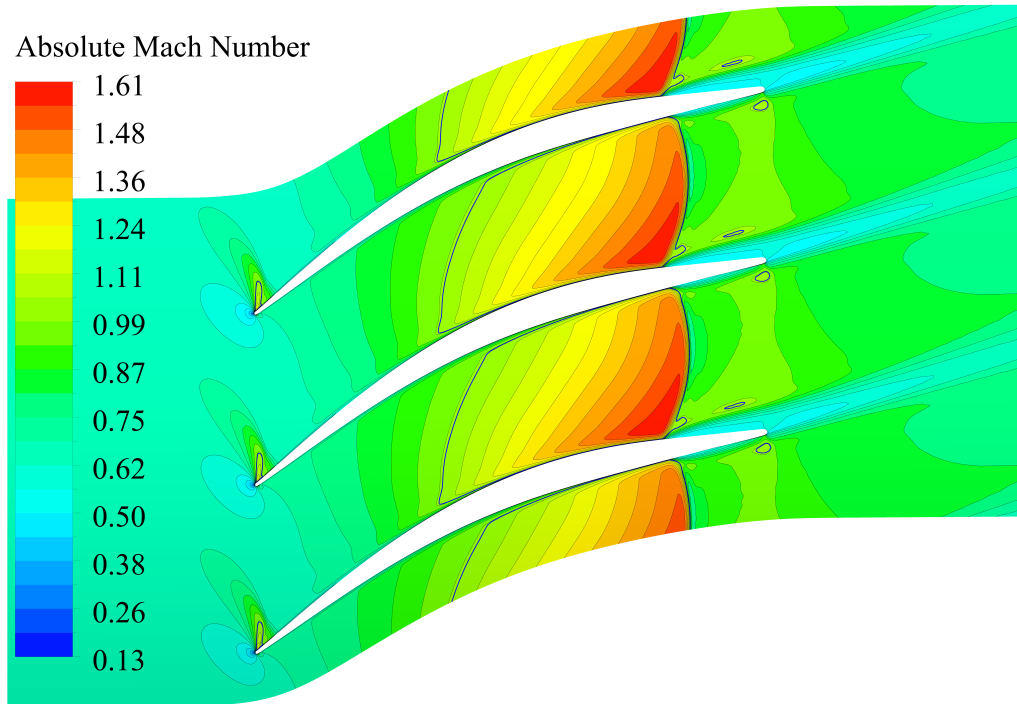


Figure 4.33: Optimised Blade Mid-Span Absolute Mach Number Contours at Choking Conditions and 50% of Rotational Speed

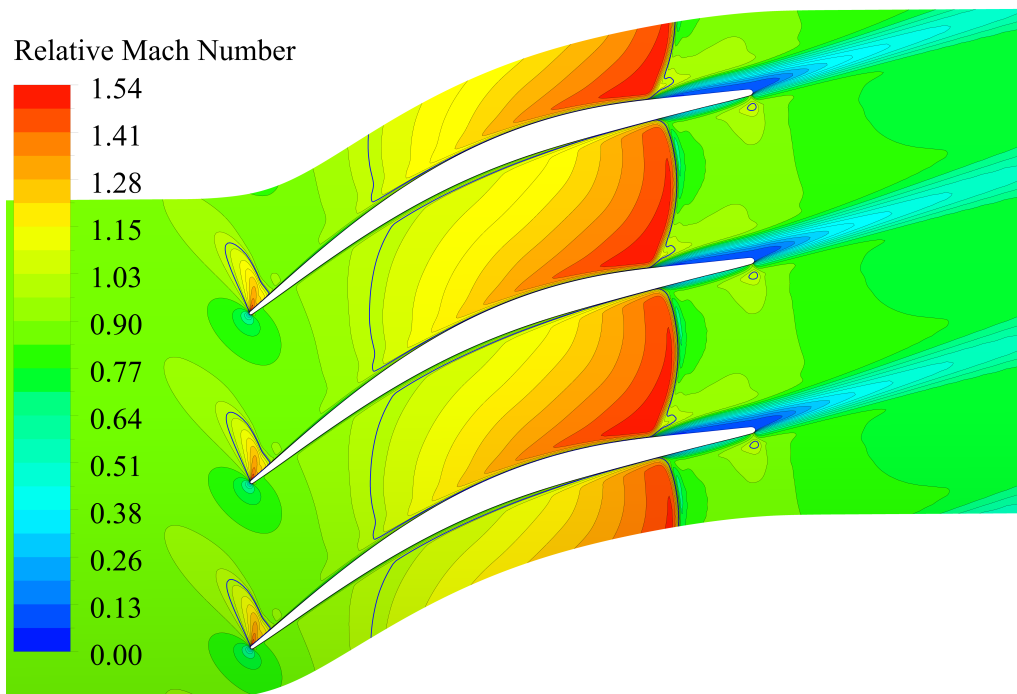


Figure 4.34: Optimised Blade Mid-Span Relative Mach Number Contours at Choking Conditions and 50% of Rotational Speed

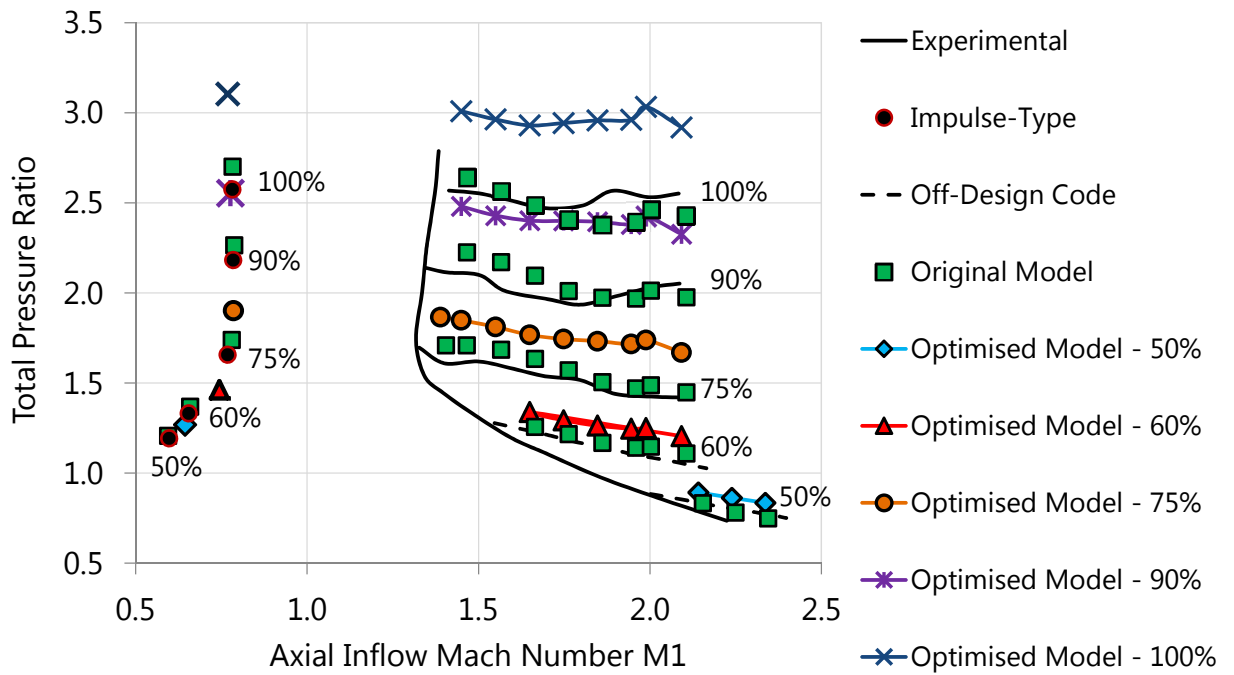


Figure 4.35: Supersonic Total Pressure Map

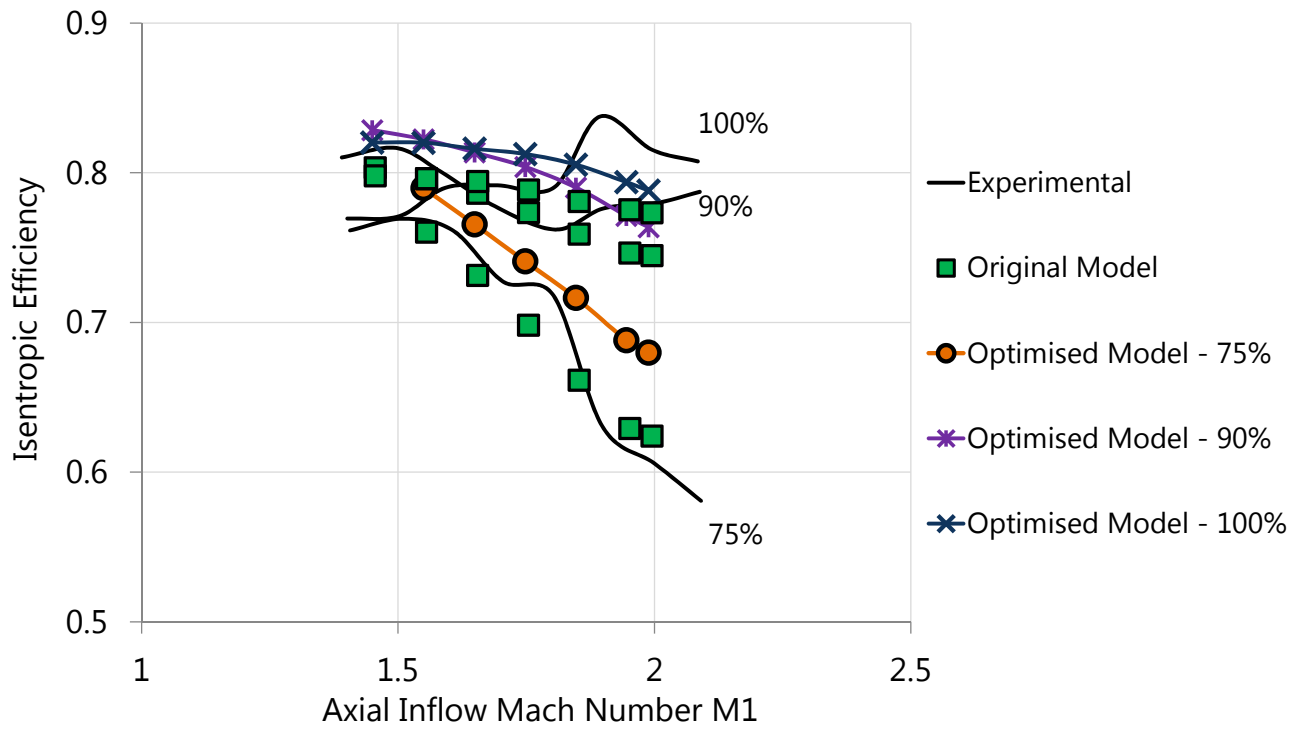


Figure 4.36: Supersonic Efficiency Map

two blade geometries. Since the inlet relative flow speed depends mainly on the blade rotational speed, no substantial difference exists even in the inlet relative flow speed. In other words, during supersonic operating mode, the mass flows of the original and the optimised blade are nearly the same. Different is the case for the impulse-type operating mode. During such operating mode, the mass flow is limited by the choking plane that, depending on the rotational speed, lies in the leading edges front plane or inside the blade passage. Therefore, the observations done for the subsonic operating mode apply also to the impulse-type one. That justifies the difference, at the lower rotational speeds, in the axial inflow Mach number between the two blades for the impulse-type operating mode. Once the unique-incidence condition is established, as stated before, such difference vanishes. The axial inflow supersonic start and unstart occurs in the same way as in the original blade. It is still possible to distinguish between positive and negative unstart depending on the relative flow incidence. Negative unstart occurs when the blade passage chokes, while positive unstart occurs when the leading edge expansion waves interact with the bow shock of the adjacent blade.

For both the impulse-type and the supersonic through-flow operating modes, an evident difference in performances is this time present between the two blades. Such difference increases while approaching design point conditions. The design point flow characteristics are qualitatively the same as the original blade ones (Figures 4.37 and 4.38). Both the absolute and relative Mach numbers in the blade passage are higher if compared with the original blade ones. That is caused by the shorter convergent part of the blade passage area which, therefore, decelerates less the supersonic flow. The only evident difference is the separation bubble location. Due to the lower blade solidity, the leading edge reflected bow shock impinges the suction surface of the adjacent blade in a more downstream position causing the development of the separation bubble in such location rather than closer to the leading edge. Another main difference between the two blade designs is a marked blade concavity in the optimised one (Figures 4.39 and 4.40). Due to this geometric feature, the optimised blade can turn slightly more the flow resulting in a

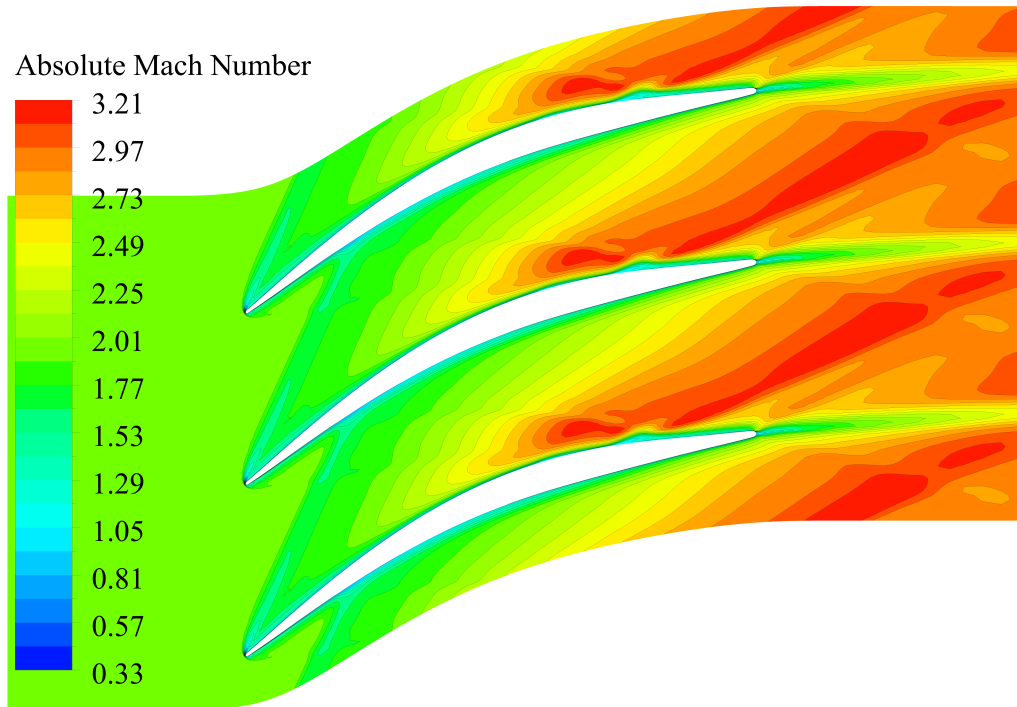


Figure 4.37: Optimised Blade Mid-Span Absolute Mach Number Contours at Design Point

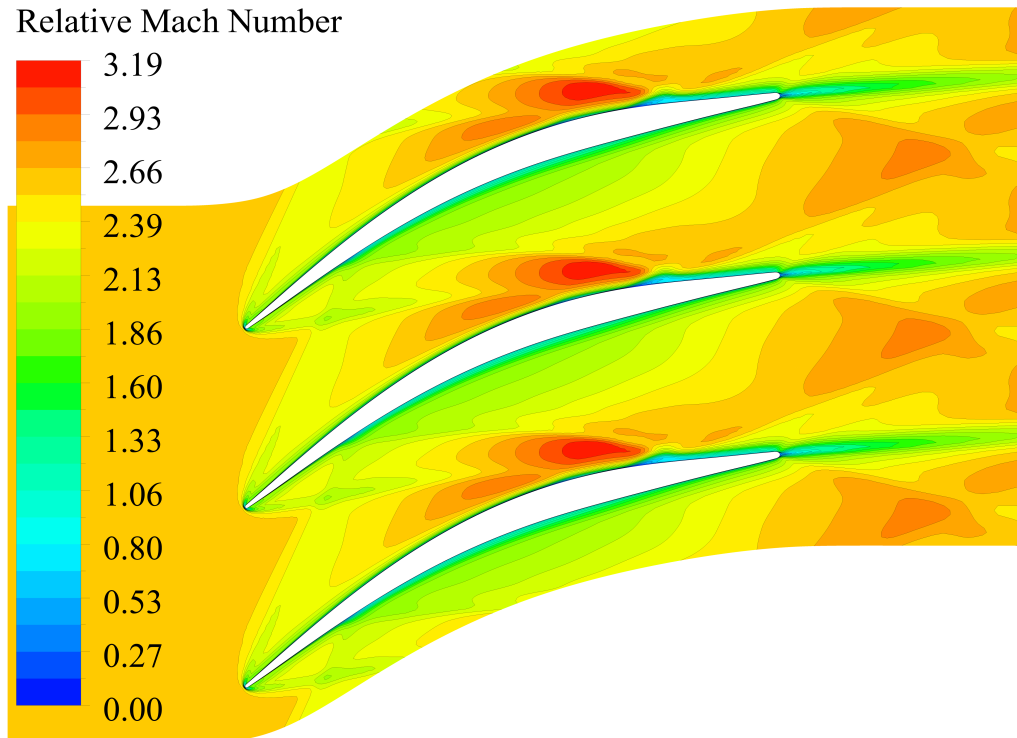


Figure 4.38: Optimised Blade Mid-Span Relative Mach Number Contours at Design Point

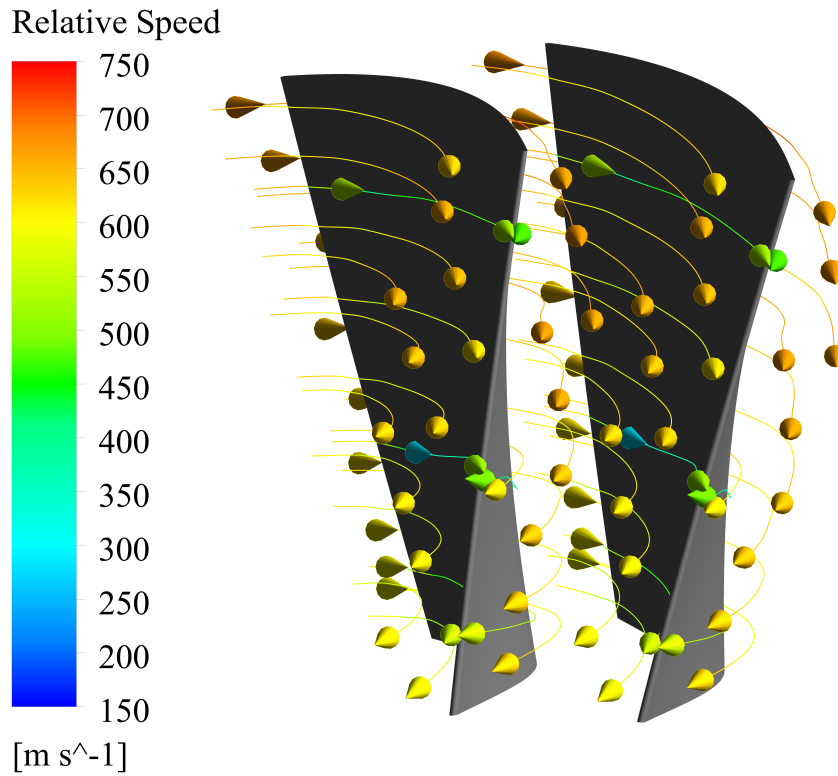


Figure 4.39: Original Blade Trailing Edge Streamlines

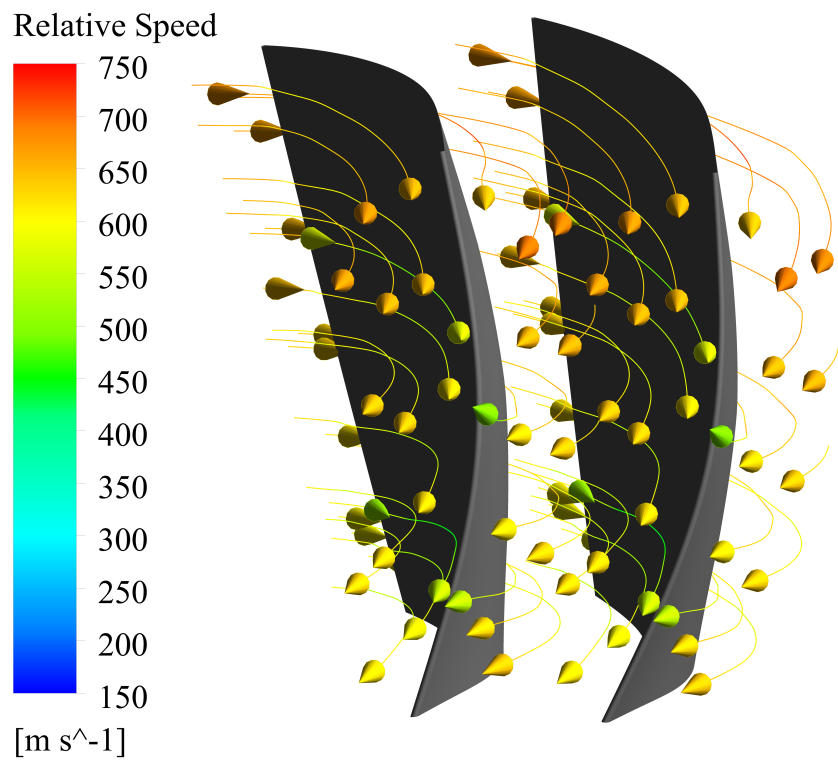


Figure 4.40: Optimised Blade Trailing Edge Streamlines

higher work done on it. The higher work transmission can also be seen in the blade loading charts (Figure 4.41 to 4.43). It is evident how the blade loading of the optimised blade is higher in whatever layer even if it could probably be still improved in the leading edge zone were, except in the tip section, the loading is next to zero due to the blade symmetry in that zone. The higher total pressure ratio showed by the optimised blade is a direct consequence of the higher amount of work done on the flow.

The primary design point losses are represented by the bow shock and by the skin friction. Since the bow shock structure is the same between the two blades, no substantial difference in the bow shock losses is present. On the other hand, skin friction losses depend mainly by the relative Mach number and by the blade solidity. The optimised blade presents a lower blade solidity. A higher blade solidity corresponds to a more extended total blade surface and therefore to higher skin friction losses. Reducing the solidity also causes a progressive increase in the interaction between the reflected bow shock and the boundary layer of the adjacent blade suction surface (Figures 4.37 and 4.38). Hence, the reduction of blade solidity results beneficial until a certain level, below which the effect is disadvantageous. The final result is a higher isentropic efficiency for the optimised blade.

4.4 Summary

The original blade model was validated with success by matching satisfactorily the CFD results with the experimental data for all the possible operating modes. At the design point, the rotor model showed a total pressure ratio of 2.48 and an isentropic efficiency of 77.3%. In such conditions, the shockwaves were contained in the blade passage resulting in little interaction with the adjacent blades suction surfaces. During both impulse-type or subsonic through-flow operating mode, the maximum inlet mass flow is determined by the cross-sectional area of the choking plane, usually located at the blade passage throat.

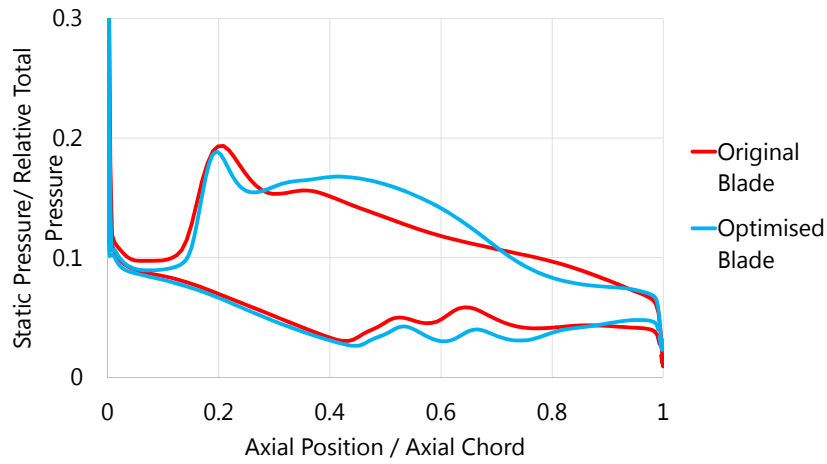


Figure 4.41: Optimised Blade Loading at Design Point (Hub)

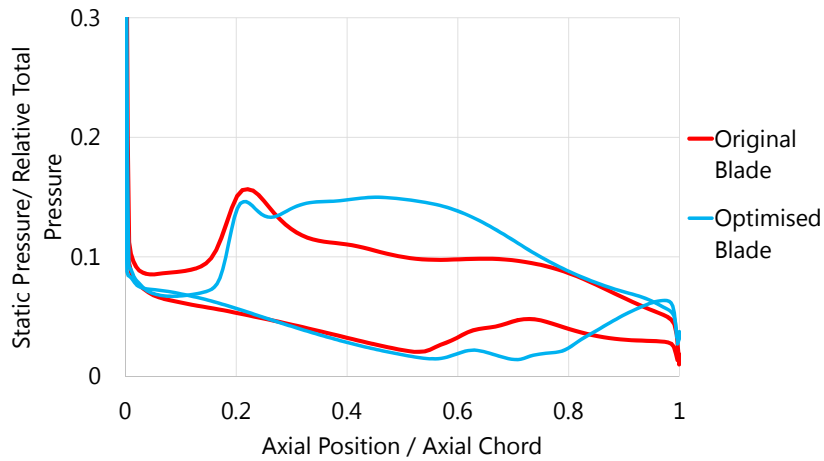


Figure 4.42: Optimised Blade Loading at Design Point (Mid)

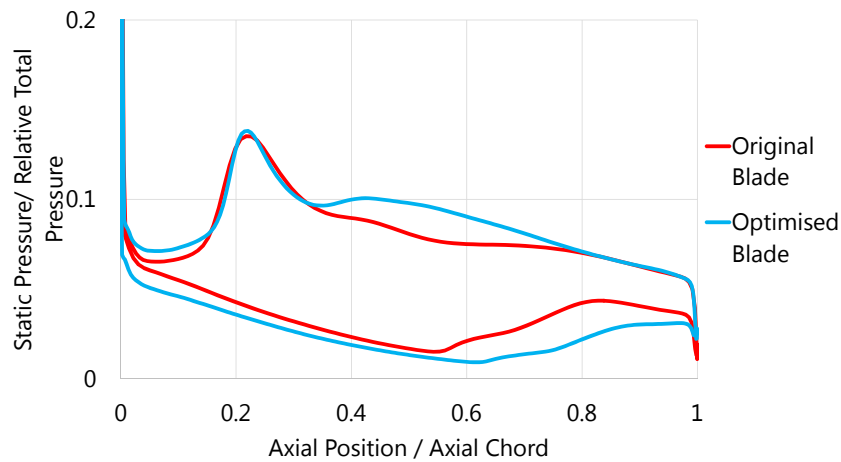


Figure 4.43: Optimised Blade Loading at Design Point (Tip)

Such plane moves to the leading edge front line as soon as the unique-incidence condition is established. Unique-incidence condition occurs in the whole blade for rotational speed equal to 75% or above. During supersonic through-flow operating mode, the maximum inlet mass flow is determined by the strength of the leading edge bow shock. The turbulence model dependency study showed that almost no difference is present between the different turbulence models. Hence, the Standard $k - \omega$ turbulence model was used during the optimisation process due to its low computational cost.

A response surface with a satisfactory prediction quality was firstly produced and was then used for generating the optimised blade geometry. The general behaviour of the optimised blade is qualitatively the same as the original one with almost no difference in performance during the subsonic operating mode. During such mode, the only difference stands in the inlet mass flow due to the geometry differences. For the same reason, a performance difference is instead present in both the impulse-type and the supersonic through-flow operating modes due to the higher flow turning, the higher blade loading and the lower blade solidity.

Chapter 5

Conclusions

The supersonic through-flow rotor previously tested by NASA was modelled for CFD study purposes. The blade was designed by setting the blade angle and thickness distributions. The model was discretised in five layers along the blade span. Only three layers, namely at 0%, 50% and 100% of the blade span, were adjustable in terms of blade angle and thickness distributions. The full model was obtained via the interpolation of the distributions at such stations. Thanks to the available experimental data, the model was satisfactorily validated for both axial subsonic and axial supersonic operating modes. Both a mesh and turbulence model dependency study were carried out in order to ensure that the results were not affected by elements not related to the flow characteristics. The mesh quality was also checked. The fluid domain was created in order to make possible the evaluations of total pressure and total temperature at the corresponding experimental rakes locations so that a direct comparison with the experimental data was possible.

At the design point, the rotor model showed a total pressure ratio of 2.48 and an isentropic efficiency of 77.3%. In such conditions, the shockwaves were contained in the blade passage resulting in little interaction with the adjacent blades suction surfaces. The most critical off-design operating point, from a pure aerodynamic point of view, is represented by the rotor axial supersonic inflow starting. That occurs by increasing the axial inflow Mach number when the blade is in unique-incidence condition. Unique-

incidence condition is established when a supersonic relative flow is present, causing the birth of shock waves or expansion waves that force the flow to enter the blade passage with only one possible incidence, namely the unique incidence. Such condition, in the case of the original blade design, occurs in the whole blade for rotational speed equal to 75% or above. Nasa experimentally observed minor discontinuities in the rotor performances when the supersonic starting process was executed for rotational speeds above 75%.

The design point aerodynamic performance of the supersonic through-flow rotor were enhanced by modifying the blade angle and thickness distributions. The optimisation method used a combination of response surface evaluations and genetic algorithms. A response surface with a satisfactory prediction quality was firstly produced and was then used for generating the Pareto front of possible better designs in terms of isentropic efficiency and total pressure ratio. Since no difference was noticed between the turbulence models used during the model validation, the optimisation process was carried out by using the one with the less computational cost, namely the standard $k - \omega$ model.

The optimised blade showed a wider blade passage and a slightly larger cascade front area. The subsonic behaviour of the optimised blade is qualitatively the same as the original one with almost no difference in performance. The only difference is visible when choking occurs since the optimised blade choked performance corresponds to the original blade one but at a 10% higher rotational speed. Such characteristic is associated to the larger throat area showed by the optimised blade. The difference almost vanishes when unique-incidence condition is established due to the dependency of the amount of inlet mass flow from the leading edges front area rather than from the blade passage throat area. The same behaviour is showed during impulse-type mode since the limiting mass flow mechanisms are the same as the subsonic one. No mass flow difference is evident at supersonic through-flow mode since the limiting mechanisms depends on the strength of the leading edge bow shocks which are the same for both the blades. A performance difference is instead present in both the impulse-type and the supersonic through-flow operating modes. Such difference increases while approaching the design point conditions.

The particular blade geometry allows a higher flow turning, a higher blade loading and a lower blade solidity resulting therefore in a higher total pressure ratio and a higher isentropic efficiency. At design point condition the blade showed an isentropic efficiency of 78.8% and a total pressure ratio of 3.03.

5.1 Future Work

Future aerodynamic blade design improvements should focus on the increase of isentropic efficiency and so aim to a reduction of the two main loss sources: the bow shock and the skin friction. A beneficial effect would be obtained by changing the design point conditions at a lower axial inflow Mach number, depending on the propulsion system requirements. For instance, the implementation of a convergent annulus could be one of the possible solutions. For a fixed rotational speed, the bow shock strength depends mainly on the leading edge bluntness. An eventual blade scaling process would result in a full scaled blade, except for the leading edge whose only requirement is to resist to foreign object damage. Therefore, the blade would be scaled by a fixed factor, while the leading edges would be partially scaled resulting therefore in a lower bow shock influence on the isentropic efficiency. Skin friction can be reduced by implementing surface riblets on the blades, as shown by the study of Ninnemann [38].

Only the blade aerodynamic aspects have been considered in this study. Hence, a blade stress analysis is suggested in order to prevent both the blade failing and a too short blade lifespan. The large rotational speed typical of the analysed supersonic through-flow rotor corresponds also to a big and heavy disk. The reduction in rotational speed would be beneficial both concerning blade stresses and disk weight. The choice of a design point rotational speed over another depends on the propulsion system constrains. Therefore, a preliminary performance study of a whole engine equipped with the supersonic through-flow rotor could be carried out by using the generated performance maps. Such a study would not only answer to such questions but would also show the eventual advantages of

using such rotor rather than other more conventional configurations.

References

- [1] Lowrie, B.W., Terence, J. (1991) *Tandem Fan Engine*, ROLLS ROYCE PLC (GB). Patent Number: EP0426500. Available at: <http://www.freepatentsonline.com/EP0426500.html> (Accessed: 23 June 2018)
- [2] Plencner, R.M. and Snyder, C.A (1991) *The Navy/ NASA Engine Program (NNEP89): A Users Manual*. NASA TM-105186. Available at: <https://ntrs.nasa.gov/archive/nasa/casi.ntrs.nasa.gov/19910020827.pdf> (Accessed: 10 May 2018)
- [3] Franciscus, L.C., Maldonado, J.J. (1989) *Supersonic Through-Flow Fan Engine and Aircraft Mission Performance*. NASA-TM-102304. Available at: <https://ntrs.nasa.gov/archive/nasa/casi.ntrs.nasa.gov/19900011722.pdf> (Accessed: 11 April 2018)
- [4] Chesnakas, C.J. (1991) *Experimental Studies in a Supersonic Through-Flow Fan Blade Cascade*. PhD Thesis in Mechanical Engineering. Virginia Polytechnic Institute.
- [5] Stanford University (2015) *Propulsion Systems: Basic Concepts*. Available at: <https://archive.is/huOKu> (Accessed: 12 June 2018)
- [6] Howlett, R.A. (1976) 'Variable stream control engine concept for advanced supersonic aircraft: Features and benefits', *The SCAR Conference*. Hampton, Virginia, USA, 9-12 November. Hampton: NASA, Part 1, pp. 341-352

-
- [7] Tweedt, D.L. (1993) *The aerodynamics of a baseline supersonic throughflow fan rotor*. PhD Thesis in Mechanical Engineering. Iowa State University.
- [8] Franciscus, L.C. (1978) *Supersonic through-flow fan engines for supersonic cruise aircraft*. NASA-TM-78889. Available at: <https://ntrs.nasa.gov/archive/nasa/casi.ntrs.nasa.gov/19780015145.pdf> (Accessed: 14 April 2018)
- [9] Berton, J.J., Haller, W.J., Senick, P.F., Jones, S.M., Seidel, J.A. (2005) *A Comparative Propulsion System Analysis for the High-Speed Civil Transport*. NASA-TM-2005-213414. Available at: <https://ntrs.nasa.gov/archive/nasa/casi.ntrs.nasa.gov/20050123580.pdf> (Accessed: 15 April 2018)
- [10] Tran, D.H. (2004) *Parametric Study of a Mach 2.4 Transport Engine with Supersonic Through-Flow Rotor and Supersonic Counter-Rotating Diffuser (SSTR/SSCRD)*. NASA-TM-2004-213139. Available at: <https://ntrs.nasa.gov/archive/nasa/casi.ntrs.nasa.gov/20040087141.pdf> (Accessed: 15 April 2018)
- [11] Ferri, A. (1956) 'Problems related to matching turbojet engine requirements to inlet performances as function of flight Mach number and angle of attack', in Fabri, J. (ed.) *Air intake problems in supersonic propulsion*, AGARDograph No.27. Chatillon-sous-Bagneux: AGARD, pp. 48-61.
- [12] Trucco, H. (1975) *Study of Variable Cycle Engines Equipped With Supersonic Fans*. NASA-CR-134777. United States: NASA.
- [13] Wilcox, W.W., Tysl, E.R., Hartmann, M.J. (1959) 'Resume of the Supersonic-Compressor Research at NACA Lewis Laboratory', *Journal of Basic Engineering*, Vol. 81, pp. 559-568

-
- [14] Breugelmans, F.A.E. (1975) 'The Supersonic Axial Inlet Component in a Compressor', *ASME 1975 International Gas Turbine Conference and Products Show*. Houston, Texas, USA, 26 March. Houston: ASME, Vol. 1A, pp. 1-8
- [15] Schmidt, J.F., Moore, R.D., Wood, J.R. and Steinke, R.J. (1987) *Supersonic Through-Flow Fan Design*. NASA-TM-88908. Available at: <https://ntrs.nasa.gov/archive/nasa/casi.ntrs.nasa.gov/19870013248.pdf> (Accessed: 15 November 2017)
- [16] Urasek, D.C., Cunnan, W.S., Lantz, R.L., Richard, L., Fronek, D.L., Dawson, R.A. and Brown, J.C. (1990) *Supersonic Throughflow Fan Test Facility at NASA Lewis Research Center*. NASA TP-3038.
- [17] Moore, R.D., Schmidt, J.F. and Tweedt, D.L. (1993) *Aerodynamic Performance of a Supersonic Throughflow Fan Stage*. NASA TP-3308.
- [18] Wood, J.R., Schmidt, J.F., James, F., Steinke, R.J., Chima, R.V. and Kunik, W.G. (1987) *Application of Advanced Computational Codes in the Design of an Experiment for a Supersonic Throughflow Fan Rotor*. NASA TM-88915. Available at: <https://ntrs.nasa.gov/archive/nasa/casi.ntrs.nasa.gov/19870013197.pdf> (Accessed: 2 May 2018)
- [19] Fronek, D.L., Setter, R.N., Blumenthal, P.Z. and Smalley, R.R. (1987) *A Distributed Data Acquisition System for Aeronautics Test Facilities*. NASA TM-88961. Available at: <https://ntrs.nasa.gov/archive/nasa/casi.ntrs.nasa.gov/19870007418.pdf> (Accessed: 4 May 2018)
- [20] Hield, P. M. (1993) *The application of a supersonic through-flow fan to supersonic civil transport*. MSc Thesis in Mechanical Engineering. Cranfield University.
- [21] Starcken, H., Zhong, Y. and Schreiber, H.A. (1984) 'Mass Flow Limitation of Supersonic Blade Rows due to Leading Edge Blockage', *ASME 1984 International Gas*

- Turbine Conference and Exhibit*. Amsterdam, Netherlands, 47 June. Amsterdam: ASME, Vol. 1, Paper number: 84-GT-233, pp. 1-7
- [22] Lichtfub, H.J. and Starke, H. (1974) 'Supersonic Cascade Flow', in Kuchemann, D. (ed.) *Progress in Aerospace Science*, Vol. 15. New York: Pergamon Press Ltd, pp. 37-149.
- [23] Moore, R.D. and Tweedt, D.L. (1991) *Aerodynamic Performance of a Supersonic Throughflow Fan Rotor*. NASA TP-3115.
- [24] Teixeira, J. A. (2018), 'Grid Generation for Turbomachinery' [PowerPoint Presentation], *Introduction to CFD for Gas Turbines*. Cranfield University. Available at: <https://bb.cranfield.ac.uk/> (Accessed: 2 April 2018)
- [25] ANSYS[®] (2017) *ANSYS BladeGen User's Guide*. ANSYS Inc. Canonsburg.
- [26] ANSYS[®] (2016), 'Module 5: Mesh Quality & Advanced Topics' [PowerPoint Presentation], *Introduction to ANSYS Meshing*. ANSYS Inc. Available at: <https://bb.cranfield.ac.uk/> (Accessed: 20 May 2018)
- [27] ANSYS[®] (2017) *ANSYS Fluent Theory Guide*. ANSYS Inc. Canonsburg.
- [28] ANSYS[®] (2017) *ANSYS CFX-Solver Modeling Guide*. ANSYS Inc. Canonsburg.
- [29] CFD Online (2015) *Best practice guidelines for turbomachinery CFD*. Available at: https://www.cfd-online.com/Wiki/Best_practice_guidelines_for_turbomachinery_CFD (Accessed: 20 May 2018).
- [30] ANSYS[®] (2017) *ANSYS Turbogrid User's Guide*. ANSYS Inc. Canonsburg.
- [31] ANSYS[®] (2017) *ANSYS CFX-Pre User's Guide*. ANSYS Inc. Canonsburg.
- [32] Box, G.E.P. and Draper, N.R. (1987) *Empirical model-building and response surfaces*. New York: John Wiley & Sons.

- [33] Myers, R.H. and Montgomery, D.C. (1995) *Response surface methodology: process and product optimization using design of experiments*. New York: John Wiley & Sons.
- [34] ANSYS[®] (2017) *ANSYS DesignXplorer User's Guide*. ANSYS Inc. Canonsburg.
- [35] Alvarez, L. (2000) *Design Optimization based on Genetic Programming*. PhD Thesis in Civil Engineering. University of Bradford.
- [36] Holland, J.A. (1975) *Adaptation in natural and artificial systems*. Ann Arbor: University of Michigan.
- [37] Li, Y. (2017) 'Gas Turbine Diagnostics', *Gas Turbine Performance, Simulation and Diagnostic*. Cranfield University. Available at: <https://bb.cranfield.ac.uk/> (Accessed: 27 November 2017).
- [38] Ninnemann, T.A. (1994) *Effects of Riblets on the Performance of the Supersonic Through-flow Fan Cascade Blades*. PhD Thesis in Mechanical Engineering. Virginia Polytechnic Institute.
- [39] Pastrone, D. (2017), 'Subsonic Air Intakes' [PowerPoint Presentation], *Jet Propulsion*. Politecnico di Torino. Available at: <https://www.polito.it/intranet/> (Accessed: 7 May 2018)
- [40] Pastrone, D. (2017), 'External-Compression Supersonic Intakes' [PowerPoint Presentation], *Jet Propulsion*. Politecnico di Torino. Available at: <https://www.polito.it/intranet/> (Accessed: 7 May 2018)

Appendix A

Gas Turbine Performance Aspects

A.1 Specific Thrust Considerations for Supersonic Flight

For a general propulsion device, standard net thrust is defined as the difference between the exhaust stream force and the free stream one. The stream force can be defined as:

$$SF = WV + A(P - P_0); \quad (\text{A.1})$$

In other words, for a given flow section, it is defined as the mass flow multiplied by the velocity of the flow passing through the section plus the area of the section multiplied by the difference between the static pressure of the flow passing through the section and the static pressure of the undisturbed upstream flow (ambient static pressure). Before proceeding, a definition of mass flow is necessary. Considering a fluid passing through a certain section, the mass flow is defined as the product between the fluid density, the fluid velocity and the area of the section crossed:

$$W = \rho VA; \quad (\text{A.2})$$

It is possible to indicate with 0 the free stream section, with i the inlet section and with j the exhaust one (considering a single exhaust), as shown in Figure [A.1](#). Considering such

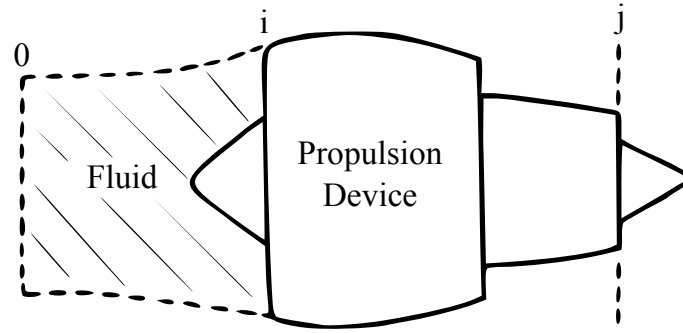


Figure A.1: Free stream, inlet and exhaust engine section locations [39, pp.26].

convention, as stated before, standard net thrust can be defined as the difference between the exhaust stream force and the free stream one:

$$F = SF_j - SF_0 = W_j V_j + A_j (P_j - P_0) - W_0 V_0; \quad (\text{A.3})$$

For a fully expanded nozzle, defined as a case in which the nozzle flow is expanded until its static pressure is the same as the external ambient one ($P_j = P_0$), thrust definition can be simplified as follows:

$$F = W_j V_j - W_0 V_0; \quad (\text{A.4})$$

Specific thrust is defined as the ratio between the thrust and the inlet mass flow:

$$SF = \frac{F}{W_0}; \quad (\text{A.5})$$

The exhaust mass flow can be defined as the sum between the inlet mass flow and the fuel flow. By introducing the fuel-to-air ratio (FAR) it is possible to define the exhaust mass flow as follows:

$$W_j = W_0 + W_f = \left(1 + \frac{W_f}{W_0}\right) W_0 = (1 + FAR) W_0; \quad (\text{A.6})$$

Therefore, an alternative expression for the specific thrust is shown below:

$$SF = \frac{W_j V_j - W_0 V_0}{W_0} = (1 + FAR) V_j - V_0; \quad (\text{A.7})$$

For a fixed thrust level, a higher specific thrust corresponds to a lower inlet mass flow (Eq. [A.5](#)). If the inlet flow speed and density are assumed constant, a lower inlet mass flow corresponds in turn to a lower inlet cross-sectional area (Eq. [A.2](#)). Therefore, during the supersonic flight, a high specific thrust is desirable since it corresponds to a smaller engine cross-sectional area and consequently to a lower aircraft drag. However, for a fixed inlet mass flow and flight speed, a higher specific thrust corresponds to a higher jet velocity (Eq. [A.7](#)) and therefore to a higher jet noise.

A.2 Spillage Drag for External-Compression Supersonic Intakes

During cruise mode, the spillage drag is defined as the difference between the inlet stream force and the free stream one (stations shown in Figure [A.1](#)):

$$D = SF_i - SF_0; \tag{A.8}$$

When an external reversible compression occurs because of the air intake, condition present during subsonic flight, the spillage drag can be considered as a positive contribution to the production of thrust. This is proven by the fact that, in such conditions, the air flow is able to create a suction force on the external intake fairing, as shown in Figure [A.2](#). It is important also to notice how the air inside the inlet contributes positively to the production of thrust thanks to its increase of static pressure due to the diffusion process.

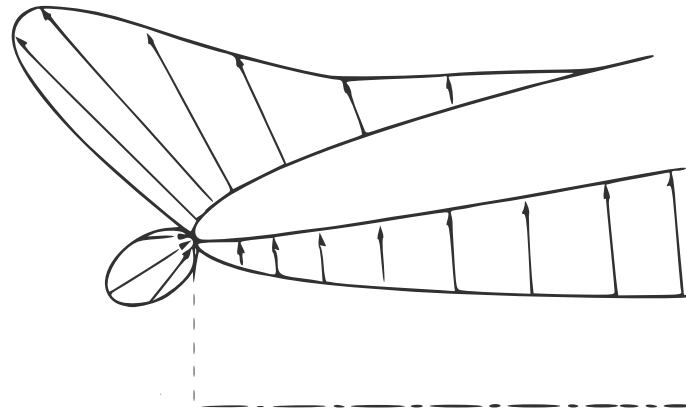


Figure A.2: Pressure distribution around an air intake edge [39, pp.3].

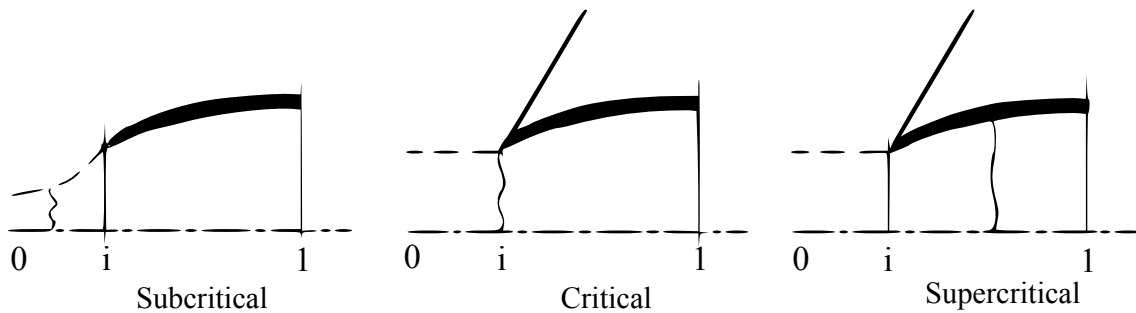


Figure A.3: Subcritical, critical and supercritical conditions [40, pp.15].

During supersonic flight, part of the compression occurs via a shock wave, which is an irreversible phenomenon, hence the spillage drag has to be accounted as a loss. It is possible to categorise the supersonic intake flow in three possible cases, as shown in Figure A.3: subcritical, critical and supercritical.

The subcritical condition is defined as a configuration in which a shockwave occurs before the intake inlet. Due to the subsonic condition of the flow after the shockwave, the intake influences the air characteristics causing an increase of its static pressure before entering in the intake itself. This process creates a difference between the free stream and the inlet stream forces, causing the production of spillage drag which now is not recoverable. The supercritical condition is defined as a configuration in which the shock wave occurs after the intake inlet. Since no subsonic conditions are present before the inlet, this configuration permits to avoid the production of spillage drag. However, due to the shockwave position, not all the air inside the intake is subject to an increase of

static pressure and part of the thrust is therefore lost. Finally, the critical condition is defined as a configuration in which the shock wave is positioned exactly at the intake inlet, resulting in the absence of spillage drag and an efficient thrust production. The best case is represented by the critical one which is also considered the on-design one. The mass flow passing through the station 1 can be expressed as follows:

$$W_1 = \frac{A_1 P_1^o}{\sqrt{RT_1^o}} \sqrt{\frac{\gamma M_1^2}{\left(1 + \frac{\gamma-1}{2} M_1^2\right)^{\frac{\gamma+1}{\gamma-1}}}} = \frac{A_1 P_1^o}{\sqrt{RT_1^o}} f(M_1); \quad (\text{A.9})$$

From Equation [A.9](#) can be seen that, for a fixed geometry and an adiabatic flux, the function of the Mach number is proportional to the ratio between the mass flow and the total pressure.

$$f(M_1) \propto \frac{W_1}{P_1^o}; \quad (\text{A.10})$$

When an engine is in part power conditions, the value of M_1 is reduced causing a reduction of the Mach function $f(M_1)$. Such reduction corresponds to a lower mass flow at the station 1 (W_1), which in turn causes the mass flow at the inlet to reduce due to the mass flow conservation law. Starting from a critical case, a reduction in inlet mass flow is possible only by moving the shockwave outside of the air intake. In other words, an engine part power condition causes the configuration to go from critical to subcritical leading to the production of spillage drag.

Appendix B

Settings Tables and Charts

B.1 Domain Definition

The domain has been created by using linear segments. The zero-reference locations are the blade leading edge for the horizontal position and the compressor centre of rotation for the vertical one. Considering that the internal and external compressor radii are respectively 7 and 10 inches, the domain hub is located at a vertical position of 7 inches, while the domain shroud is located at a vertical position of 10 inches. The positions of the discretisation points are listed in Table [B.1](#).

Table B.1: Domain Points Locations

Hub		Shroud	
Horizontal [mm]	Vertical [mm]	Horizontal [mm]	Vertical [mm]
-152.0	177.80	-152.0	254.0
0.0	177.80	0.0	254.0
90.42	177.80	96.80	254.0
250.0	177.80	250.0	254.0

B.2 Original Blade Model

Since the purpose of this document is not to describe obsolete blade models which are not useful for CFD analysis, only the final validated geometry is here presented. The general software settings are reported in Table B.2. Data and plots relative to thickness and blade angle distributions are here reported, from Table B.3 to Table B.14 and from Figure B.1 to Figure B.6. As described in the specific section, the distributions are relative to the hub, mean and tip layers of the blade model. For both the distributions, in the x-axis the layer chord location in terms of percentage is reported, where 0% corresponds to the leading edge section while 100% corresponds to the trailing edge one for that particular layer.

Table B.2: General Blade Model Settings

Property	Description
Machine Type	Axial Compressor
Component Type	Rotor
Mode	Angle/Thickness
Rotation Type	Negative
Units	mm
Number of Blades	44
Number of Blade Points	60
Number of Leading Edge Points	9
Number of Trailing Edge Points	9
Hub Leading Edge Ellipse Ratio	1.5
Shroud Leading Edge Ellipse Ratio	1.5
Hub Trailing Edge Ellipse Ratio	1.5
Shroud Trailing Edge Ellipse Ratio	1.5

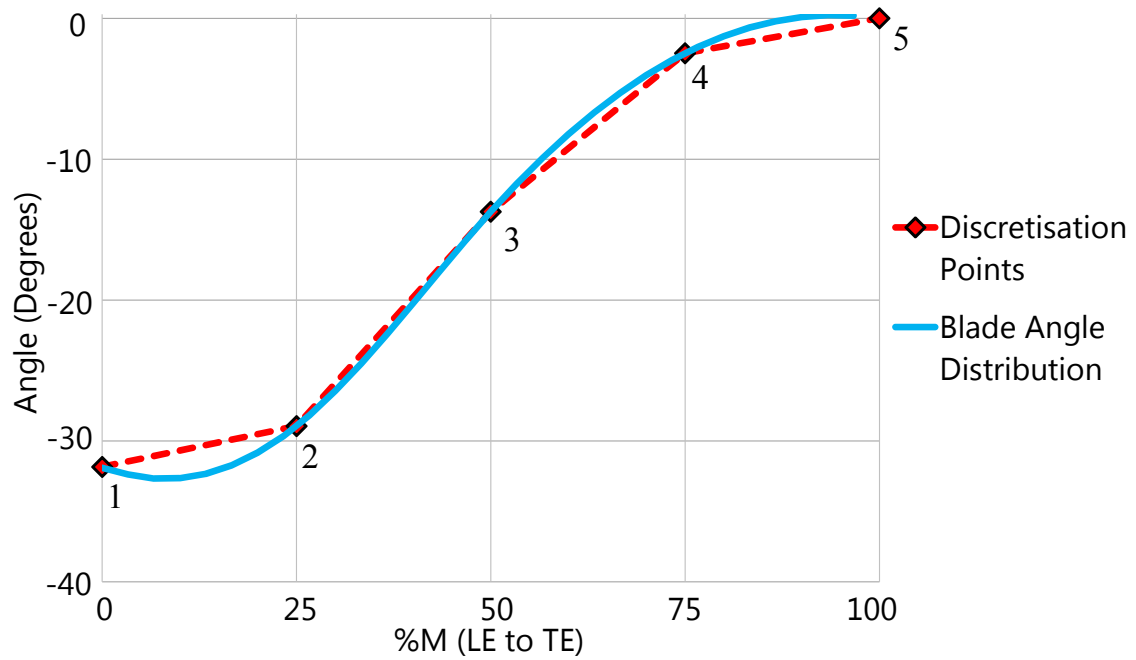


Figure B.1: Original Blade Angle Distribution (Hub)

Table B.3: Angle Distribution Discretisation Points Locations (Hub)

Discretisation Points	x	y
1	0.0	-31.84
2	25.0	-28.95
3	50.0	-13.73
4	75.0	-2.48
5	100.0	0.0

Table B.4: Angle Distribution Properties (Hub)

Property	Description
Layer	0% Span
Distribution	Angle
Curve Type	Cubic Spline

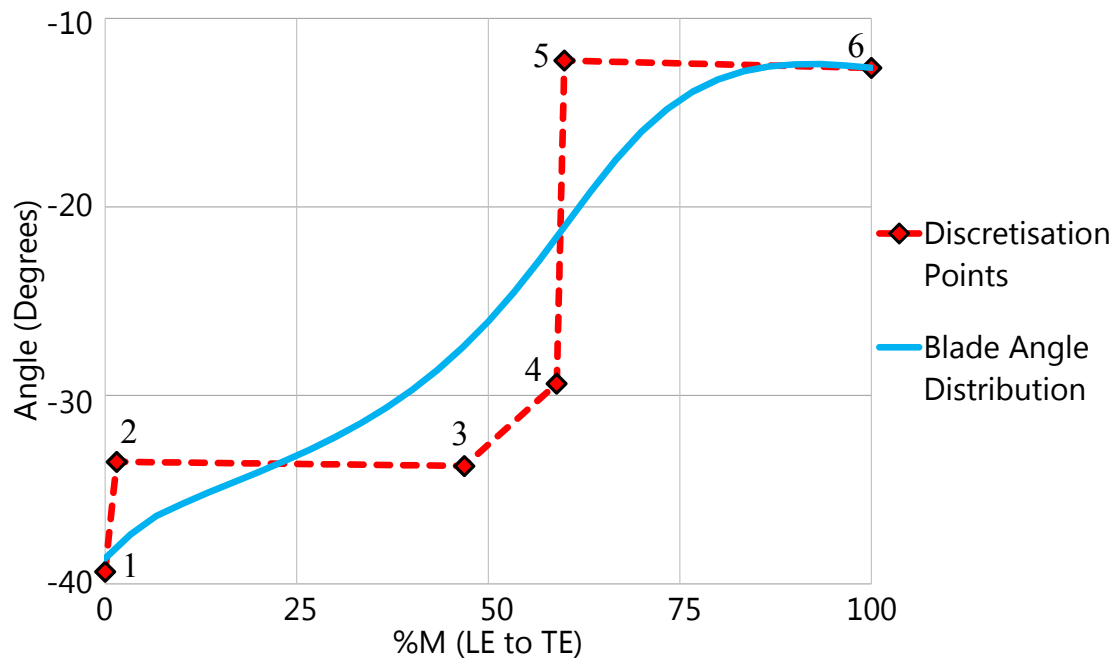


Figure B.2: Original Blade Angle Distribution (Mean)

Table B.5: Original Angle Distribution Discretisation Points Locations (Mean)

Discretisation Points	x	y
1	0.0	-38.13
2	1.52	-32.48
3	46.88	-32.69
4	58.93	-28.46
5	59.93	-11.85
6	100.0	-12.23

Table B.6: Original Angle Distribution Properties (Mean)

Property	Description
Layer	50% Span
Distribution	Angle
Curve Type	Bezier Segment

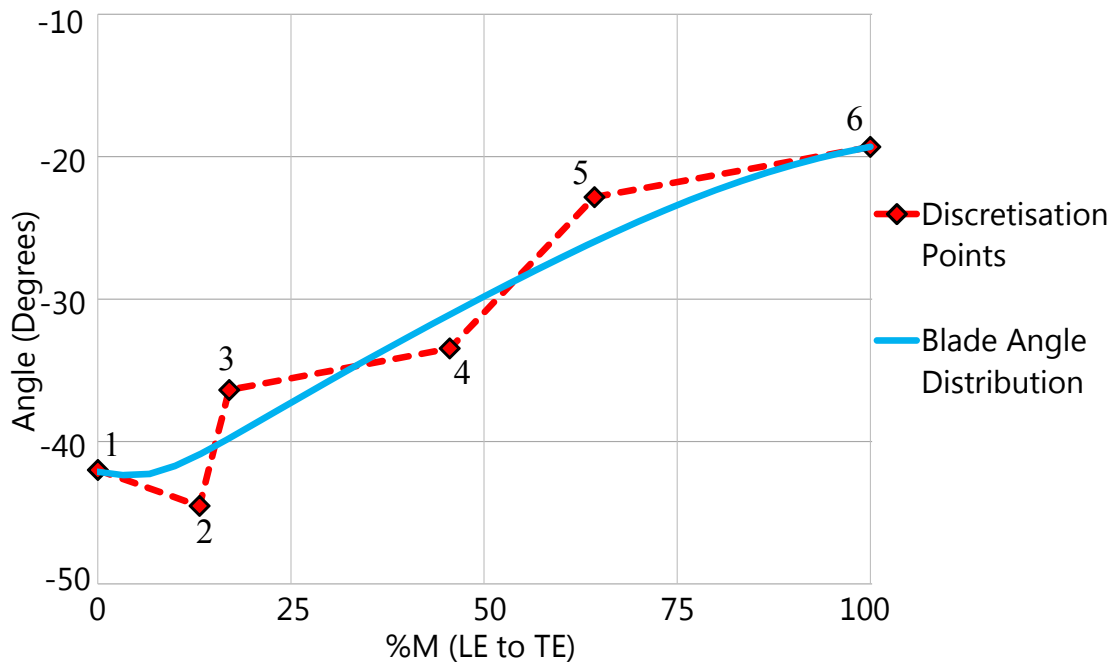


Figure B.3: Original Blade Angle Distribution (Tip)

Table B.7: Original Angle Distribution Discretisation Points Locations (Tip)

Discretisation Points	x	y
1	0.0	-42.0
2	13.17	-44.52
3	17.02	-36.37
4	45.55	-33.46
5	64.28	-22.84
6	100	-19.32

Table B.8: Original Angle Distribution Properties (Tip)

Property	Description
Layer	100% Span
Distribution	Angle
Curve Type	Beizer Segment

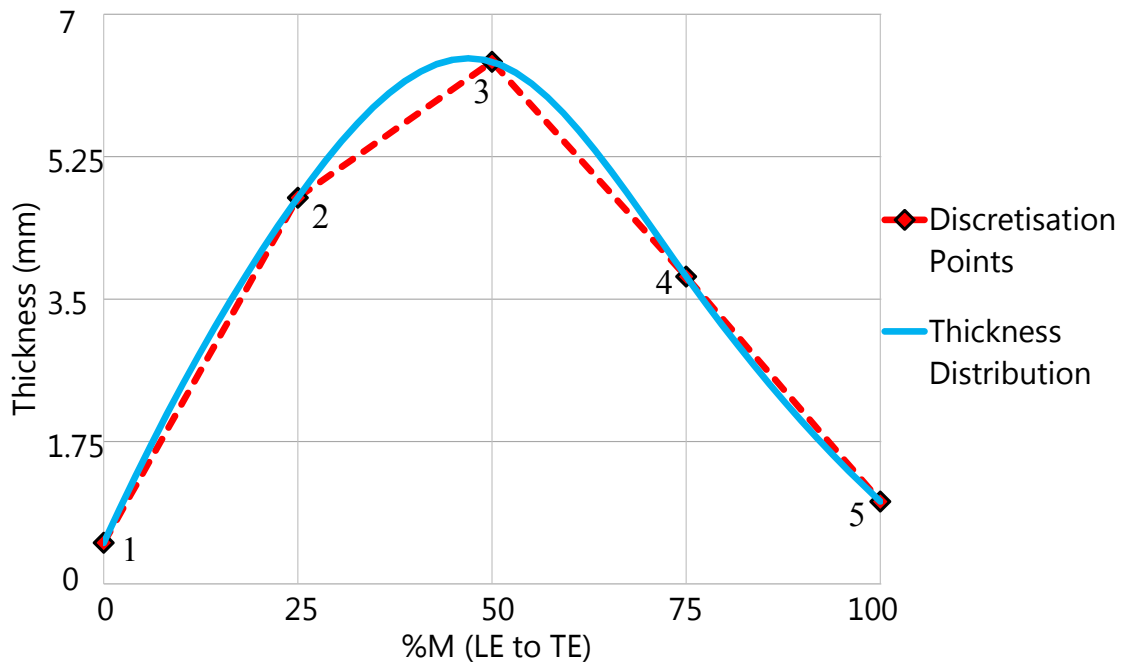


Figure B.4: Original Thickness Distribution (Hub)

Table B.9: Original Thickness Distribution Discretisation Points Locations (Hub)

Discretisation Points	x	y
1	0.0	0.50
2	25	4.74
3	50	6.41
4	75	3.77
5	100	1.01

Table B.10: Original Thickness Distribution Properties (Hub)

Property	Description
Layer	0% Span
Distribution	Thickness
Curve Type	Cubic Spline

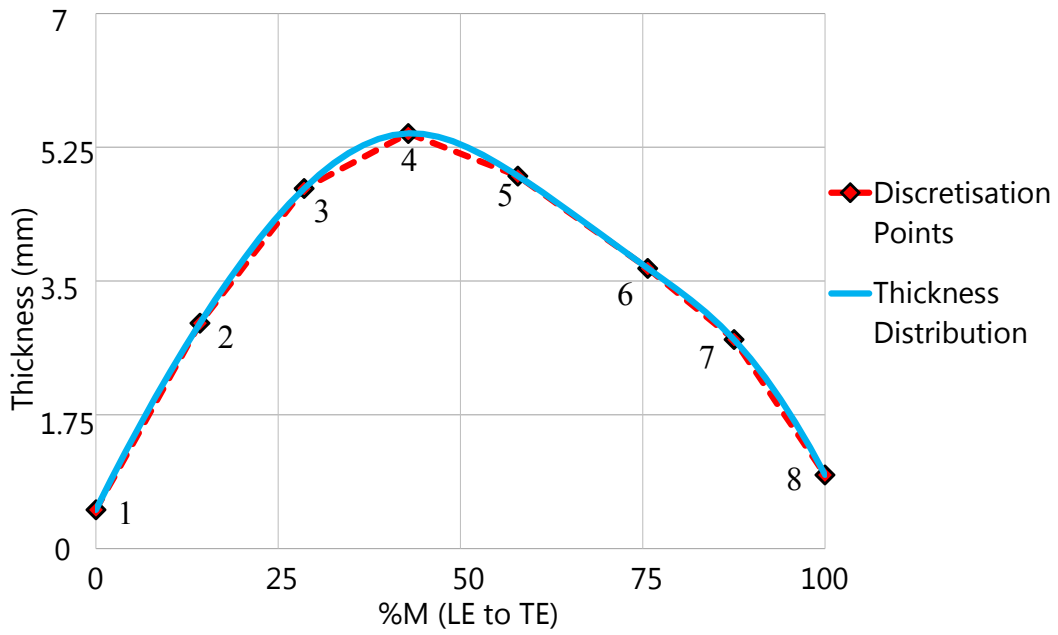


Figure B.5: Original Thickness Distribution (Mean)

Table B.11: Original Thickness Distribution Discretisation Points Locations (Mean)

Discretisation Points	x	y
1	0.0	0.51
2	14.28	2.94
3	28.57	4.71
4	42.85	5.43
5	57.87	4.87
6	75.69	3.66
7	87.52	2.73
8	100.0	0.96

Table B.12: Original Thickness Distribution Properties (Mean)

Property	Description
Layer	50% Span
Distribution	Thickness
Curve Type	Cubic Spline

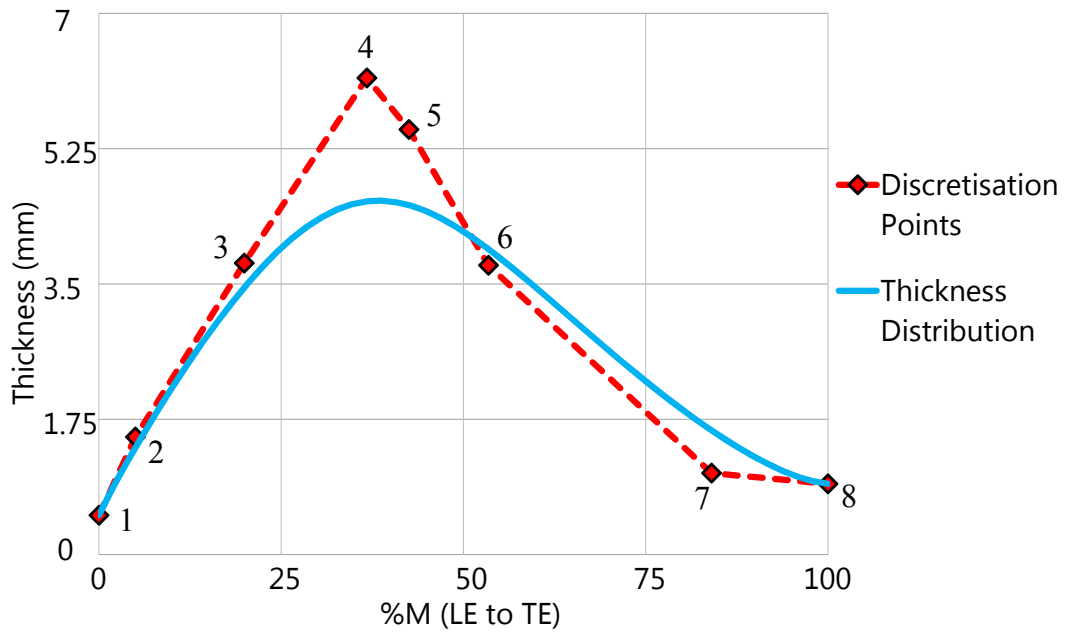


Figure B.6: Original Thickness Distribution (Tip)

Table B.13: Original Thickness Distribution Discretisation Points Locations (Tip)

Discretisation Points	x	y
1	0.0	0.51
2	5.02	1.52
3	19.94	3.77
4	36.76	6.16
5	42.51	5.49
6	53.43	3.74
7	84.03	1.05
8	100.0	0.91

Table B.14: Original Thickness Distribution Properties (Tip)

Property	Description
Layer	100% Span
Distribution	Thickness
Curve Type	Bezier Segment

B.3 Mesh Settings

The final selected mesh type and quality have been discussed in the specific section '*Mesh Design*'. The settings for replicating such mesh are reported in Table [B.15](#). The general requirements already described in the main section, such as a normal expansion ratio ≤ 1.1 and about 70 mesh nodes in the blade passage, has been respected.

Table B.15: Turbogrid Settings

Property	Description
Inlet Passage Mesh Type	H-Grid
Outlet Passage Mesh Type	H-Grid
Blade Passage Mesh Type	O-Grid
First Element Offset	$1.8e^{-7}$ [m]
Global Size Factor	1.375
Expansion Rate	1.1
Passage Number of Elements	80
Inlet Passage Expansion Rate	1.0
Outlet Passage Expansion Rate	1.0

B.4 Boundary Conditions and Solver Settings

The boundary conditions relative to each domain part are reported in Table [B.16](#), while the general domain boundary conditions are reported in Table [B.17](#). Since the whole domain has been set as rotating, the parts which are stationary needs to be set as counter-rotating so that at the end no absolute motion exists. Regarding the rotor subsonic operating mode, the outlet boundary conditions are reported in Table [B.18](#). For each speed line, a static pressure range is shown, where the maximum value corresponds to the imminent surge while the minimum value corresponds to an operating point which lies in the choking line. The impulse-type mode is replicated by merely imposing a very low back static pressure

in order to establish a supersonic outflow. The supersonic operating mode is replicated by setting a supersonic outlet and a specific inlet static pressure, static temperature and normal flow speed in order to replicate the experimental Mach numbers. For the sake of completeness, the solver settings are reported in Table [B.19](#).

Table B.16: Domain Parts Boundary Settings

Domain Part	Boundary Setting
Shroud	Counter Rotating No Slip Smooth Wall
Stationary Hub	Counter Rotating No Slip Smooth Wall
Blade	Rotating No Slip Smooth Wall
Rotating Hub	Rotating No Slip Smooth Wall
Inlet	Stationary Flow Inlet
Outlet	Stationary Flow Outlet
Periodic Interface	Interface

Table B.17: General Domain Settings

Domain Setting	Notes
Domain Type	Fluid
Fluid Material	Air Ideal Gas
Fluid Type	Continuous Fluid
Reference Pressure	0 [atm]
Bouyancy Model	Non Buoyant
Domain Motion	Rotating
Rotation Axis	Global Z

Table B.18: Subsonic Outlet Boundary Settings

Rotational Speed [rev/min]	Static Pressure Range [kPa]
5,156.4 (30%)	84.0 - 102.73
6,875.2 (40%)	84.0 - 103.0
8,594.0 (50%)	84.0 - 104.70
10,312.8 (60%)	84.0 - 105.66
12,891.0 (75%)	84.0 - 107.50

Table B.19: Solver Settings

Property	Description
Turbulence Numerics	High Resolution
Timescale Control	Auto Timescale
Length Scale Option	Conservative
Residual Type	RMS
Timescale Factor	1
Maximum Number of Iterations	1,000
Residual Target	$1e^{-5}$

B.5 Optimised Blade Model

The optimisation process requires a limited amount of design variables. Starting from the original design, a reduction in the number of discretisation points is therefore required. Both the blade angle and thickness characteristics were modified in the number of discretisation points but by maintaining as far as possible the initial distribution equal to the original one. All the distributions are based on Beizer segments. The new points nomenclature and the optimised distributions are reported from Figure [B.7](#) to Figure [B.12](#).

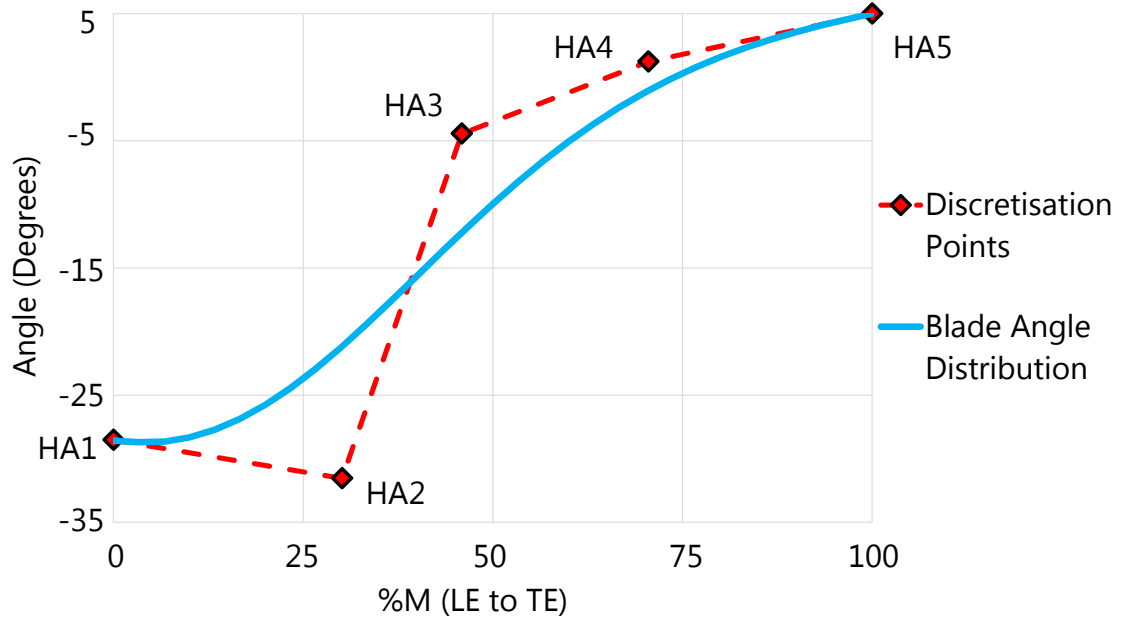


Figure B.7: Optimised Blade Angle Distribution (Hub)

Table B.20: Optimised Angle Distribution Discretisation Points Locations (Hub)

Discretisation Points	x	y
HA1	0.0	-30.46
HA2	30.17	-33.65
HA3	45.94	-5.00
HA4	70.39	0.98
HA5	100.0	4.98

Table B.21: Optimised Angle Distribution Properties (Hub)

Property	Description
Layer	0% Span
Distribution	Angle
Curve Type	Bezier Segment

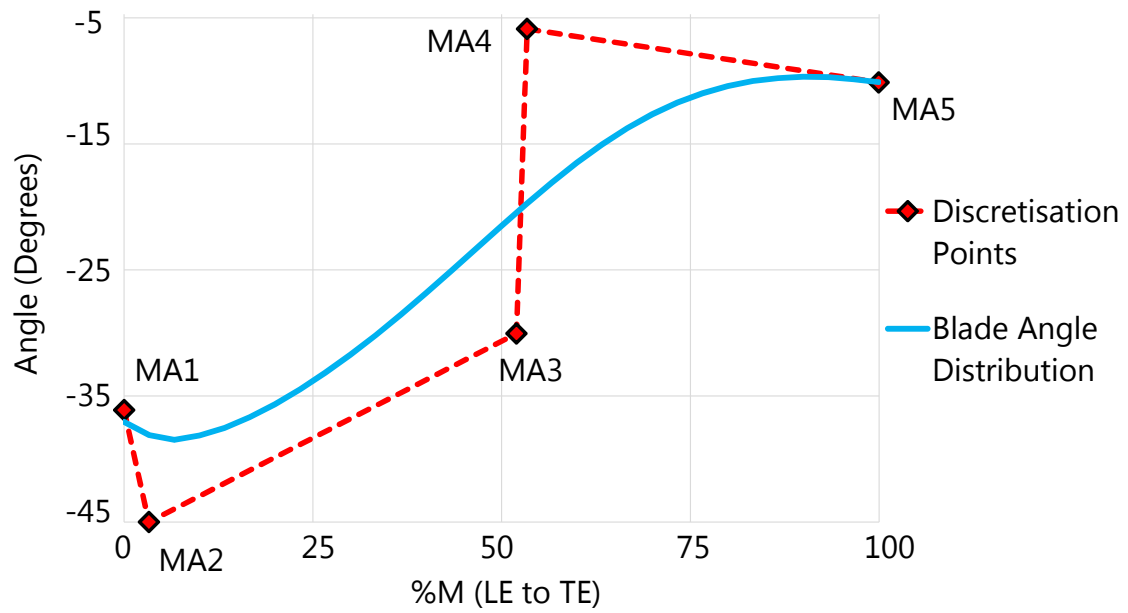


Figure B.8: Optimised Blade Angle Distribution (Mean)

Table B.22: Optimised Angle Distribution Discretisation Points Locations (Mean)

Discretisation Points	x	y
MA1	0.0	-36.06
MA2	3.31	-44.97
MA3	52.07	-29.98
MA4	52.49	-5.75
MA5	100.0	-10.0

Table B.23: Optimised Angle Distribution Properties (Mean)

Property	Description
Layer	50% Span
Distribution	Angle
Curve Type	Bezier Segment

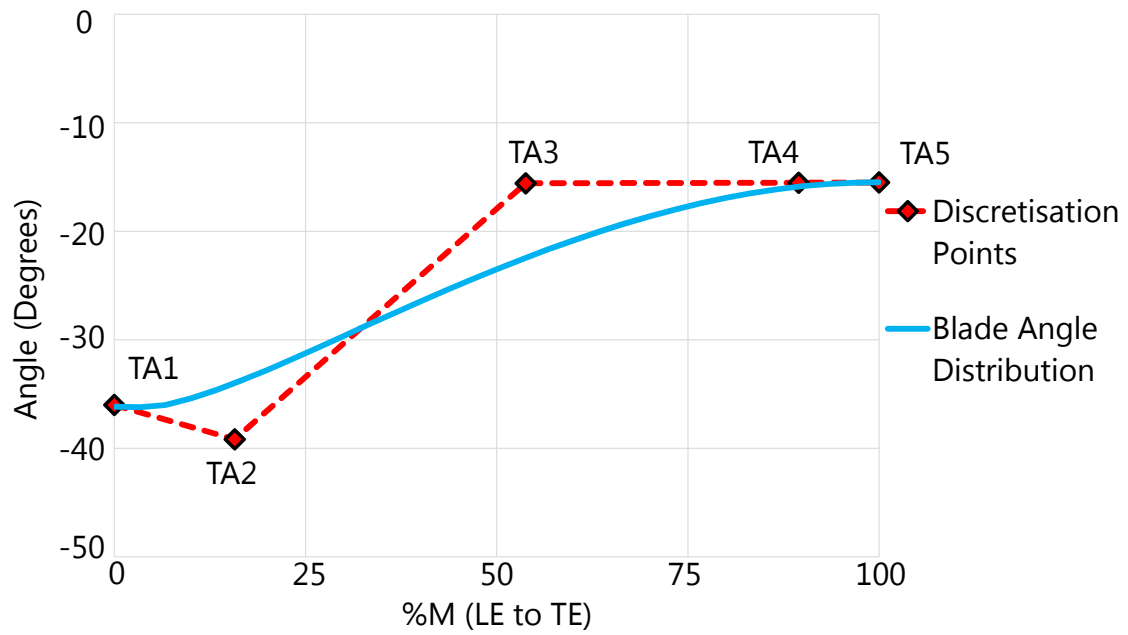


Figure B.9: Optimised Blade Angle Distribution (Tip)

Table B.24: Optimised Angle Distribution Discretisation Points Locations (Tip)

Discretisation Points	x	y
TA1	0.0	-36.75
TA2	15.86	-40.09
TA3	53.88	-15.09
TA4	89.52	-15.03
TA5	100.0	-15.0

Table B.25: Optimised Angle Distribution Properties (Tip)

Property	Description
Layer	100% Span
Distribution	Angle
Curve Type	Bezier Segment

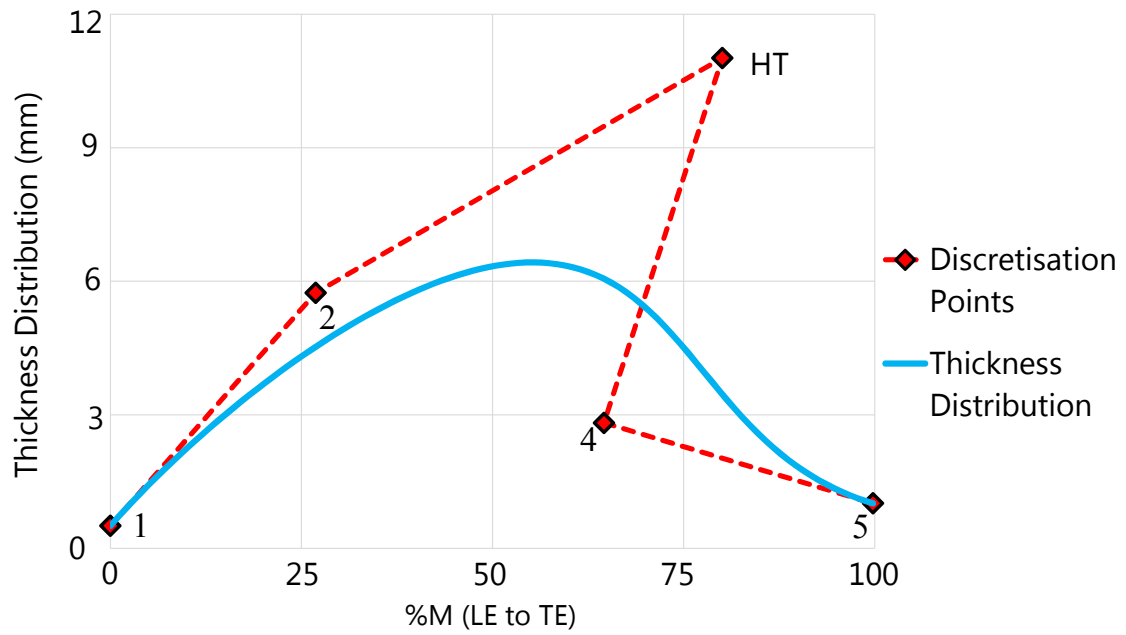


Figure B.10: Optimised Blade Thickness Distribution (Hub)

Table B.26: Optimised Thickness Distribution Discretisation Points Locations (Hub)

Discretisation Points	x	y
1	0.0	0.58
2	26.93	5.74
HT	80.25	11.04
4	64.72	2.82
5	100.0	1.01

Table B.27: Optimised Angle Distribution Properties (Hub)

Property	Description
Layer	0% Span
Distribution	Thickness
Curve Type	Bezier Segment

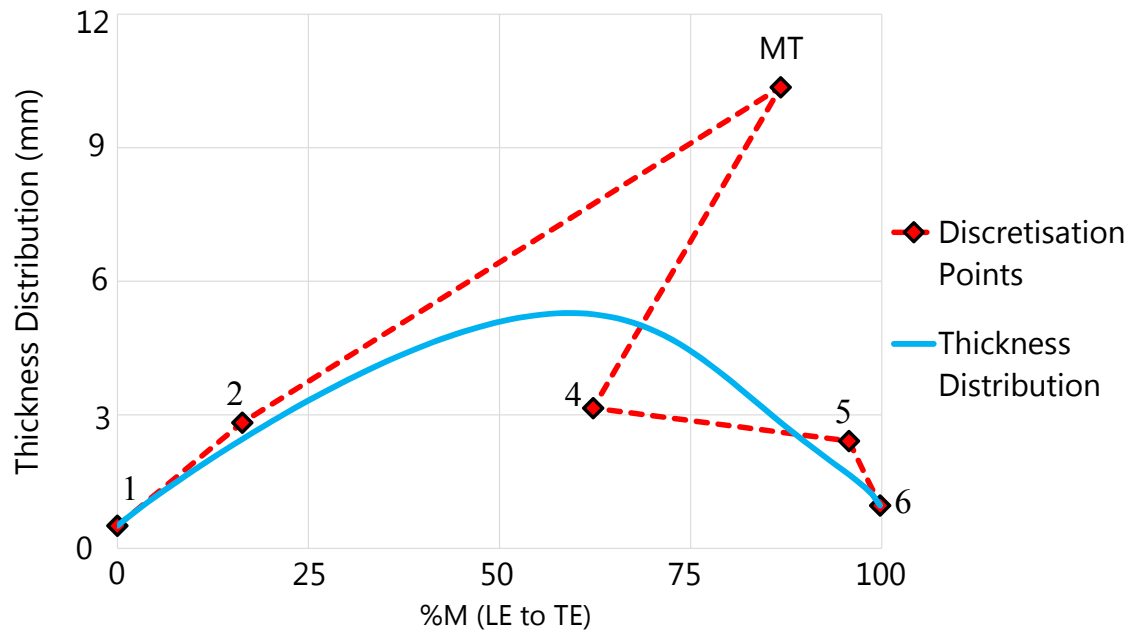


Figure B.11: Optimised Blade Thickness Distribution (Mean)

Table B.28: Optimised Thickness Distribution Discretisation Points Locations (Mean)

Discretisation Points	x	y
1	0.0	0.51
2	16.37	2.82
MT	86.96	10.36
4	62.38	3.15
5	95.91	2.41
6	100.0	0.96

Table B.29: Optimised Angle Distribution Properties (Mean)

Property	Description
Layer	50% Span
Distribution	Thickness
Curve Type	Bezier Segment

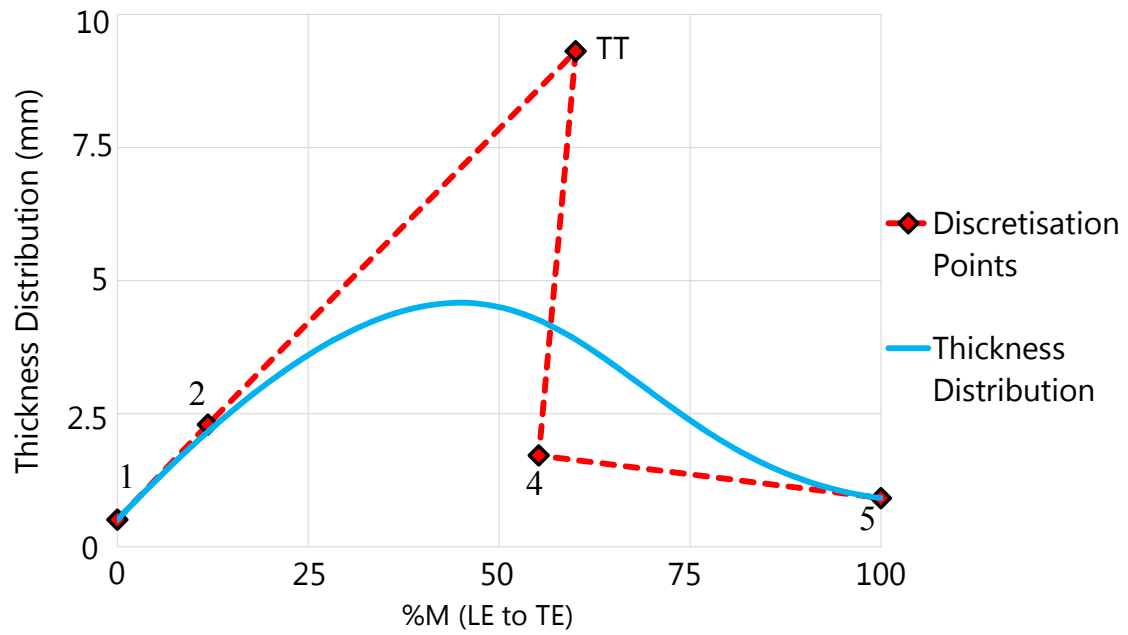


Figure B.12: Optimised Blade Thickness Distribution (Tip)

Table B.30: Optimised Thickness Distribution Discretisation Points Locations (Tip)

Discretisation Points	x	y
1	0.0	0.51
2	11.84	2.23
TT	60.01	9.31
4	55.19	1.71
5	100.0	0.91

Table B.31: Optimised Angle Distribution Properties (Tip)

Property	Description
Layer	100% Span
Distribution	Thickness
Curve Type	Bezier Segment